National Aeronautics and Space Administration

Joint Inversion and Assimilation Technique
to Understand Inter-eruptive Deformation Processes at Active Volcanoes

Mary Grace Bato (329A)

Paul Lundgren (329A), Marco Bagnardi (329A), Alberto Roman (329A)

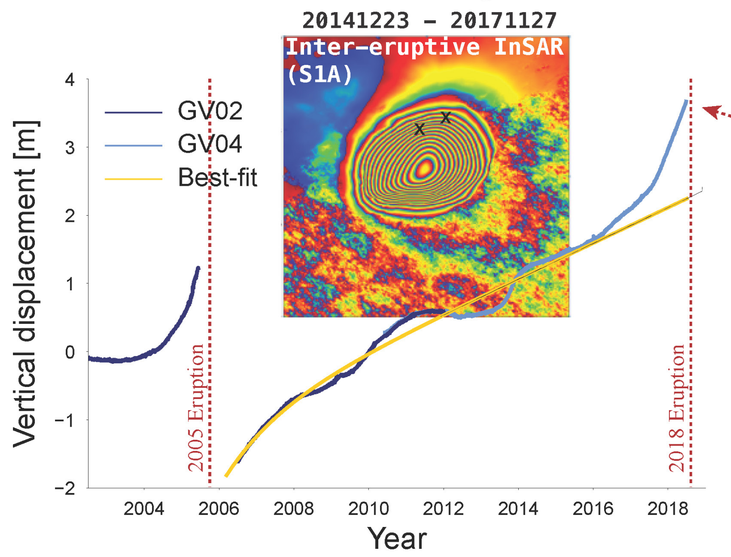
0. INTRODUCTION

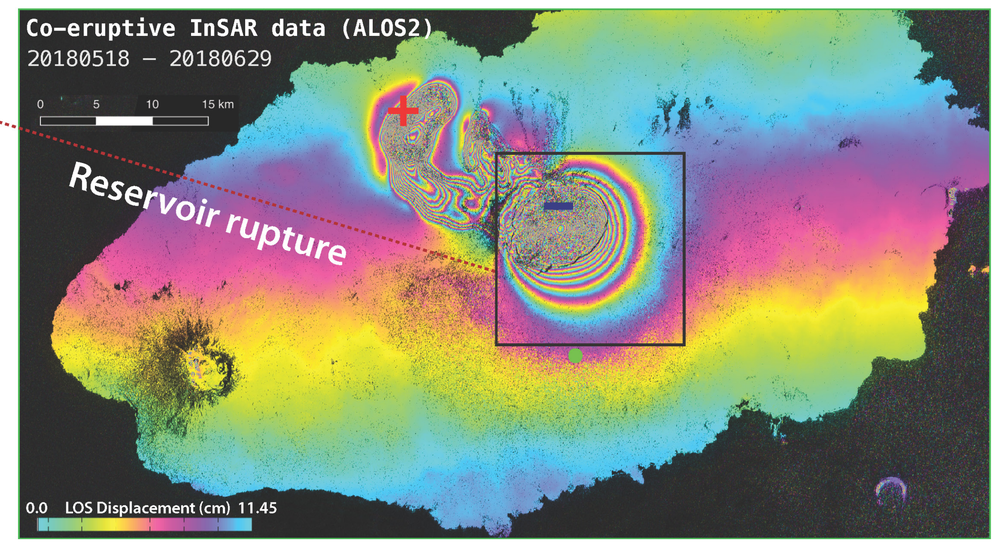
When volcanic unrest is detected, it is important to **accurately track source parameters and their uncertainties in real-time** to forecast if an eruption is imminent.

One of the most **important parameters to track is the overpressure evolution** inside the shallow magma reservoir.

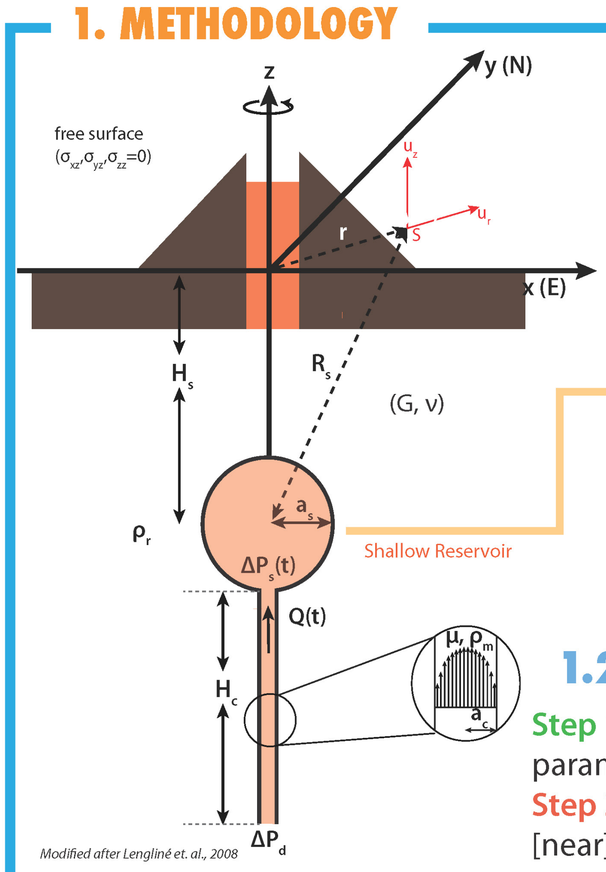
Objective: Develop a simple and fast framework to track the shallow reservoir evolution in [near] real time using GNSS and InSAR data.

@ SIERRA NEGRA, GALAPAGOS, ECUADOR





1. METHODOLOGY



Modified after Lengliné et. al., 2008

1.1 PHYSICS-BASED DYNAMICAL MODEL

Rising magma increases the pressure inside a magma chamber causing the system to overpressurize. When a critical value is reached, the magma chamber may rupture allowing the magma to propagate which may then lead to an eruption.

Evolution of Overpressure:

$$\frac{\Delta P_s(t_{i+1}) - \Delta P_s(t_i)}{t_{i+1} - t_i} = \frac{G a_c^4}{8\gamma_s a_s^3 \mu H_c}\left[\Delta P_d - \Delta P_s(t_i) + (\rho_r - \rho_m) g H_c - \Delta P_s(t_0)\right]$$

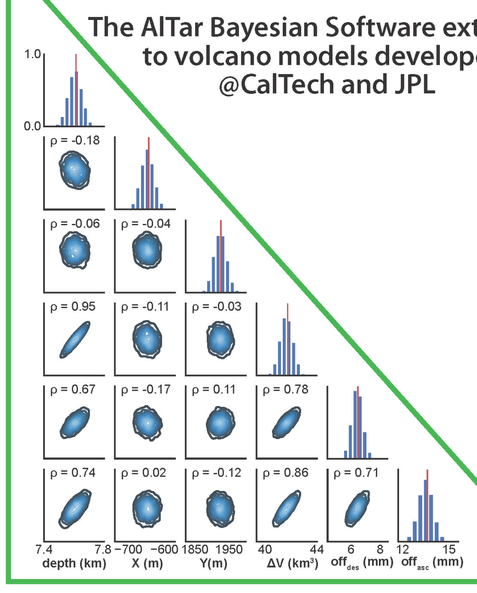
Overpressure-Displacement Data Relationship:

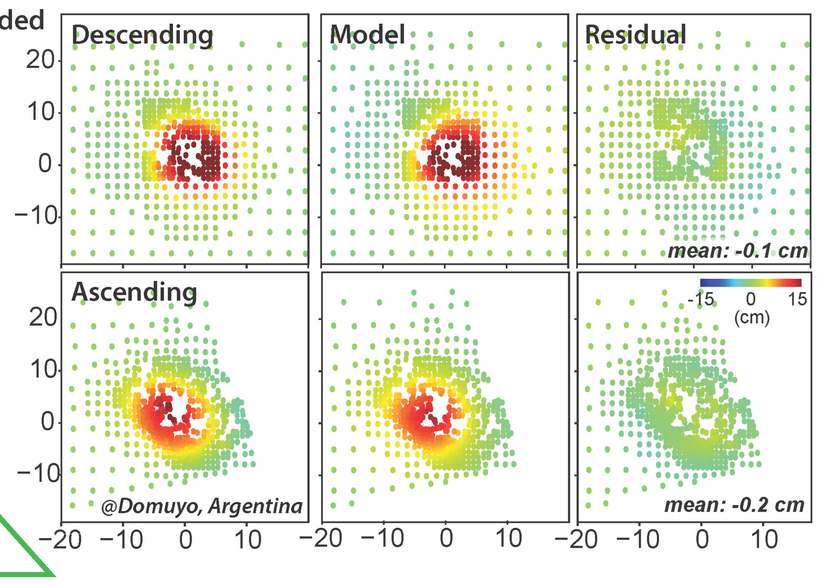
$$u_R(r, t_i) = \frac{(1-v)}{G} r\left(\alpha_s \frac{a_s{}^3}{R_s^3} \Delta P s_{t_i}\right)$$
$$u_z(r, t_i) = \frac{(1-v)}{G}\left(H_s \alpha_s \frac{a_s{}^3}{R_s^3} \Delta P s_{t_i}\right)$$

1.2 INVERSION + DATA ASSIMILATION (DA)

Step 1: Do Bayesian inversion to constrain geometrical parameters and get *a priori* info for time-varying parameters.

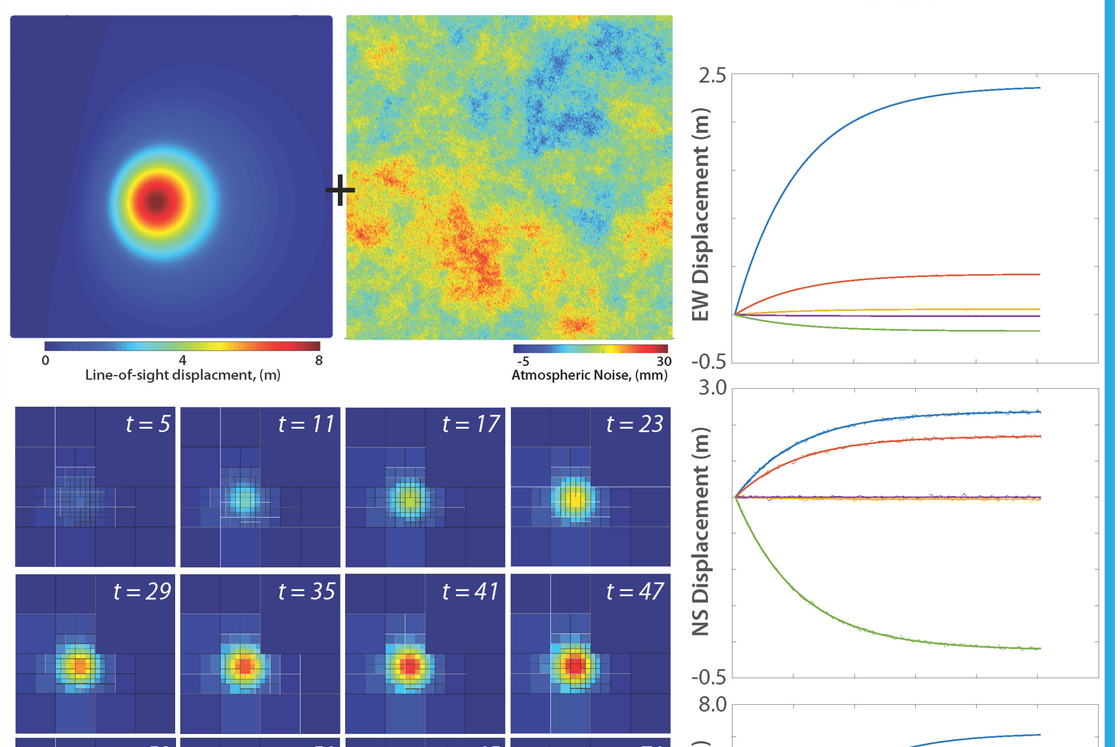
Step 2: Use PDFs from Step 1, then **perfrom DA** to track in [near] real-time the state of the system and/or estimate the parameter that can change in time.



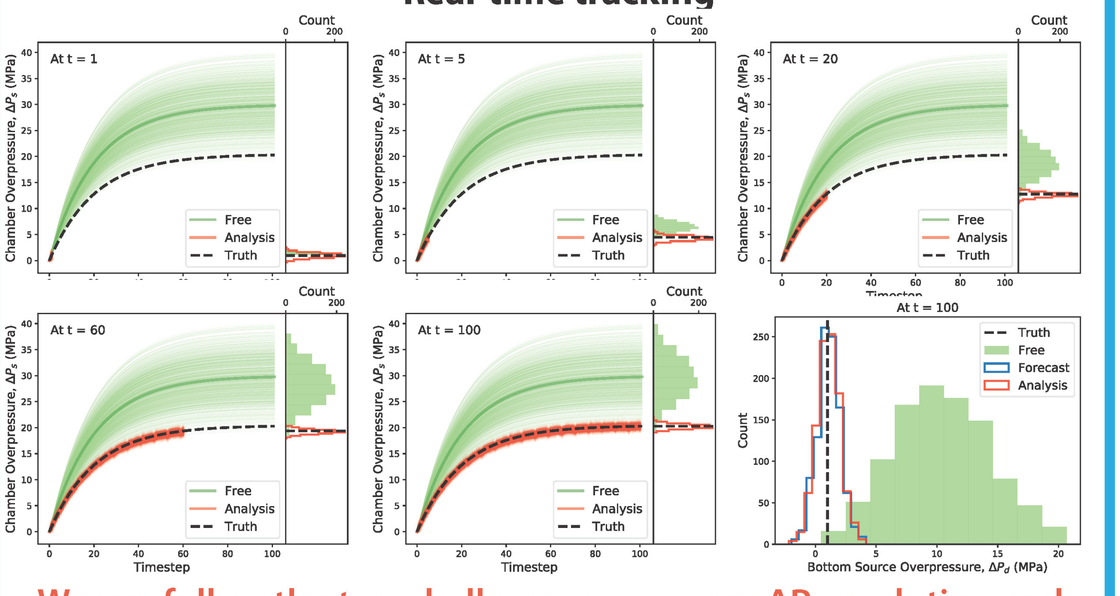


2. RESULTS

Synthetic Data used



Real-time tracking



We can follow the *true* shallow overpressure ΔPs evolution and estimate the inlet pressure ΔPd.

3. CONCLUSIONS & PERSPECTIVES

We have presented a simple framework to track the evolution of the shallow chamber using combined inversion and data assimilation.

- √ With a simple dynamical model (one-reservoir with constant inlet pressure).
- √ Realistic atmospheric noise was added
- √ Quadtree was performed
- √ InSAR covariance was considered

NEXT: Follow the rapid acceleration of deformation prior to an eruption: Sierra Negra case

National Aeronautics and Space Administration

Jet Propulsion Laboratory
California Institute of Technology
Pasadena, California

www.nasa.gov

Copyright 2019. All rights reserved.

Poster No. EA02

National Aeronautics and Space Administration

Diffuse Heating of Volcanoes Prior to Eruption

Author: Társilo Girona (329A)
Co-authors: Vincent Realmuto (329A), Paul Lundgren (329A)

TAKE-HOME MESSAGE

- Volcanoes get warm years before eruptions due to the large-scale (~volcanic edifice size) diffuse release of heat (Fig. 1). This is the first time that large-scale diffuse heating is detected [1].
- Diffuse heating probably reflects the latent heat released during the underground condensation of volcanogenic water vapor. Volcanic thermal power and subsurface pressure are now linked through a transport model [2].
- Our findings open new horizons to better constrain the thermal budget of active volcanic systems, explore the coupling between thermal emissions and ground deformation [3], and improve the forecasting of eruptions.

1. Introduction: volcanoes release heat through the soil

Previous studies in fumarolic fields revealed that heat is released diffusively through the soil. **Diffuse heating is a major source of energy**, and has been found to dominate over the elastic energy released during seismic and deformation crises [4].

Research Questions:

a. Does diffuse heating occur over large areas of the volcanic edifices?
b. Are volcanic eruptions preceded by an enhancement of diffuse heating?
c. How is diffuse heating related to the pressure of magma reservoirs?

Case Studies:

Ontake (Japan)
Calbuco (Chile)
Ruapehu (New Zealand)
Redoubt (USA)
Domuyo (Argentina)

2. Method: temperature contrast between a volcano and its surroundings

a. We analyzed 16.5 years of radiance data (from ~26,000 to ~47,000 scenes per volcano; > 25 TB) from the MODIS instruments aboard the Terra and Aqua satellites.

b. After discarding cloudy scenes, we calculated the contrast in median brightness temperature between the volcanoes and their surroundings.

c. The results are filtered through an efficient noise reduction technique to extract long-term (~years) trends. This yields the **median anomaly** $\overline{\delta T}(t)$.

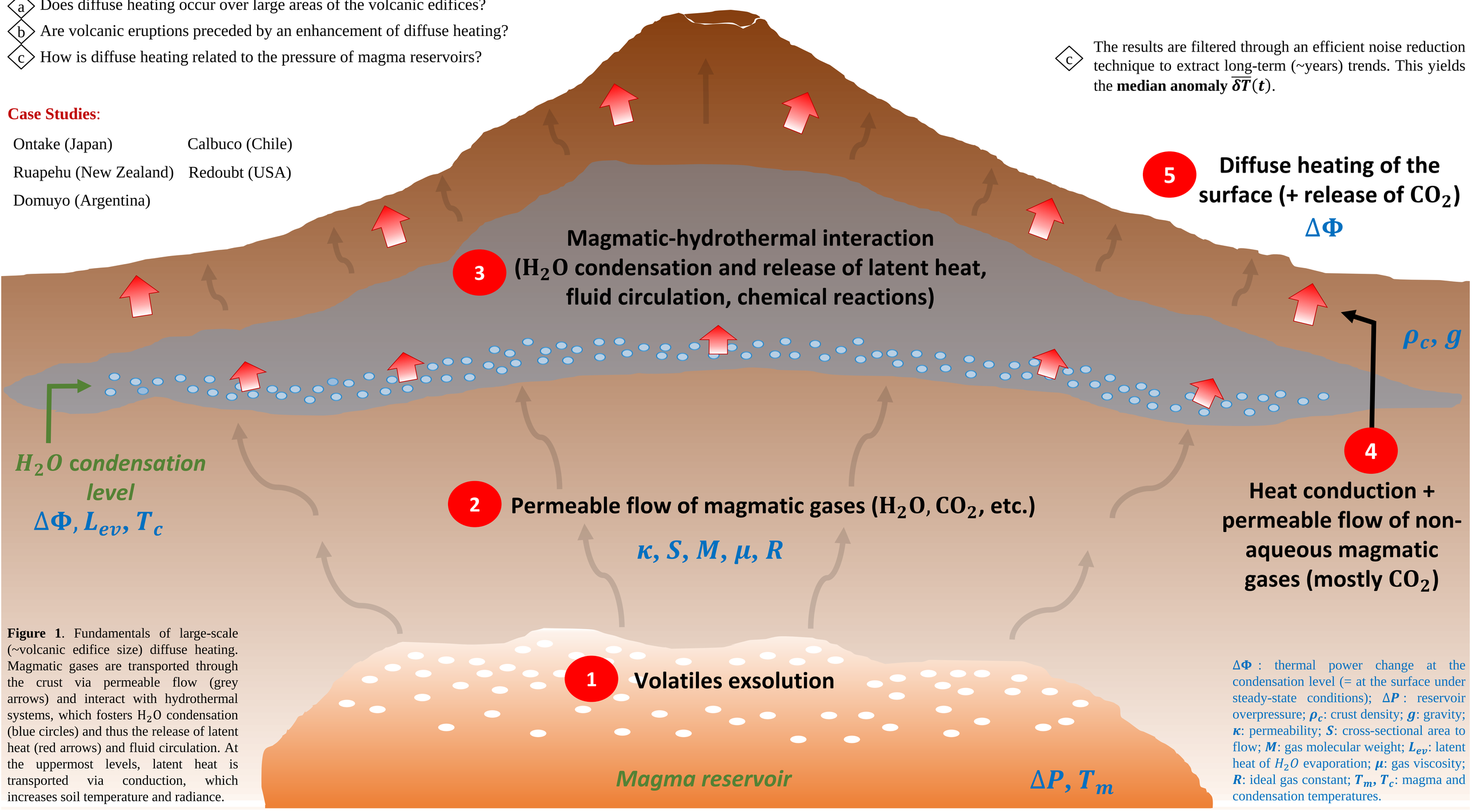


Figure 1. Fundamentals of large-scale (~volcanic edifice size) diffuse heating. Magmatic gases are transported through the crust via permeable flow (grey arrows) and interact with hydrothermal systems, which fosters H_2O condensation (blue circles) and thus the release of latent heat (red arrows) and fluid circulation. At the uppermost levels, latent heat is transported via conduction, which increases soil temperature and radiance.

$\Delta\Phi$: thermal power change at the condensation level (= at the surface under steady-state conditions); ΔP : reservoir overpressure; ρ_c: crust density; g: gravity; κ: permeability; S: cross-sectional area to flow; M: gas molecular weight; L_{ev}: latent heat of H_2O evaporation; μ: gas viscosity; R: ideal gas constant; T_m, T_c: magma and condensation temperatures.

3. Results: volcanic edifices get warm for years before eruptions

a. The last magmatic and gas-driven eruptions were preceded by long-term (~years) warming of ~0.10-0.72 ℃ (Fig. 2).

↓

Pre-eruptive increases of thermal power of **10s of MW**.

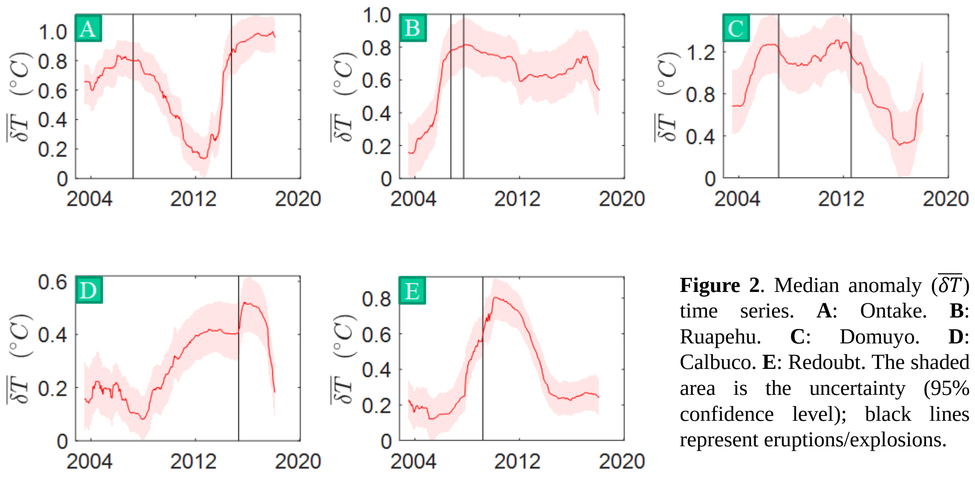


Figure 2. Median anomaly ($\overline{\delta T}$) time series. **A**: Ontake. **B**: Ruapehu. **C**: Domuyo. **D**: Calbuco. **E**: Redoubt. The shaded area is the uncertainty (95% confidence level); black lines represent eruptions/explosions.

4. Interpretation: diffuse heating reflects underground H_2O condensation

a. We propose that large-scale diffuse heating reflects the latent heat released during the underground condensation of volcanogenic H_2O (Fig. 1). The rate of heat production is controlled by the supply of H_2O (via permeable flow) to the condensation zone, and thus by the magma reservoir pressure.

b. Under local thermal equilibrium and steady-state conditions, **thermal power increases of 10s of MW correspond to overpressures of ~0.1 – 2 MPa** in magma reservoirs (Fig. 3).

A

$$\Delta\Phi = \frac{2\rho_c g \kappa S M L_{ev}}{\mu R (T_m + T_c)} \Delta P$$

B

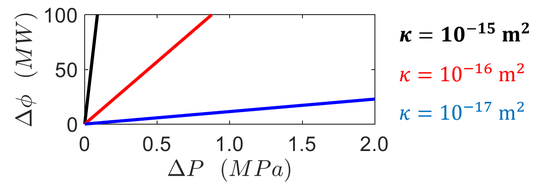


Figure 3. Link between thermal power change ($\Delta\Phi$) and reservoir overpressure (ΔP). **A**: Solution of the mass, momentum and energy equations under local thermal equilibrium and steady-state conditions. **B**: $\Delta\Phi$ vs ΔP for realistic values of the parameters. See Fig. 1.

National Aeronautics and Space Administration
Jet Propulsion Laboratory
California Institute of Technology
Pasadena, California
www.nasa.gov

Copyright 2019. All rights reserved.

References:
[1] Girona, T., Realmuto, V., Lundgren, P., Volcanoes get warm for years prior to eruption, *Submitted to Nature*. **[2]** Girona, T., Realmuto, V., On the source of diffuse heating at active volcanoes, *In Prep.* **[3]** Lundgren, P., Bato, G., Girona, T., Samsonov, S., Realmuto, V., Dynamics of unrest at a large silicic volcanic system: Domuyo volcano, Argentina, *In Prep.* **[4]** Chiodini, G. *et al. J. Geophys. Res. Solid Earth* **106,** 16213–16221 (2001).

Acknowledgments:
T. Girona is supported by an appointment to the NASA Postdoctoral Program at the Jet Propulsion Laboratory, Caltech, administered by Universities Space Research Association under contract with NASA.

Poster No. EA-03

National Aeronautics and Space Administration

Blind Source Separation with application to surface deformation and change

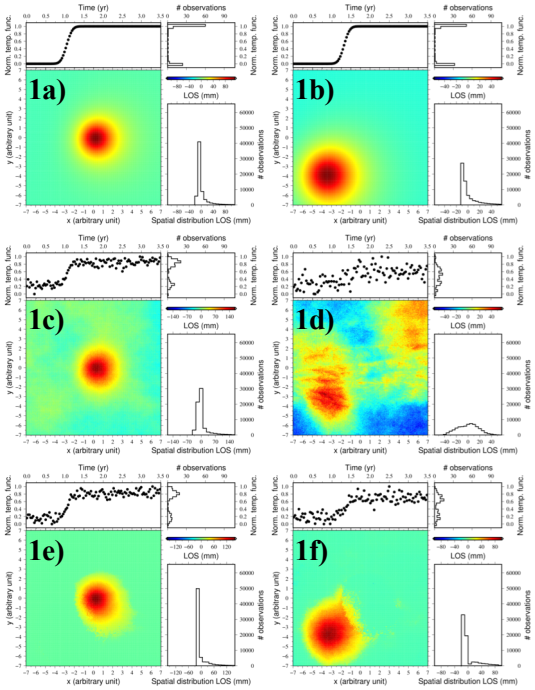
A. Gualandi (329) and Z. Liu (329)

Introduction

GOAL: Exploit the large amount of data derived from InSAR satellite missions (e.g., upcoming NISAR).

PROBLEM: Several deformation mechanisms are active at the same time.

SOLUTION: Blind source separation techniques like Independent Component Analysis (ICA). A variational Bayesian approach (vbICA) is superior with respect to the widely used FastICA algorithm (Figs. 1 and 2). vbICA is a generative model: it uses a mix of Gaussians to model the sources and minimize the KL-divergence between the approximating and true sources probability density functions. FastICA is a mapping approach that maximizes the non-Gaussianity of the sources.



Synthetic tests

256 × 256 = 65536 pixels

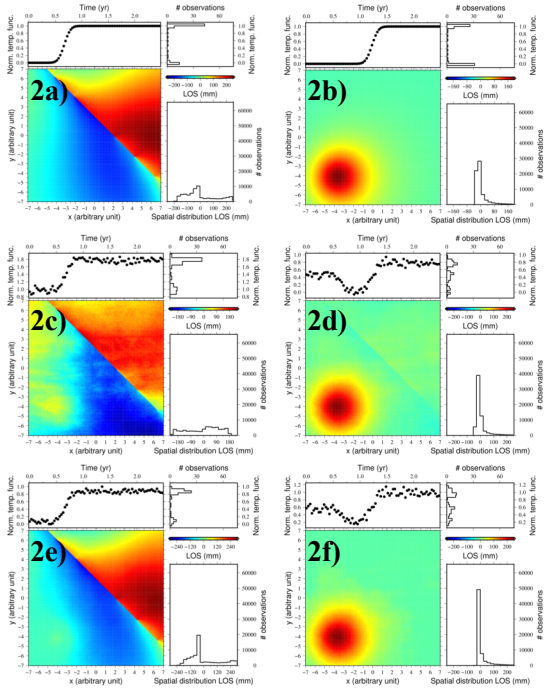
Fig. 1: Two Mogi sources (107 epochs)

Fig. 2: Creep + Mogi (76 epochs)

In both cases we add noise of different origin (atmospheric stratification, tropospheric turbulence, orbital errors, random phase noise).

Fig. 1: Line-Of-Sight (LOS) displacement $X_{LOS} = AS$. A: normalized temporal function. S: spatial distribution. Top row: true sources (Figs. 1a-b). Central/Bottom row: FastICA/vbICA sources (Figs. 1c-f).

Fig. 2: As Fig. 1, but for creep signal (left column) and a Mogi source (right column).



California: Natural separation of long-term subsidence and seasonal deformation (Figs. 3a-b). They might be due to anelastic and elastic compaction, respectively. Subsidence persists after the end of the drought (Fig. 3c). We can also isolate unwrapping errors (Fig. 3d), manifested as pixels with anomalous jumps of the order of half of the radar wavelength.

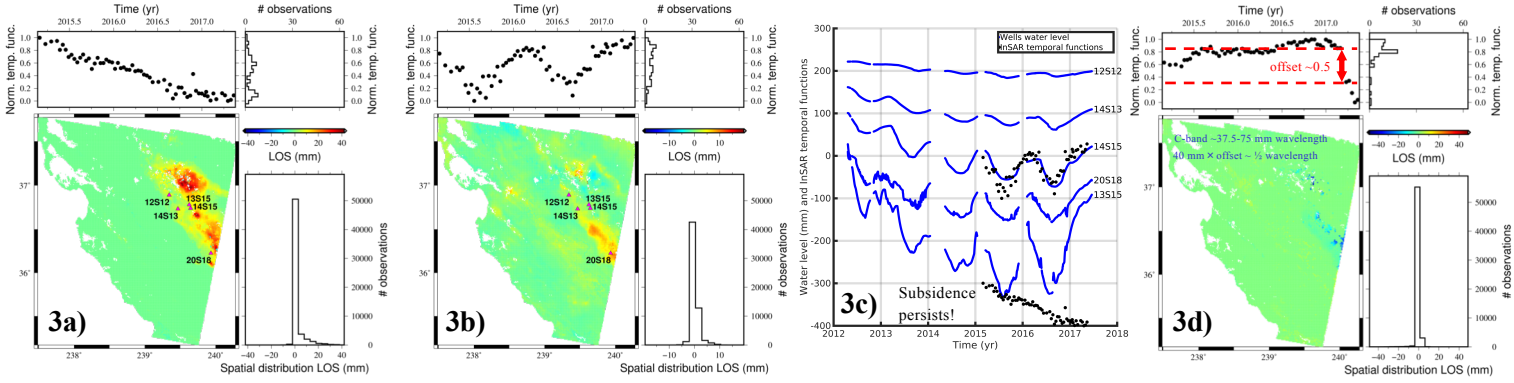


Fig. 3: a) Long-term subsidence in Central Valley (CV) might indicate anelastic compaction. Magenta triangles: wells location. b) Seasonal deformation in CV might be related to shallow aquifers and elastic deformation. c) Wells water level (blue) and arbitrarily rescaled InSAR long-term/seasonal temporal functions (black). d) Isolated jumps probably due to unwrapping errors.

Conclusions: vbICA allows to retrieve useful information from large spatio-temporal datasets and helps interpret them.

National Aeronautics and Space Administration
Jet Propulsion Laboratory
California Institute of Technology
Pasadena, California

www.nasa.gov

Copyright 2019. All rights reserved.

Poster No. EA-04

National Aeronautics and Space Administration

Widespread initiation, reactivation, and acceleration of landslides in the northern California Coast Ranges due to extreme rainfall

Alexander Handwerger (329-A), Eric Fielding (329-A), Mong-Han Huang (U of Maryland), Georgina Bennett (U of East Anglia), Cunren Liang (Caltech), and William Schulz (USGS)

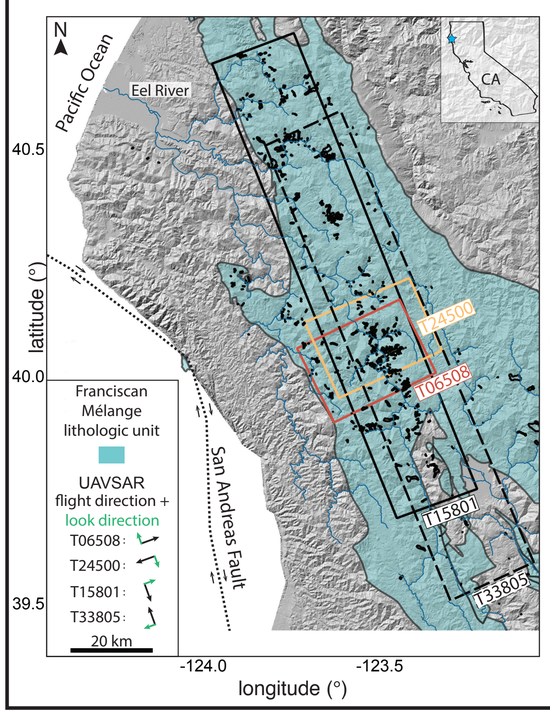
1. Introduction

Landslides are a natural hazard that causes billions of dollars in damages and claims thousands of lives annually. Climate change, which is altering the frequency and magnitude of precipitation worldwide, is predicted to have a major impact on landslides.

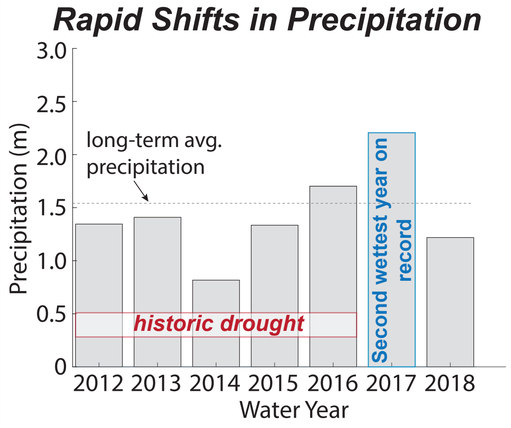
Main Question: *How do landslides respond to drought and extreme rainfall?*

Objectives: Document the kinematic response of hundreds of slow-moving landslides in California during the recent historic drought (2012-2016) and the second wettest year on record (2017).

California Coast Ranges



Rapid Shifts in Precipitation



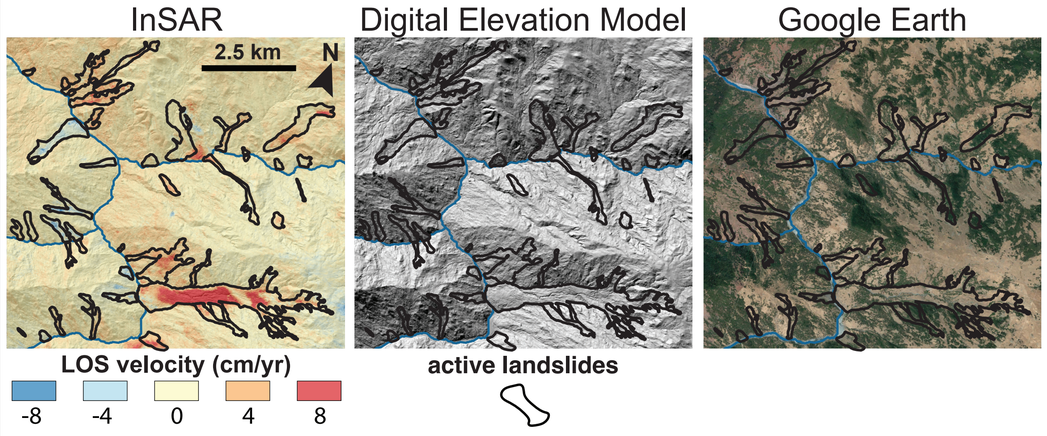
Rapid shifts from dry-to-wet extremes in California, similar to the changes in precipitation that occurred between 2015 and 2017, are predicted to increase by 25% to 100% during the 21th century (Swain et al., 2018)

2. Methods

Airborne Synthetic Aperture Radar



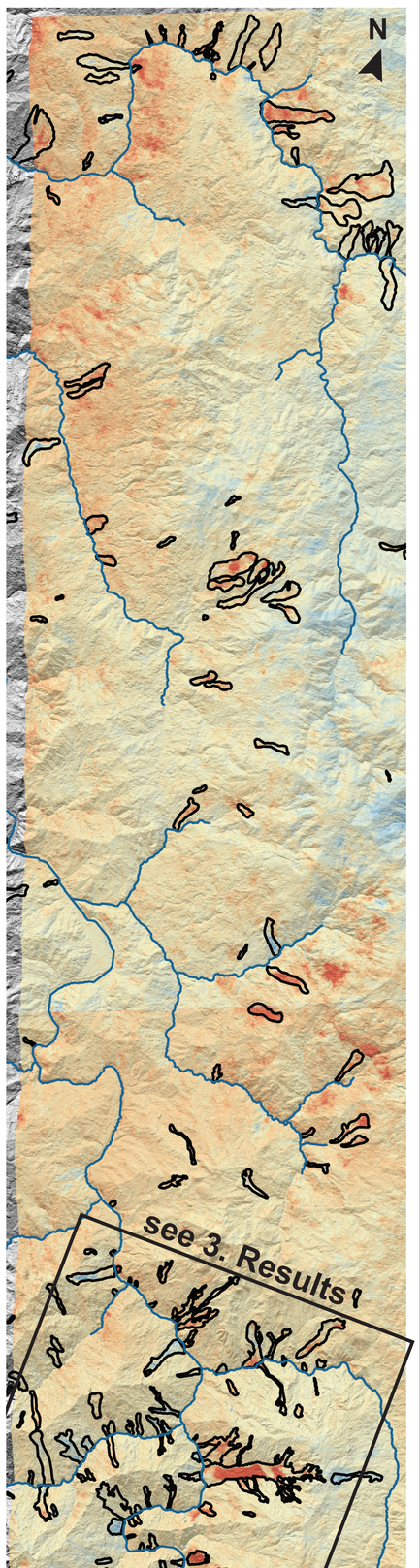
We use radar interferometry (InSAR) and pixel offset tracking techniques on a novel dataset from NASA/JPL Uninhabited Aerial Vehicle Synthetic Aperture Radar (UAVSAR). The data is processed with the JPL/Caltech and Stanford InSAR Scientific Computing Environment (ISCE) software package. We construct time series inversions with the Generic InSAR Analysis Toolbox (GIAnT) and perform a least squares inversion with multiple line-of-sight (LOS) measurements to invert for 3-D ground surface displacement.



Landslide reconnaissance

We identify active landslides between April 2016 and February 2018 using InSAR velocity maps. Landslides display clear ground deformation (high positive or negative LOS velocities). We then use high-resolution digital elevation models, Google Earth images, and previously published landslide inventories to confirm that the InSAR deformation signals correspond to landslides.

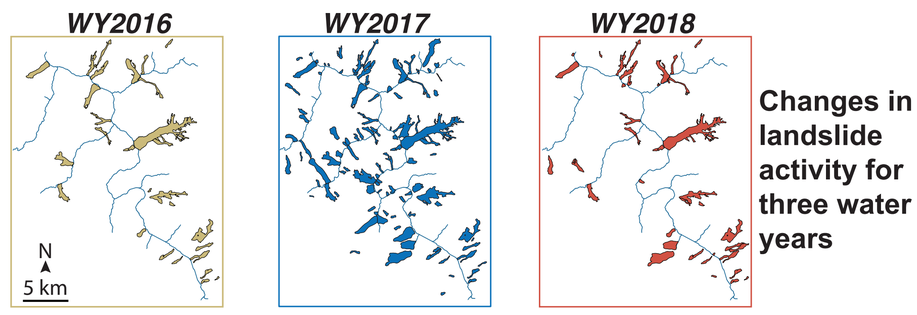
UAVSAR T33805



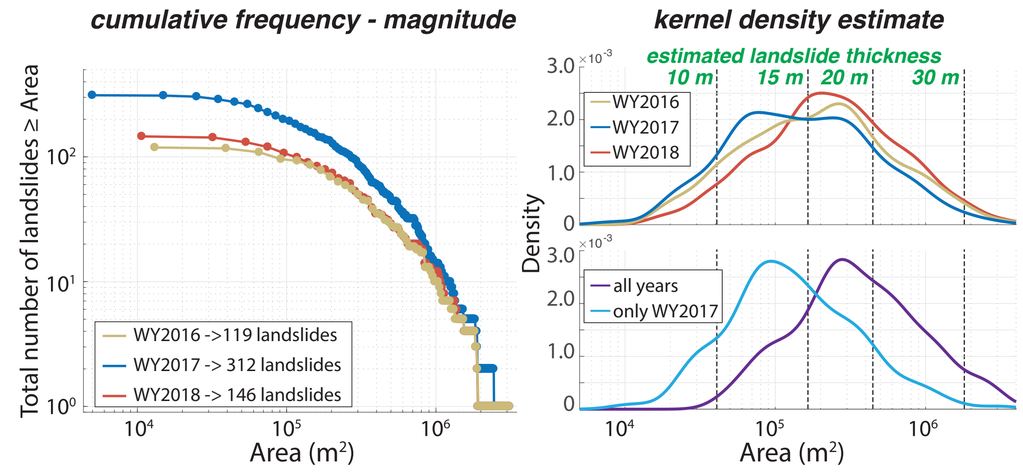
3. Results

We found that 312 landslides were moving due to extreme rainfall during 2017, compared to 119 during 2016, which was the final year of the historic multi-year drought. However, with a return to below average rainfall in 2018, only 146 landslides remained in motion.

WY = water year (Oct 1 to Sep 30)

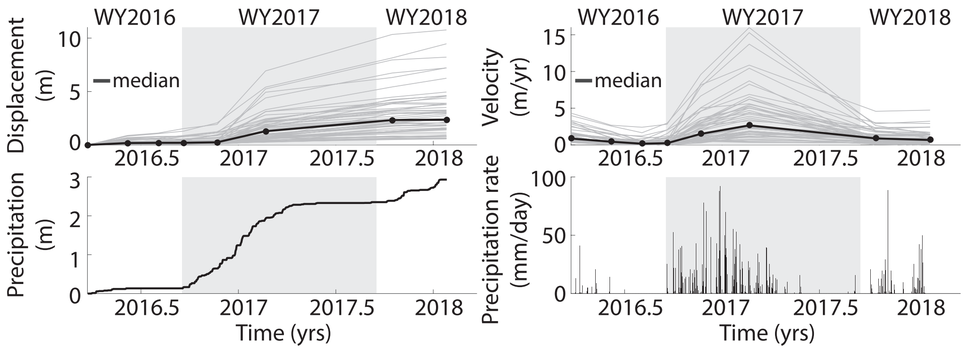


Changes in landslide activity for three water years



The increased number of landslides during 2017 was primarily accommodated by landslides that were smaller than the landslides that remained active between 2016 and 2018. Our findings suggest that small landslides experience large precipitation-induced pore-water pressure swings, which trigger large changes in landslide activity. Large landslides are less sensitive to changes in seasonal to annual rainfall and display more consistent motion from year-to-year.

Time series analysis for 51 landslides



Landslides that were active during the full study period displayed seasonal changes in motion. There was a large increase in displacement for each landslide that corresponded to the large increase in precipitation during the 2017. The maximum velocity occurred during the wet season of 2017.

4. Conclusions

- Large, deep-seated, slow-moving landslides show size-dependent sensitivity to large changes in annual rainfall.
- The extreme wet season of 2017 triggered a widespread, but short-lived increase in landslide activity and velocity.
- Based on climate model predictions for the next century in California, which include increases in annual precipitation and increases in the frequency of dry-to-wet extremes, we hypothesize that there will be an overall increase in landslide activity.

National Aeronautics and Space Administration

Jet Propulsion Laboratory
California Institute of Technology
Pasadena, California

www.nasa.gov

Copyright 2019. All rights reserved.

Handwerger, A. L., Fielding, E. J., Huang, M., Bennett, G., Liang, C., and Schulz W. H. (2019). Widespread initiation, reactivation, and acceleration of landslides in the northern California Coast Ranges due to extreme rainfall. JGR Earth Surface.

Swain, D. L., Langenbrunner, B., Neelin, J. D., & Hall, A. (2018). Increasing precipitation volatility in twenty-first-century California. Nature Climate Change, 8(5), 427.

EA-05

National Aeronautics and Space Administration

Using Geodetic Data to Constrain the Hazard Probability of Distributed Rupture

Author: Chris Milliner (329A)

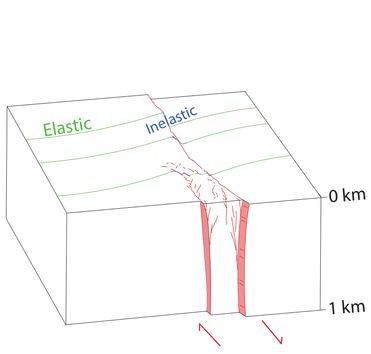
Rui Chen (California Geological Survey), Jean-Philippe Avouac (Caltech)
Tim Dawson (California Geological Survey), Andrea Donnellan (3200), James Dolan (USC)

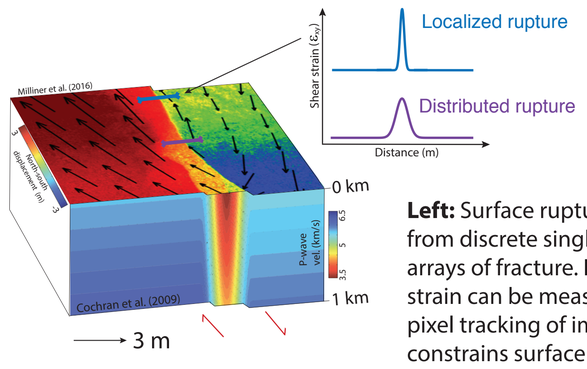
1. Introduction

Background Probabilistic Fault Displacement Hazard Analysis (PFDHA), defines the probability of distributed faulting with distance from the primary fault strand. So far this has been constrained solely from field observations of recent surface ruptures, which suffer from large uncertainty and are sparsely measured along ruptures.

Aim The degree of strain localization along surface rupturing earthquakes can vary from discrete single-faults to distributed arrays of fractures that are 100's of meters wide. Here we attempt to measure this variation of inelastic strain localization using geodetic imaging data (optical and radar), to then develop empirical probability models of its occurrence.

Importance Distributed inelastic, permanent strain poses a hazard to critical infrastructure (e.g., water and gas piplines, roads and bridges) and affects the mechanical properties of rock (e.g., permeability), and causes attenuation of seismic radiation.





Left: Surface rupture can vary from discrete single faults to arrays of fracture. Inelastic strain can be measured by pixel tracking of images that constrains surface motion.

2. Methods

Measuring Surface Displacement

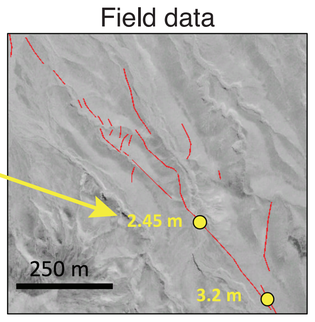
Data: We use air photos, satellite optical imagery (Worldview and Quickbird, 50 cm resolution), and ALOS-2 descending and ascending SAR pairs in strip-map mode taken before and after earthquakes to measure near-field surface deformation.

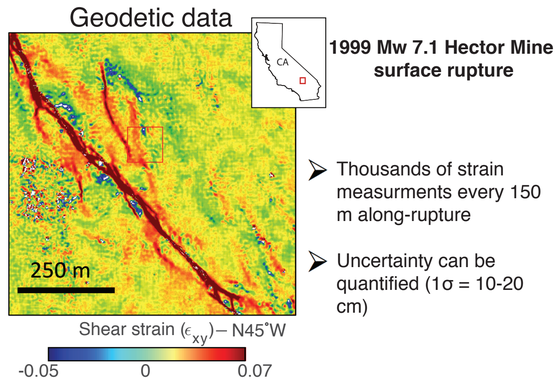
Correlation method: We use correlation of radar and optical images before and after earthquakes to resolve the surface defomation to subpixel precision (bottom right). This provides denser measurements of strain that are of lower uncertainty than field data (bottom left).

Field measurment of fault offset



- Sparse measurements (yellow dots)
- Large or sometimes unknown uncertainty due to subjective nature



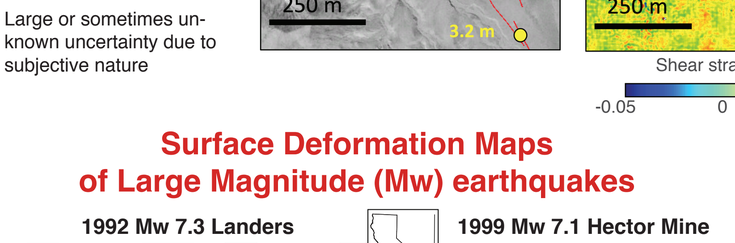


1999 Mw 7.1 Hector Mine surface rupture

- Thousands of strain measurments every 150 m along-rupture
- Uncertainty can be quantified (1σ = 10-20 cm)

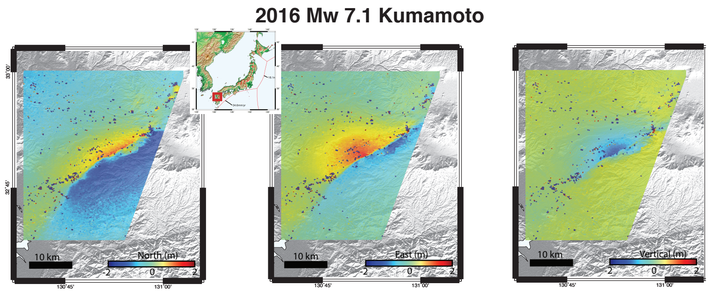
Surface Deformation Maps of Large Magnitude (Mw) earthquakes

1992 Mw 7.3 Landers | **1999 Mw 7.1 Hector Mine**



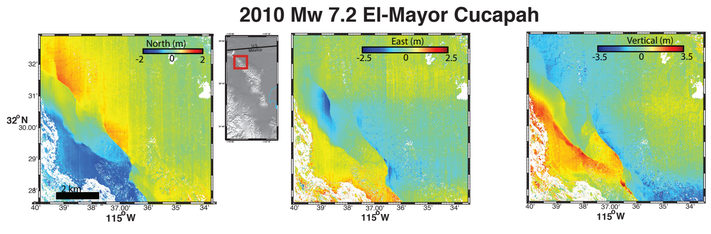
2D surface deformation (horizontal components) constrained from image correlation of **aerial photos**

2016 Mw 7.1 Kumamoto



3D surface deformation from inverting multi-look ALOS-2 **SAR offsets** (azimuthal and range)

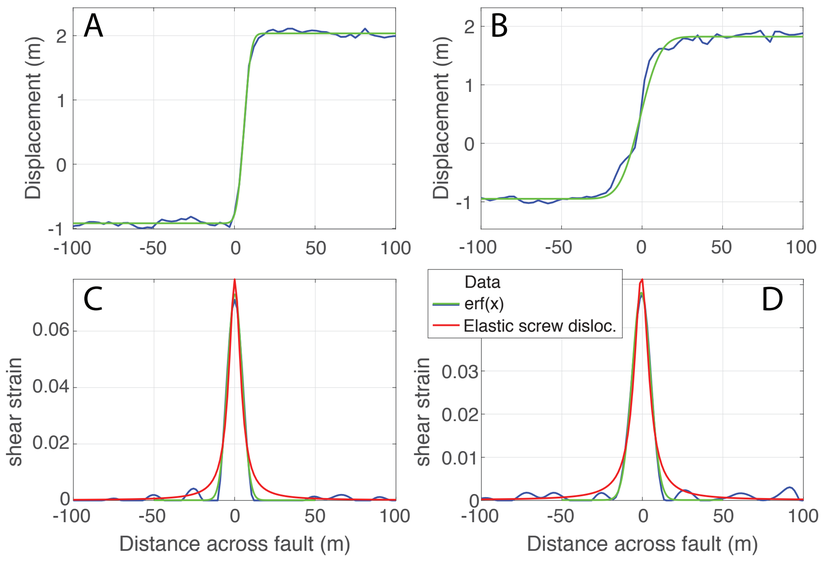
2010 Mw 7.2 El-Mayor Cucapah



3D surface deformation from correlation of **stereo-view optical imagery** (World View).

3. Results

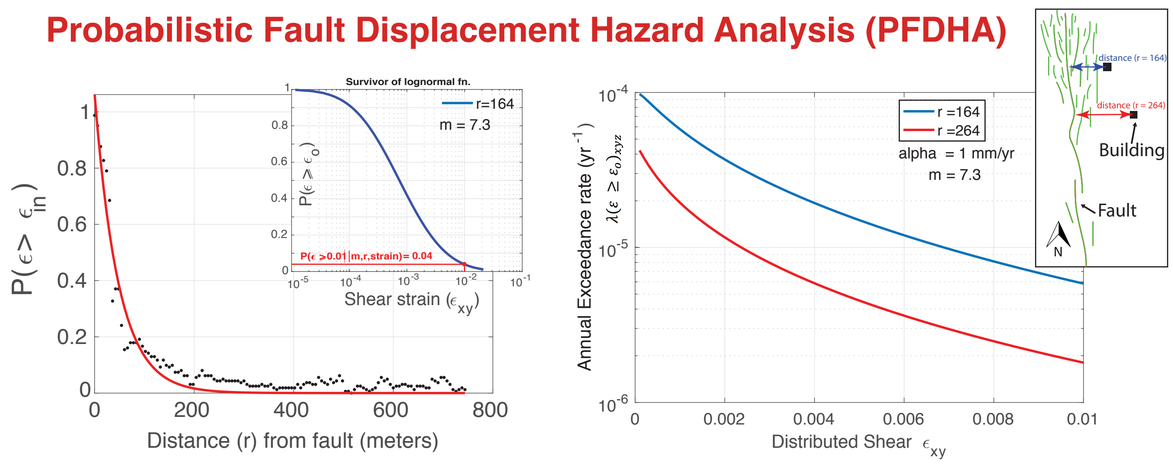
Measurements of Surface Strain



From the deformation maps we extract fault-parallel displacement (A,B) and shear strain (C,D) profiles, which vary in amplitude and attenuation across the ruptures. Strain (bottom) is estimated as the gradient of displacement (top).

We find the observed strain distribution(blue) is inconsistent with elastic strain predicted by a screw dislocaiton (red), and is instead likely reflecting inelastic failure of the surface (green)

Probabilistic Fault Displacement Hazard Analysis (PFDHA)



PFDHA calculations. Left, shows conditional probability of occurrence and exceedance (inset) constrained from strain profiles (top figure). These are used to calculate the hazard curve (right) using equation we have developed (below). The hazard curve shows the annual frequency of exceeding a given amount of shear strain at a given distance (*r*), (red and blue lines). Red line has lower hazard or annual frequency as feature (e.g., a building) is situated further away from primary fault (see inset top right for schematic of scenarios).

Annual frequency of exceeding a given shear strain (ε_o)

Annual rate of return (yr^{-1}) **Source**: Geologic slip rates

Conditional probability of exceedance **Source**: This study, strain profiles

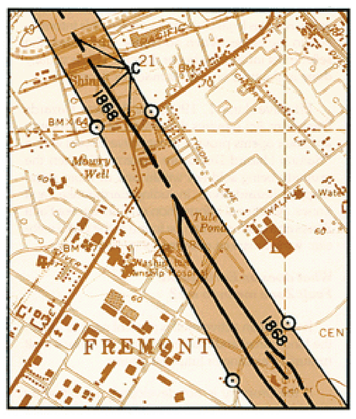
$$\lambda(\varepsilon \geq \varepsilon_o)_{xyz} = \alpha(m)\, P[sr \neq 0 \,|m]\, \int_0^r P[\varepsilon > \varepsilon_{inelastic} | r, z, sr \neq 0]\, P[\varepsilon \geq \varepsilon_o | m, r, \varepsilon_{inelastic}]\, f_R(r) dr$$

Probability of surface rupture (*sr*) given the earthquake magnitude (*m*). **Source**: Empirical scaling relations of past ruptures

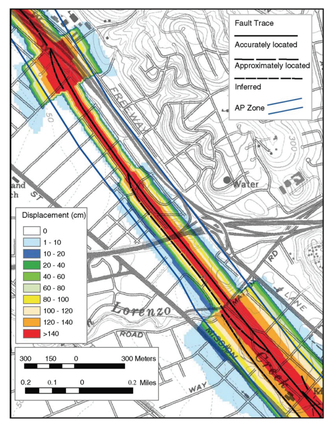
Conditional probability of rupture occurrence at distance (r) **Source**: This study, strain profiles

α = annual return (yr^{-1})
$sr = surface\ rupture$
$m = Moment\ magnitude$
$\varepsilon = fault-parallel\ shear\ strain$
$\varepsilon_{inelastic} = inelastic\ shear\ strain$ (0.004)
$r = distance\ from\ fault$ (m)
$z = footprint\ area$ (m^2)

Advancement of Hazard Maps



Current distributed faulting hazard maps. Setback distances are typically arbitrary (dark brown), giving a binary safe-no safe location and provides no hazard informaiton for structures already situated nearby faults



Our proposed product - a probabilistic estimate of distributed strain, constrained by geodetic imaging data.

4. Conclusions

- Correlation of optical and radar images can be used to measure the full 3D surface deformation, providing dense measurements that are of lower uncertainty than current traditional field observations.
- Geodetic data can resolve the attenuation of inelastic strain across faults providing key data to constrain probabilistic models for occurrence and exceedance of distributed rupture
- The data collected and probability models generated here can be used to better mitigate for the hazard of distributed rupture by producing more accurate probability estimates.

National Aeronautics and Space Administration
Jet Propulsion Laboratory
California Institute of Technology
Pasadena, California
www.nasa.gov

Copyright 2018. All rights reserved.

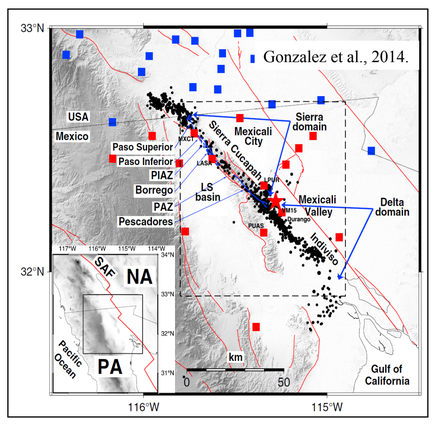
Poster No. EA-06

National Aeronautics and Space Administration

Investigating elastic heterogeneity and topography effects on 2010 M_w 7.2 El Mayor Cucapah coseismic deformation using finite element modelling and space geodetic data

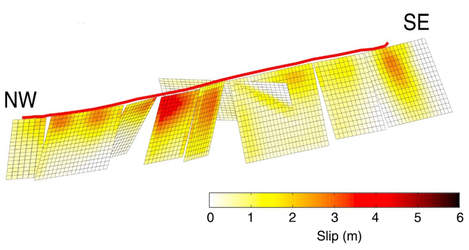
Fabio Pulvirenti (329A) Zhen Liu (329A)
Marco Aloisi (INGV) Alejandro Gonzalez Ortega (CICESE)

1. Introduction



- **Event**: Mw 7.2 El Mayor Cucapah earthquake
- **Date of occurrence**: 4th April 2010
- **Location**: Northeastern Baja California
- **Kinematics**: Right-lateral strike slip and normal faulting (120km NW-SE bilateral rupture)

Motivation: Analytical inversions of geodetic data assume flat homogeneous or layered half-space to provide the slip on fault segments. **Are analytical assumptions sufficient to describe complex tectonic events?**



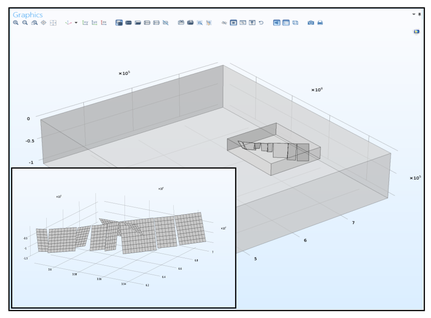
Left: Analytical solution from joint inversions of GPS, InSAR and subpixel offset data from Huang et al., 2016 suggests the presence of 9 fault planes with relatively shallow slip, (peak slip 6m).

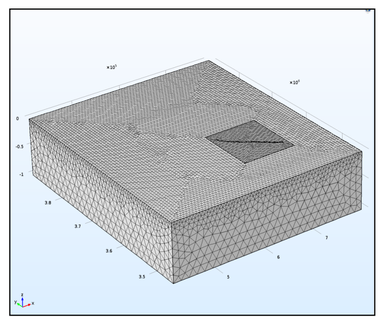
Is this an optimal solution and is it valid when additional complexity is considered?

Objective: Use numerical modeling to check the goodness of the analytical slip solution vs recorded data and further optimize it considering also additional complexity (topography and material heterogeneities).

2. Modeling

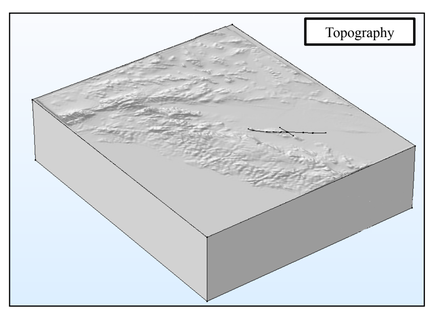
3D finite element model (performed with COMSOL Multiphysics). Analytical fault geometry is embedded into two computational domains to constraint the mesh. Materials configuration include homogeneous, layered (PREM) and heterogeneous case (from SCEC CVM-H).

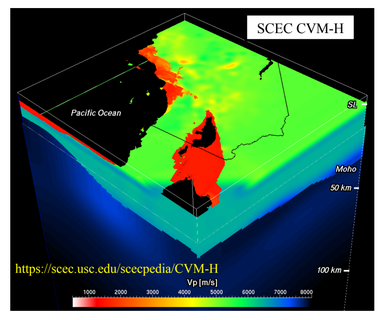




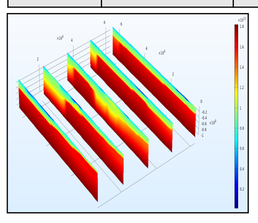
Geometry specs
- Outer Domain 550x550x100km
- Inner Domain 100x100x20km
- Topography: SRTM 90m

Boundary conditions
- Top surfaces: Free
- Bottom surface: Fixed
- Outer boundaries: Roller





Heterogeneous Model Parameters			
Depth(Km)	Density(Kg/m^3)	E(GPa)	v
0-100	1930-3400	2.5 - 180	0.16-0.45

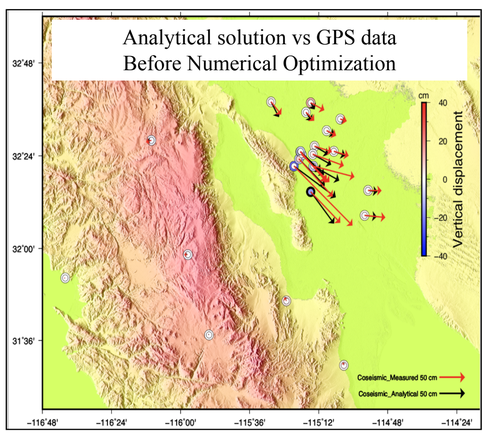


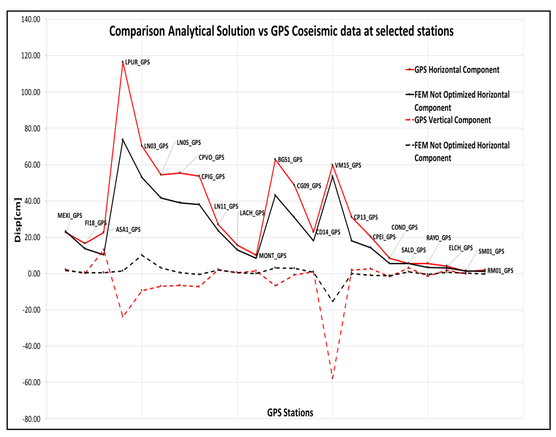
Example of vertical and lateral heterogeneities (Young's modulus)

Optimization

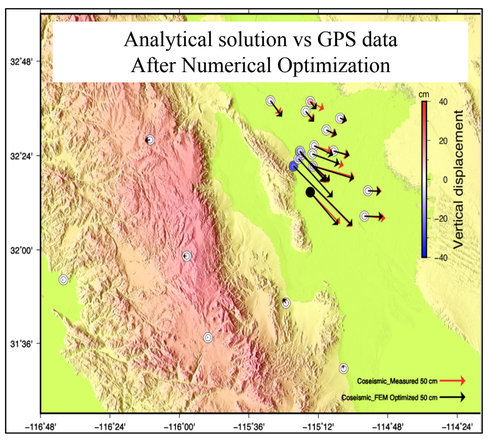
Input: Coseismic GPS data → Least-squared type cost function → **Output: New slip=Analytical Slip*c**
$0 \leq c \leq 2$ spatial control variable

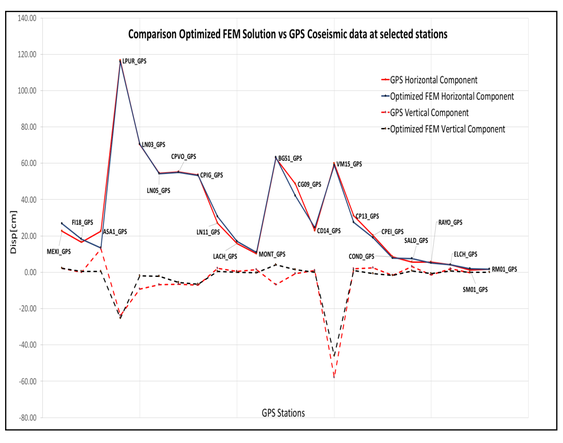
3. Results





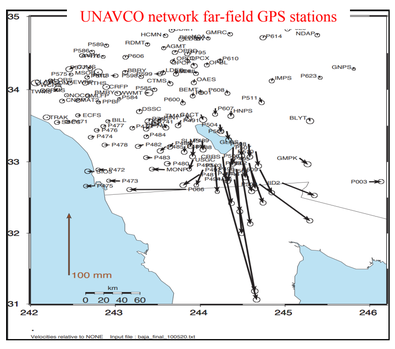
Near-field GPS coseismic displacement from analytical solution underestimate recorded data

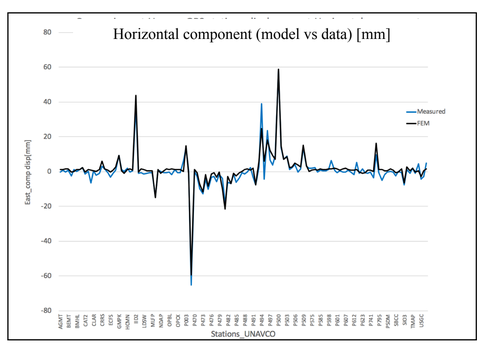


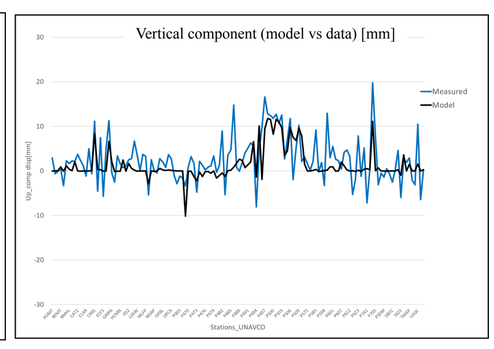


GPS displacement vectors from optimized solution match very well the data

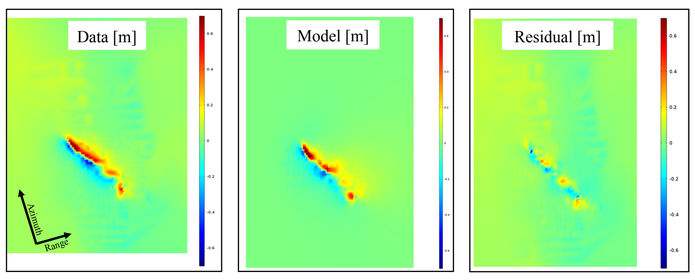
Does the optimized slip provide good fit on other set of data when used in a forward model?



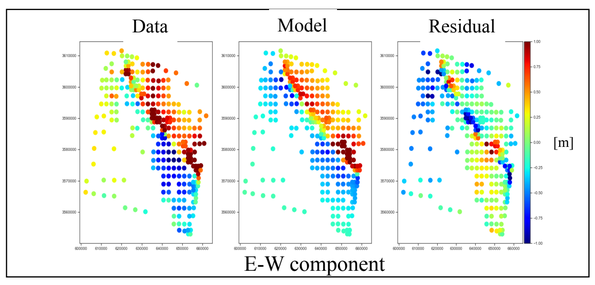




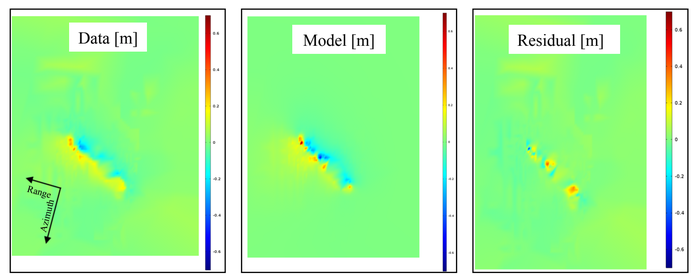
GPS data comparison at far-field UNAVCO stations (horizontal and vertical compoenents)

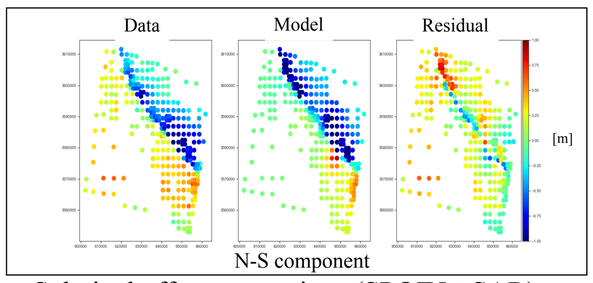


InSAR data comparison (ALOS-PALSAR and ENVISAT)



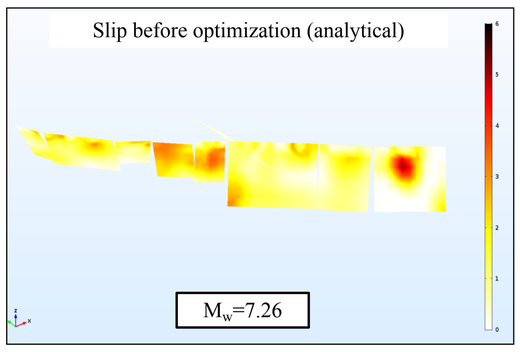
E-W component

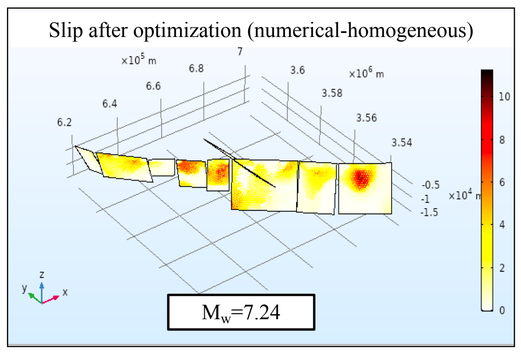




N-S component

Subpixel offset comparison (SPOT5 +SAR)





- Optimized solution increases but spatially reduces the analytical slip to fit the observations;
- Moment magnitude obtained from optimized solution is closer to the recorded value (M_w 7.2).

Main outcomes

- Optimized solution fixes GPS near-field displacement vectors and fits well far-field GPS, InSAR and subpixel off. data.
- Inclusion of heterogeneities increases the slip at depth (about 1-2 m) because of higher rigidity of the medium;
- Inclusion of topology gives negligible contribution (<2%) because most of near-field GPS stations are in a valley.

Conclusions: Our numerical model suggests that El Mayor Cucapah event may have been triggered by much higher slip than expected. Our results provide new hints to better understand the dynamics of such a complex tectonic event and can be of help for future seismic hazard estimation.

References:
❖ Huang et al., 2016. J.Geophys.Res.Solid Earth, 121; ❖ Gonzalez et al., 2014. J.Geophys.Res.Solid Earth, 119.

National Aeronautics and Space Administration
Jet Propulsion Laboratory
California Institute of Technology
Pasadena, California

www.nasa.gov

EA-07

Copyright 2019. All rights reserved.

Closing magmatic conduits: constraints from geodetic observations and dynamical models

Alberto Roman (329A-Affiliate)

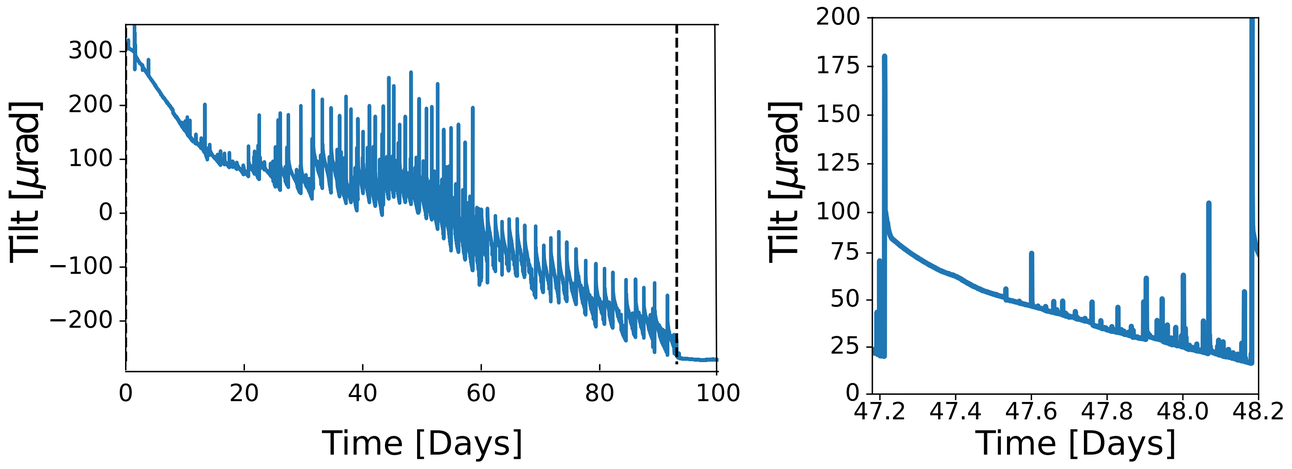
Paul Lundgren (329A) **Marco Bagnardi (329A-Affiliate)**

1. Introduction

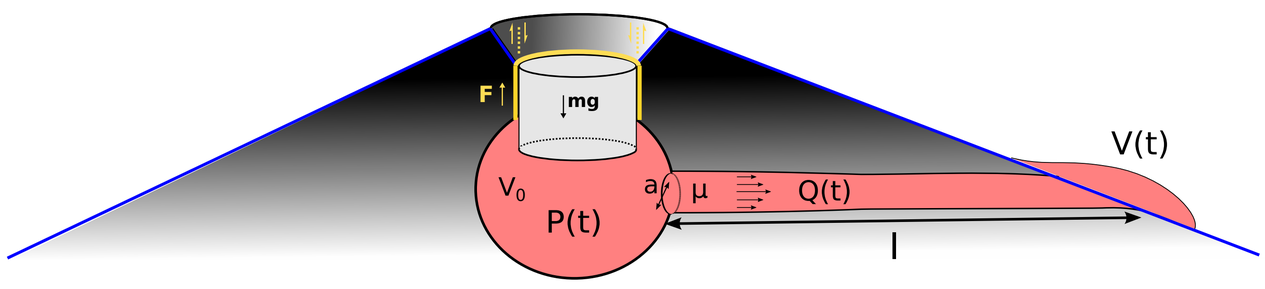
Volcanic activity forecasting is moving to an approach based on deterministic physical models, which allow to make quantitative predictions on the evolution of the system. As magma moves in the crust it deforms the encasing rocks and the Earth surface, making geodetic observations one of the most valuable tools for volcano montioring. Physical models must thus couple the dynamics of magma transport with the mechanics of rocks deformation in order to allow for accurate, consistent predictions.

Problem: The processes associated with large eruptions are not accounted by avalaible models, making our understanding of such events limited.
The 2018 Kilauea eruption provides a unique case study. It lasted 3 months and produced approximately one cubic kilometer of lavas, becoming the largest eruption in the last 200 years. Kilauea is the best instrumented volcano in the world and the eruption has been monitored by ALOS-2, SENTINEL-1 and GLISTIN-A missions, which provide a high-quality data-set.

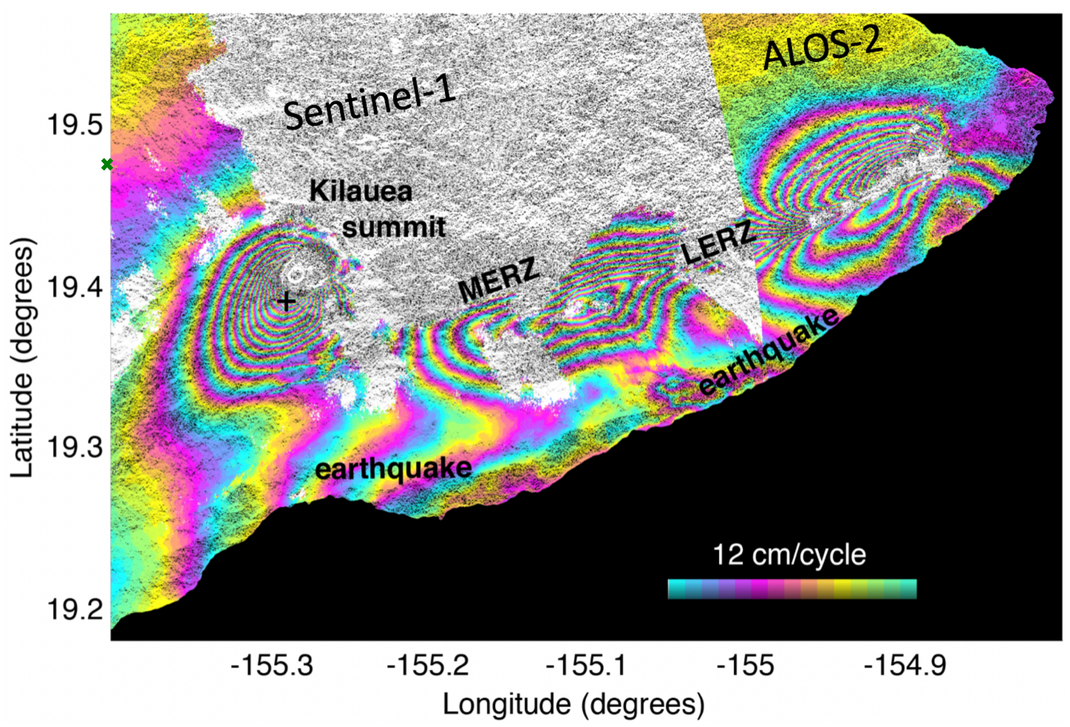
Objective: our goal is to combine ground and space-based geodetic observations with a new physical model to understand the dynamics of the Kilauea 2018 eruption. The model is used to constrain the main properties of the Kilauea plumbing system, but can be easily adapted to other large, caldera-forming eruptions.



3. Model



2. Data



Governing equations

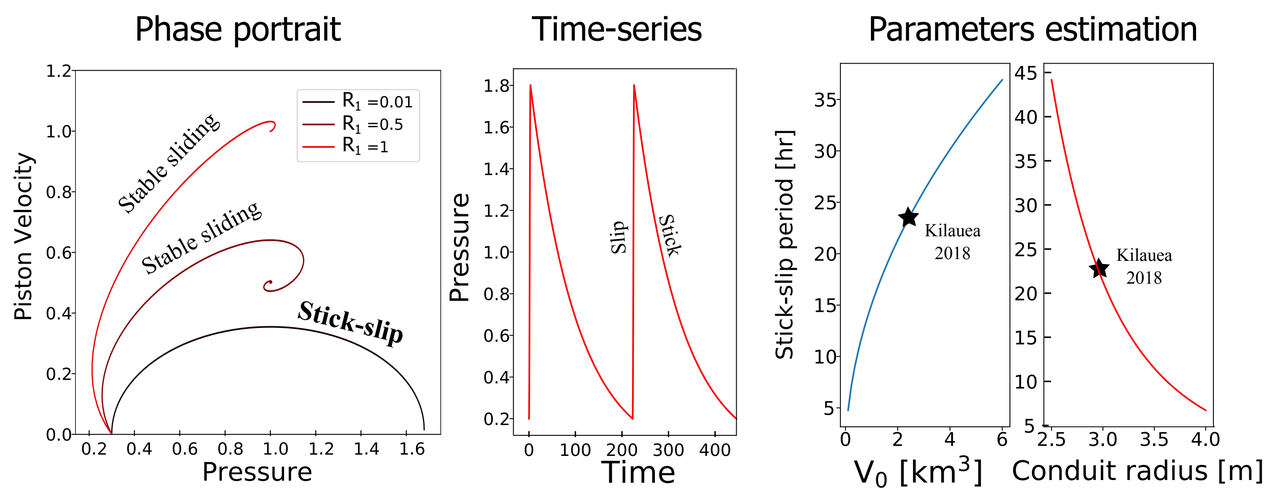
$$\begin{cases} \frac{dx}{dt} = v \\ m\frac{dv}{dt} = mg - F - pS \\ \frac{dp}{dt} = \frac{kS}{V_0}v - \frac{k\pi a^4}{8V_0\mu l}p \end{cases}$$

Static and dynamic friction coefficient

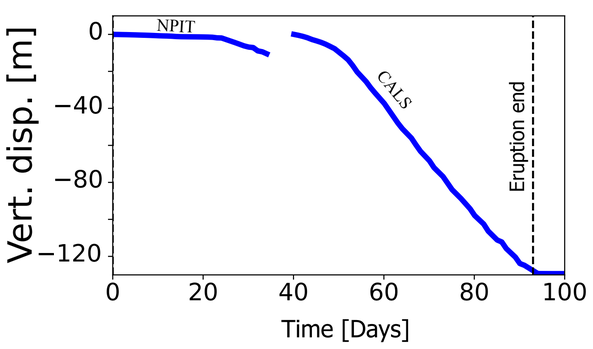
$$F = \begin{cases} F_s & v=0 \\ F_d & v\neq 0 \end{cases}$$

R_1 dimensionless damping factor

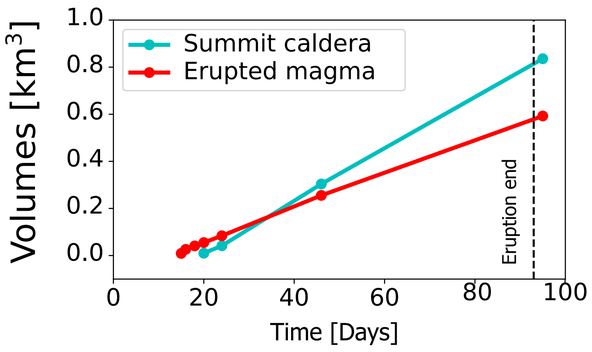
$$R_1 = \frac{\pi a^4}{8\mu l S}\left(\frac{km}{V_0}\right)^{1/2}$$



GNSS network: caldera displaments



GLISTIN derived volumes time series



4. Conclusions

1) Large volcanic eruptions enter in a particular regime which is dominated by caldera collapse

2) Caldera collapse is characterized by oscillatory (stick-slip) behavior with well defined periods

3) Dynamical modeling shows that the period of the stick-slip motion is controlled by the mechanical and geometrical parameters of the volcanic plumbing system

4) For the 2018 Kilauea eruption we estimate a chamber volume of 2 km^3 and a conduit radius of about 3 m

National Aeronautics and Space Administration

Jet Propulsion Laboratory
California Institute of Technology
Pasadena, California

www.nasa.gov

Copyright 2019. All rights reserved.

EA-08

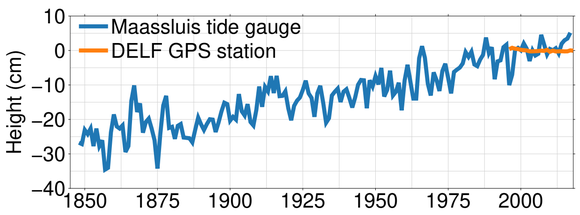
National Aeronautics and Space Administration

The impact of contemporary mass redistribution on sea-level and vertical land motion observations

Thomas Frederikse (329C), Felix Landerer (329C), and Lambert Caron (329C)

Sea-level observations are contaminated by local vertical land motion, and GPS records are rather short

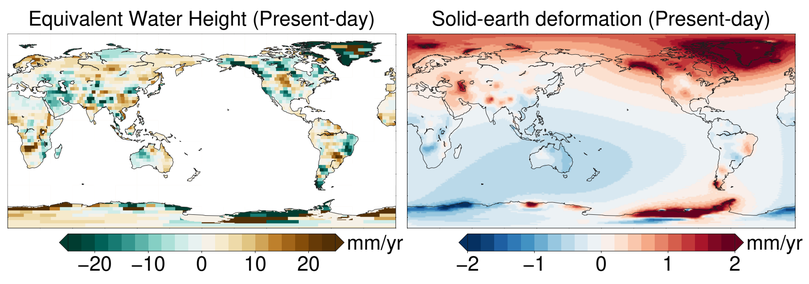
- Tide-gauge data are used for many oceanographic, geophysical purposes and sea-level reconstructions, but they are affected by land motion.
- Short (~10 years) GPS records are commonly used to correct tide-gauge data (Multi-decadal records).



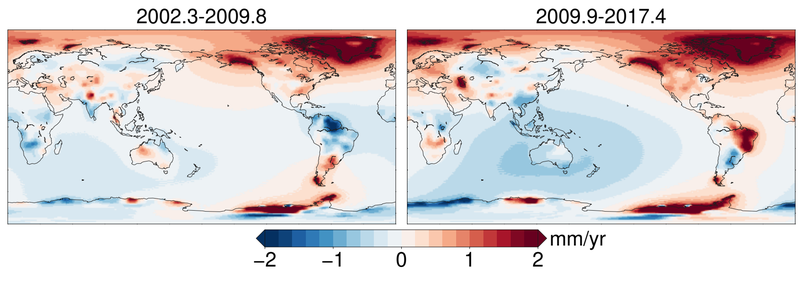
- Can we just use the short GPS record to correct the long tide-gauge, or can we do a better job?
- What we should do: correct for as much processes that make this extrapolation inaccurate.

Contemporary mass redistribution causes vertical land motion. Can we use GRACE to measure and remove this process?

- Global water redistribution causes deformation of the surface. We can use GRACE to measure this redistribution and compute the resulting deformation.



- Over the GRACE era (2002 – 2017), mass redistribution caused large uplift signals, mostly due to ice mass loss.
- How constant is this this rate with time? The below figure shows the solid-earth deformation rates over the first and second half of the GRACE time span.



- The differences are substantial. Given that 8 years is a typical GPS record length, extrapolating an 8-year rate could lead to significant biases.

Take-home messages

1. **Elastic deformation causes substantial vertical land motion**
2. **Extrapolating GPS records can thus lead to errors**
3. **We have a data set with corrected VLM rates**
4. **With these updated rates, we can reconcile long tide-gauge observations and 20th-century sea-level reconstructions**

National Aeronautics and Space Administration

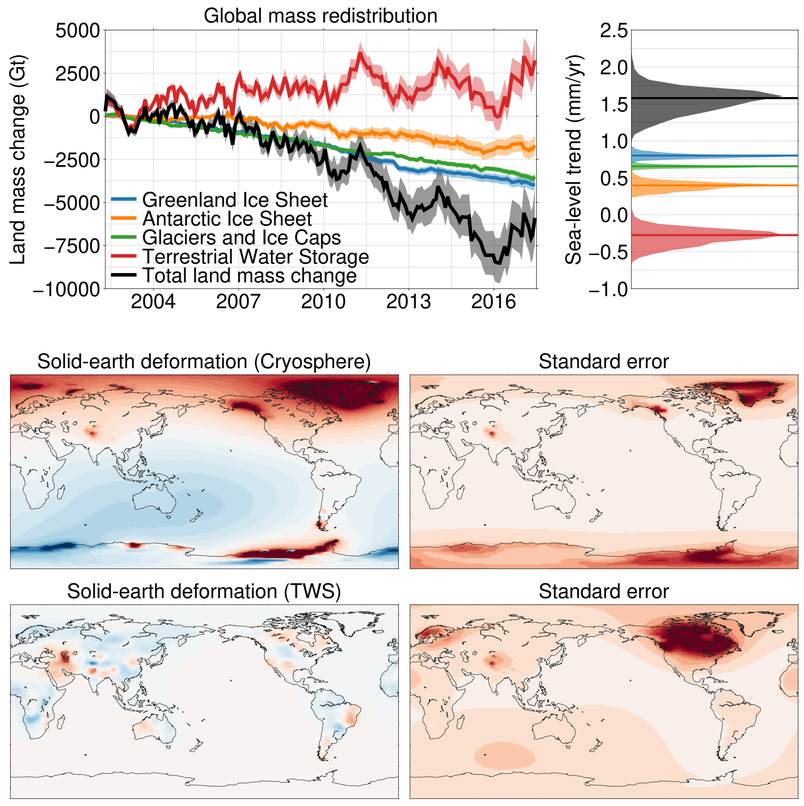
Jet Propulsion Laboratory
California Institute of Technology
Pasadena, California

www.nasa.gov

Copyright 2019. All rights reserved.

Which processes are responsible for this deformation?

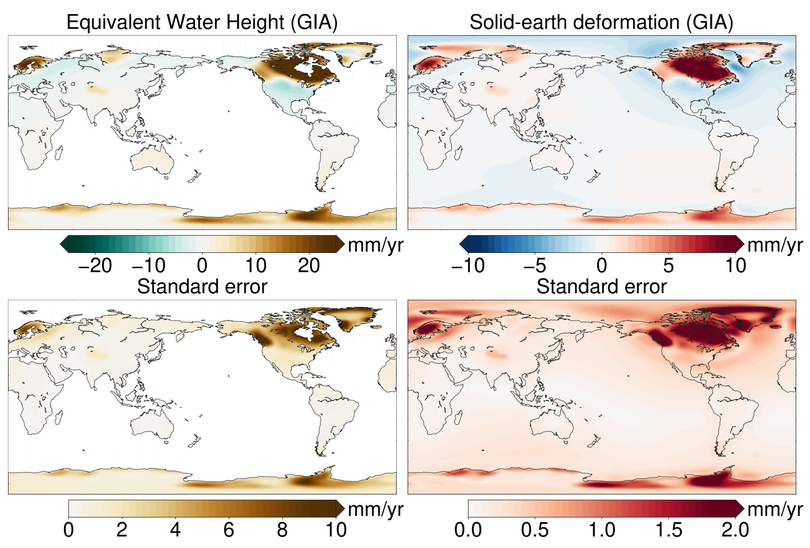
- The figure below shows the total land mass change per component, as well as the resulting deformation



- The trends are mostly due to glaciers and ice sheets, but decadal variability is dominated by terrestrial water storage (TWS)
- The ongoing ice mass loss is not representative for deformation during the centennial tide-gauge record
- Decadal variability due to TWS changes even affects rates over the GRACE period

Uncertainty and the role of Glacial Isostatic Adjustment

- Glacial Isostatic (GIA) affects both GRACE observations and causes vertical land motion, but its contribution is uncertain.
- We use a large ensemble of GIA models to estimate the mean corrections, and to derive robust uncertainties

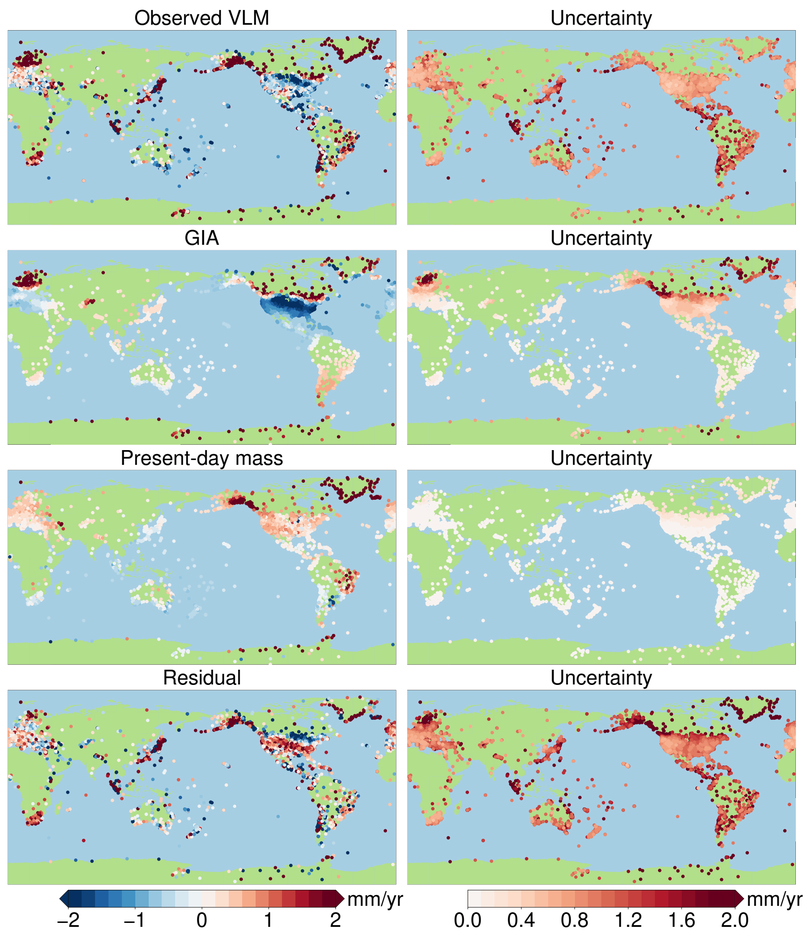


Can we avoid the bias due to elastic deformation when extrapolating GPS records?

- We can separate the observed VLM into GIA, elastic deformation, and all other sources:

$$VLM_{observed} = VLM_{GIA} + VLM_{elastic} + VLM_{residual}$$

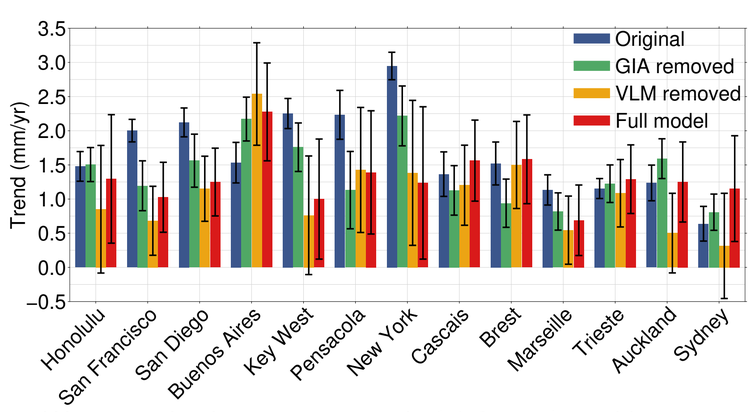
- We can compute the linear trend in $VLM_{residual}$ instead of $VLM_{observed}$
- This avoids the extrapolation bias due to elastic deformation
- We compute trends from GPS records in the Nevada Geodetic Laboratory database using the MIDAS trend estimator.
- Errors quantified using the Monte-Carlo approach



- Deformation from contemporary mass redistribution explains substantial fraction of observed trends in South America and parts of Asia.

This process affects estimates of GMSL changes

- An ongoing discussion in the sea-level community is on why long tide-gauge records are not in agreement with global sea-level reconstructions.
- Correcting tide gauges for residual VLM improves the agreement and reduces the inter-station spread



- We now obtain a mean trend of 1.3 mm/yr, with a spread of 0.4 mm/yr of these long records, which is now in agreement with recent sea-level reconstructions, which give a 20th-century rate of about 1.2 mm/yr.

EA-09

National Aeronautics and Space Administration

Assessing the Effects of Drought on Irrigation Demand using Satellite Observations

Author: Alireza Farahmand (329E)

Ali Behrangi[1], Amir AghaKouchak[2]

1) University of Arizona 2) University of California, Irvine

Introduction

- Droughts can pose a significant threat on irrigation demand in irrigated regions
- The irrigation water demand is fundamental for agricultural water management given that agricultural irrigation is the second largest user of water in the United States
- Several studies have been developed for linking irrigation water demand to environmental conditions. These models are generally either conceptual or statistical . Generally, statistical methods have much fewer data requirements and have shown to be an effective tool for assessing the effects of droughts irrigation water demand
- However, these models are either deterministic or offer probabilistic results via a single irrigation demand distribution function that incorporates all the possible climate conditions experienced during a specific month or growing season
- In contrast, policy makers might prefer a model that produces irrigation water demand distributions based on a specific environmental condition (e.g., temperature or water vapor amount) that is observed (or expected) for a given month or growing season
- Here, we introduce a new model capable of producing such irrigation demand distributions which relies on a copula-based, multivariate statistical technique and the concept of conditional probability

Datasets

- GLDAS (Global Land Data Assimilation System) Soil Moisture *0.25 °*
- MERRA (Modern-Era Retrospective analysis for Research and Applications) Relative Humidity and Temperature *0.5° * 0.625°*
- Global Precipitation Climatology Project (GPCP) Precipitation *0.5 °*
- Global Food Security Support Analysis Data (GFSAD) Crop Mask 2010 *1 km*
- Annual Texas Irrigation Water Use 1984-2015
- Re-gridded Spatial Resolution: 0.25 degree
- Temporal Resolution of hydrologic data: Monthly
- Data Length: 1984-2015

$VPD = c1 \times \exp\left(\frac{c2 \times T_{mean}}{c3+T_{mean}}\right) - \ c1 \times \exp\left(\frac{c2 \times Td_{mean}}{c3+Td_{mean}}\right)$, where $c1 = 0.611$ kPa, $c2 = 17.5$, $c3 = 240.978$ ° c, Td_{mean}: dew point temperature ° c, T_{mean}: air temperature ° c

Methodology

The Empirical Gringorton probability:

For SM, VPD and RH, and P

$$p(x_i) = \frac{i - 0.44}{n + 12}$$

i Rank of data from the smallest

n Sample size

x Data vector

For: (P, SM), (RH,SM), (VPD, SM)

$$p_j(x_k, y_k) = \frac{m_k - 0.44}{n + 12}$$

m_k Number of occurrences of the pair (x_i, y_i) for $x_i \le x_k$ and $y_i \le y_k$

n Sample size

$$SI = \phi^{-1}(p(x_i))$$

ϕ Standardized normal distribution function, SI Standardized Index

$$p(x1 \mid x2 = \mathrm{DI}) = c(x1, x2).p(x1)$$

$x1$: $Irrigation\ Demand$, $x2$: $Drought\ Indicator$

$p(x1)$: PDF of Irrigation Demand

$c(x1, x2)$: Copula of Irrigation Demand and Drought Indicator

$p(x1 \mid x2)$: Conditional Probability of Irrigation Demand Given x2=SI

Results

- Table 1 shows the correlation between annual irrigation water use and mean of June-September drought indicators. As seen the drought indicator of combination of soil moisture and relative humidity result in highest correlation of -0.56

Variable	Correlation
Soil Moisture (SM)	-0.55
Relative Humidity (RH)	-0.5
Vapor Pressure Deficit (VPD)	0.49
Precipitation (P)	-0.4
(SM,VPD)	-0.51
(SM,RH)	-0.56
(P,SM)	-0.54

Table 1: Correlation of Annual Water Use with Average Summer Drought Indicator

- In top panel of figure 2, we can see the time-series of annual irrigation water use in the state of Texas during the 1984-2015 time period. In the bottom panel, we can see the time series of drought indicator of SM and RH for the same time series. As shown, there is a clear relationship between water use and drought condition. The lower the drought indicator (hence higher more intense drought condition), the higher the water use.

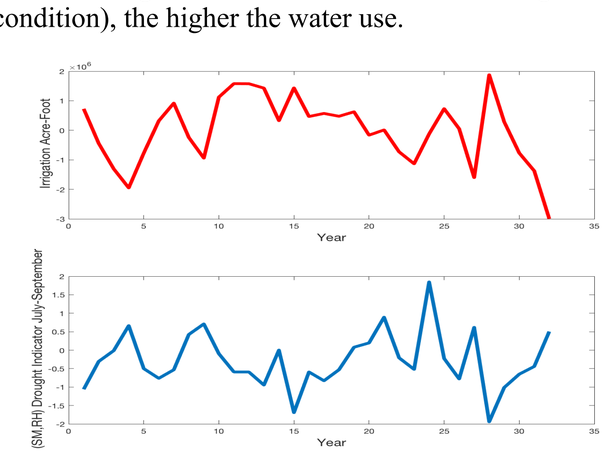
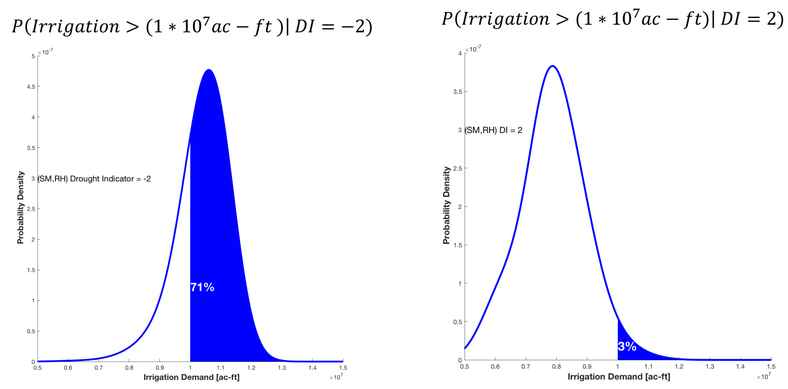


Figure 1: Time series of Annual Irrigation Water Use and Drought Condition

- Figure 2 shows the probability distribution functions of irrigation water demand given a dry (DI=-2) and a wet (DI=2) condition. The hatched area shows the probability of irrigation demand above10^7 acre feet of water.



Dry Condition **Wet Condition**

Figure 2: PDF of irrigation water demand given a dry (DI=-2) and a wet (DI=2) condition

Conclusion

- Droughts and high evapotranspiration rates (e.g., caused by high temperatures) can pose a significant threat on irrigation demand in irrigated regions.
- This study evaluated multiple drought indicators for assessing the effects of drought on irrigation demand. The drought indicator of soil moisture and relative humidity has the best relationship with irrigation water use
- We introduced a copula-based methodology to generate probability distribution functions of irrigation water demand given various drought condition

National Aeronautics and Space Administration

Jet Propulsion Laboratory
California Institute of Technology
Pasadena, California

www.nasa.gov

Copyright 2019. All rights reserved.

Poster No. EA-10

National Aeronautics and Space Administration

Regime-Dependent Differences in Active Satellite Rainfall Products

Author: Ethan L. Nelson (329E)
Advisor: Matthew D. Lebsock (329J)

Motivating Questions

1. Do spaceborne radars at different frequencies retrieve similar distributions of rainfall in middle latitudes?
2. If not, how do they vary by environmental regime?

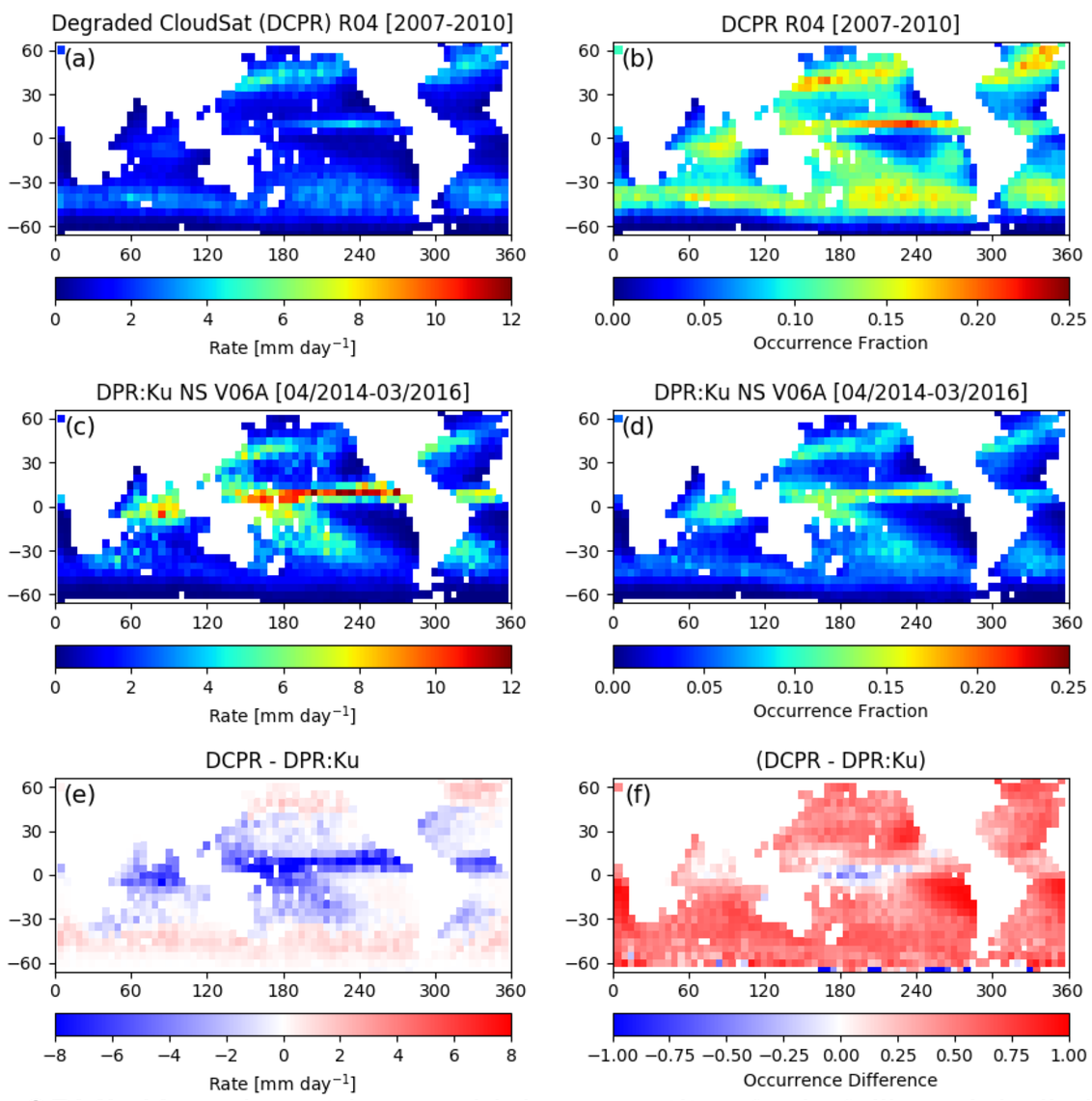
Background

- Water is a critical resource for society and nature.
- Rainfall couples Earth's energy budget and atmospheric circulations.
- Models poorly represent rainfall, **so we need better observations of rainfall to improve future climate projections** (Stephens et al. 2010).
- NASA's global spaceborne precipitation sensing system consists of many passive sensors trained on Ku-band radar observations.
- It has been documented in the tropics that, while these radars can sense heavy precipitation, they cannot sense lighter precipitation because of their low frequency and large footprint (Berg et al. 2010).
- Here we extend that prior to work to middle latitudes in the context of our two motivating questions.

Methods

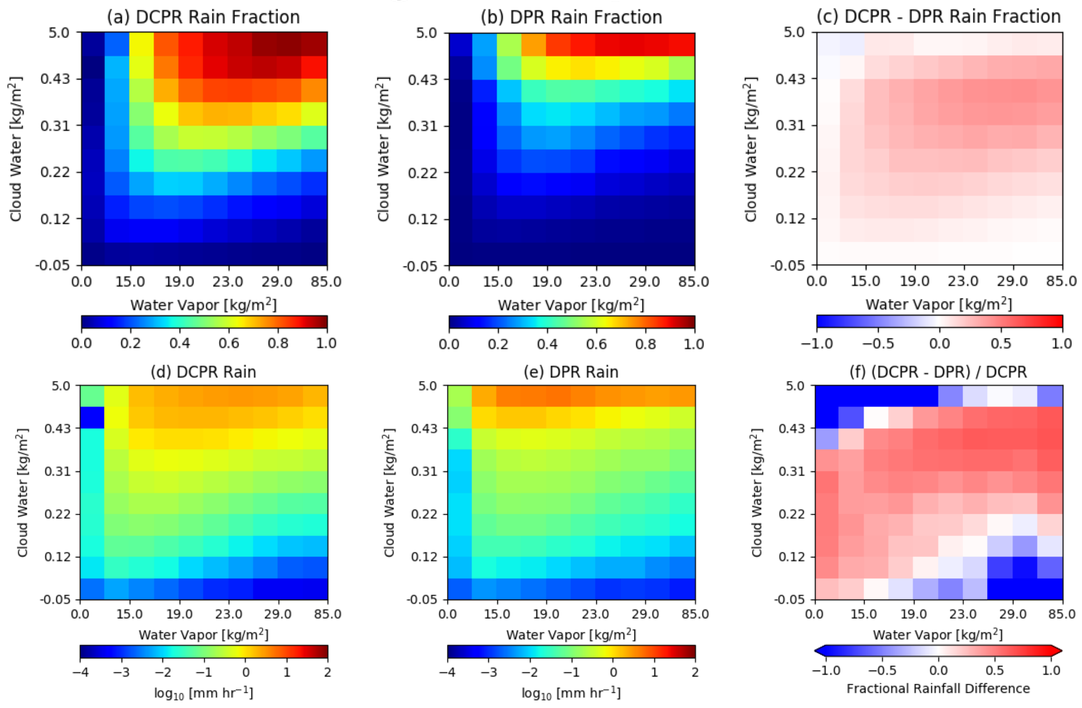
- Rainfall data is taken from the GPM Ku-band precipitation radar.
- CloudSat's W-band radar, sensitive to clouds and light precipitation, provides rainfall intensity and occurrence data for comparison.
- Environmental data is available from Remote Sensing Systems using microwave imagers nearly collocated with each radar.

Global Retrieved Rainfall Distributions



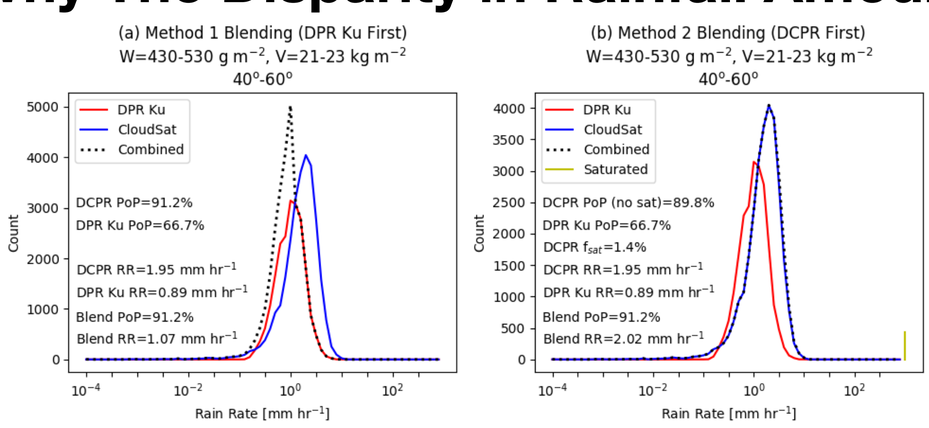
- GPM's Ku radar retrieves a higher quantity of rain falling globally but not in the midlatitudes.
- CloudSat retrieves rain occurring more often than GPM's Ku radar in the midlatitudes and nearly globally.

Regime Dependence



- Environmental regime allows us to examine similar types of rainfall despite different radar orbits.
- Water vapor provides information on rain location around fronts, while cloud liquid water informs about the density of clouds.
- **CloudSat sees rain occurring more often in nearly all regimes**—and especially in smaller cloud liquid water paths (0.31-0.43 kg m^{-2}).
- CloudSat retrieves higher rainfall amounts in all regimes but high cloud water/low water vapor and low cloud water/high water vapor.

Why The Disparity in Rainfall Amounts?



- In this example regime, differences exist in the rain rate distribution.
- **Even at moderate rainfall rates (~1 mm hr^{-1})** where both sensors should ideally retrieve the same distribution, **the sensors differ**.
- Attempts to reconcile the two sensors—either by raising GPM precipitation occurrence with CloudSat or accounting for CloudSat saturation with GPM—do not yield an improvement.

Discussion

- CloudSat observes precipitation falling more often and of an overall larger amount than GPM's Ku radar in the midlatitudes.
- This mostly occurs in moderate environmental regimes.
- Some differences in the two radars stem from instrument sensitivity since they observe rain occurrence differently.
- But differences in the magnitude of rainfall likely arise because these satellites use different radars at different frequencies with different algorithms that have different microphysical assumptions.
- This motivates the need for a combined low/high frequency radar platform to leverage strengths of each in a unified algorithm.

References

1. Stephens et al. (2010) *JGR*, doi:10.1029/2010JD014532.
2. Berg et al. (2010) *JAMC*, doi:10.1175/2009JAMC2330.1.

National Aeronautics and Space Administration
Jet Propulsion Laboratory
California Institute of Technology
Pasadena, California

www.nasa.gov

Poster No. EA-11

Copyright 2019 California Institute of Technology. All rights reserved. Government sponsorship acknowledged.

National Aeronautics and Space Administration

Evaluation of Available Global Runoff Data in South and Southeast Asia

Md. Safat Sikder[1*] (329F), Cédric H. David[1] (329F), George H. Allen[2], Xiaohui Qiao[3], E. James Nelson[3], Mir A. Matin[4]

[1]Jet Propulsion Laboratory, California Institute of Technology; [2]Texas A&M University; [3]Brigham Young University; [4]International Centre for Integrated Mountain Development

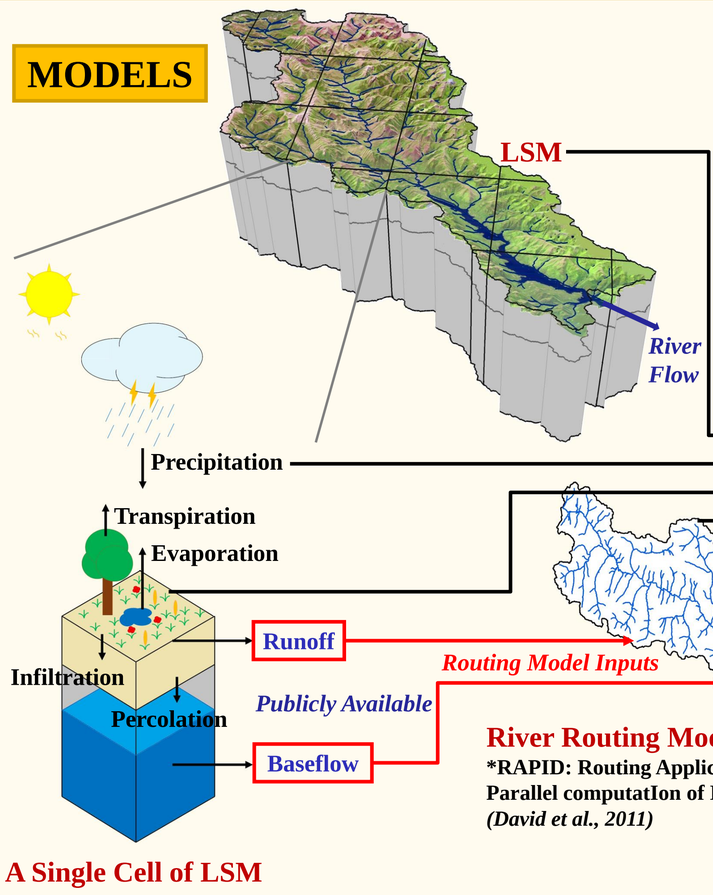
INTRODUCTION

- Hydrologic outputs from global Land Surface Models (LSMs) are widely available and represent valuable alternatives for supporting water management in ungauged river basins where observations are scarce.
- Outputs from these models can help to prevent large-scale disasters in transboundary river basins in South and Southeast Asia where data sharing is limited.
- The wide range of existing model outputs makes the choice of dataset challenging in the absence of detailed model validation in that region.

OBJECTIVES

- Identify optimal global LSMs for estimating river flow in the Ganges-Brahmaputra-Meghna (GBM) and the Mekong river basin located in South and Southeast Asia, respectively.
- A secondary goal is to identify the most sensitive factors affecting the accuracy of the simulated flow among a) the choice of the LSM, b) precipitation input, c) spatio-temporal resolution of the models, and d) routing model parameters.

MODELS & METHODS

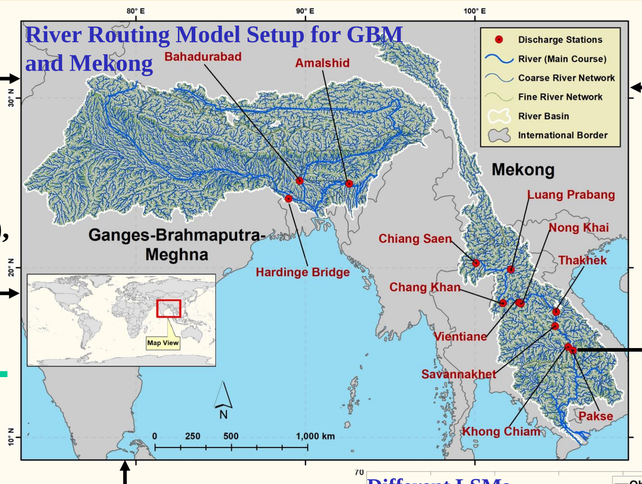


LSMs: CLM, Noah, Mosaic, VIC, ECMWF-ERA-Interim/Land

Routing Model Parameters: Flow Wave Propagation Time (k), Muskingum Dimensionless Diffusion Coefficient (x)

Accuracy Depends:
- LSMs
- Input Precipitation
- Model Resolution
- Model Parameter

Accuracy of Simulated River Flow in Comparing with the Observed?

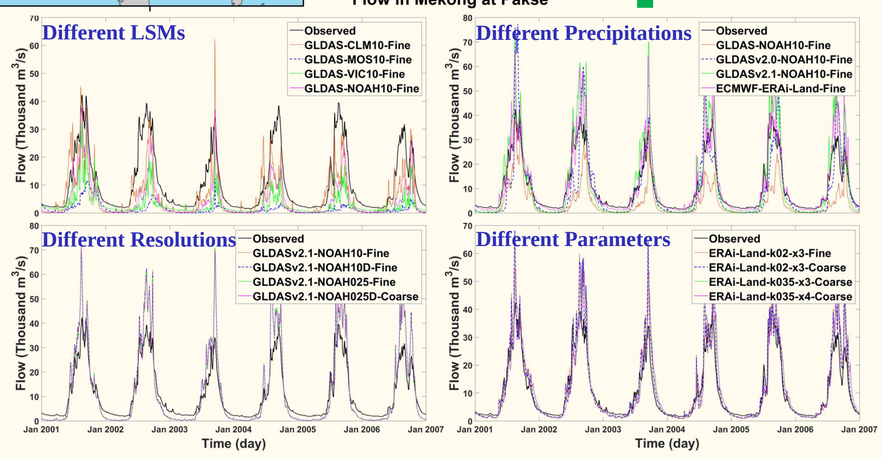


LSM resolution: 3-hour, 1-day & 0.25˚ , 1˚
Routing Model Resolution: ~5 km, ~20 km (average reach length)

METHODS

Accuracy of Simulated Flow: Correlation Coefficient, Nash–Sutcliffe Efficiency, Root Mean Square Error, Bias, Standard Error, Lagged Cross-Correlation

Input Precipitation: GLDAS, GLDASv2.0, GLDASv2.1, ECMWF-ERA-interim



RESULTS

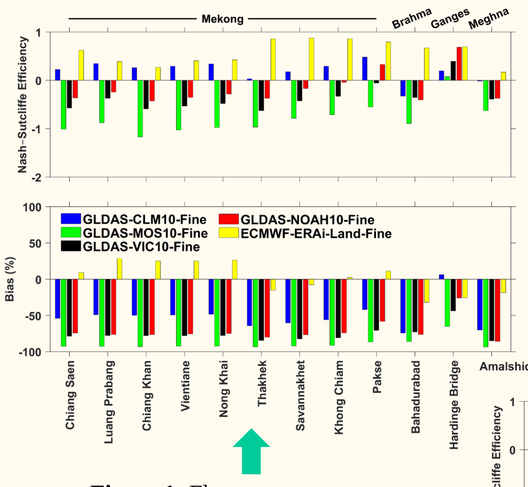


Figure 1: Flow accuracy as a function of different LSMs

ECMWF is superior in most cases

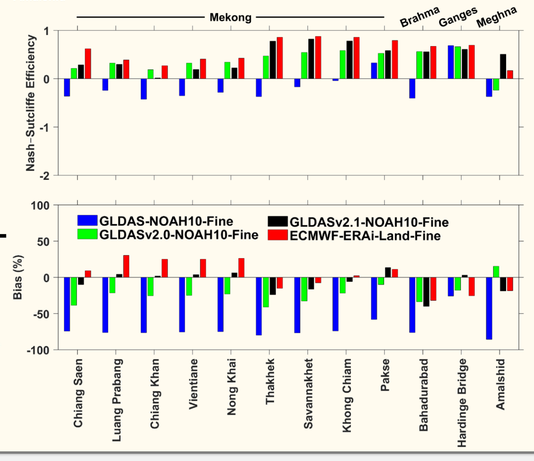


Figure 2: Flow accuracy as a function of different precipitation inputs

High NSE and Low Absolute Bias: More Accurate Simulation

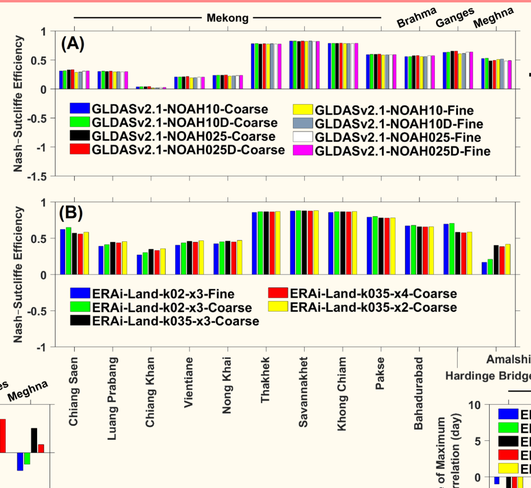


Figure 3: Flow accuracy as a function of different (A) model resolutions, (B) routing model parameters

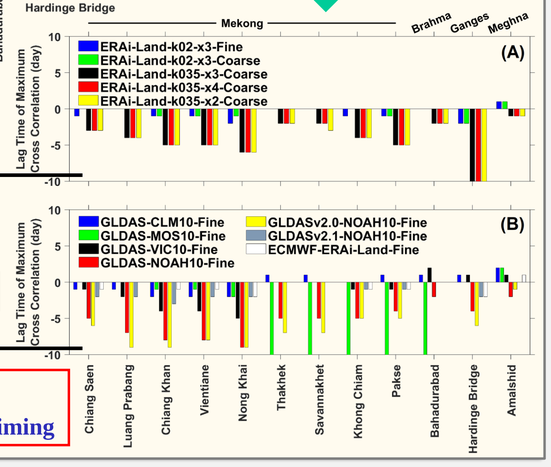
Resolutions and Parameters are less sensitive factors

Figure 4: Lag time corresponding to the maximum cross-correlation as a function of different (A) routing model parameters, (B) LSMs and precipitation inputs

Parameter, k can be used to fine-tune the hydrograph timing

Timing of ECMWF is better

Lag Time Close to Zero: Better Match in Hydrograph Timing



CONCLUSIONS

- ECMWF's ERA-Interim/Land outperforms all other LSMs.
- Selection of LSM and precipitation input are the most sensitive factors affecting the river flow.
- Routing model parameters are not much sensitive as the above two factors, but "k" can be used to fine-tune the hydrograph timing.
- The findings are expected to help water managers in the region while also supporting further development of models.

National Aeronautics and Space Administration
Jet Propulsion Laboratory
California Institute of Technology
Pasadena, California

www.nasa.gov

References:

- Davie et al., (2011), River Network Routing on the NHDPlus Dataset, *Journal of Hydrometeorology*, 12(5), pp: 913–934.
- Sikder et al., (2019), Evaluation of Available Global Runoff Datasets through a River Model in Support of Transboundary Water Management in South and Southeast Asia, *Frontiers in Environmental Science*. [***in review***]

*Contact:
Md. Safat Sikder
md.safat.sikder@jpl.nasa.gov
orcid.org/0000-0002-1910-1800

Poster No. EA-15

Copyright 2019. All rights reserved.

National Aeronautics and Space Administration

Constraining carbon fluxes in northern regions by combining constraints from multiple atmospheric CO2 observing systems

Author: Brendan Byrne (329G)
Junjie Liu (329G), Meemong Lee (329I), Ian Baker (Colorado State University), Kevin W. Bowman (329G), John S. Kimball (University of Montana), Charles E. Miller (329G), Nicholas C. Parazoo (329G)

Introduction

Estimates of CO2 fluxes at Earth's surface can be obtained from measurements of atmospheric CO2 using flux inversion methods. The recent launch of space-based missions that measure column-averaged dry-air mole fractions of CO2 (XCO2) has greatly increased the number of atmospheric CO2 measurements that can be used to estimate CO2 fluxes. However, at high latitudes the observational coverage of the space-based XCO2 measurements is highly seasonal (Fig. 1).

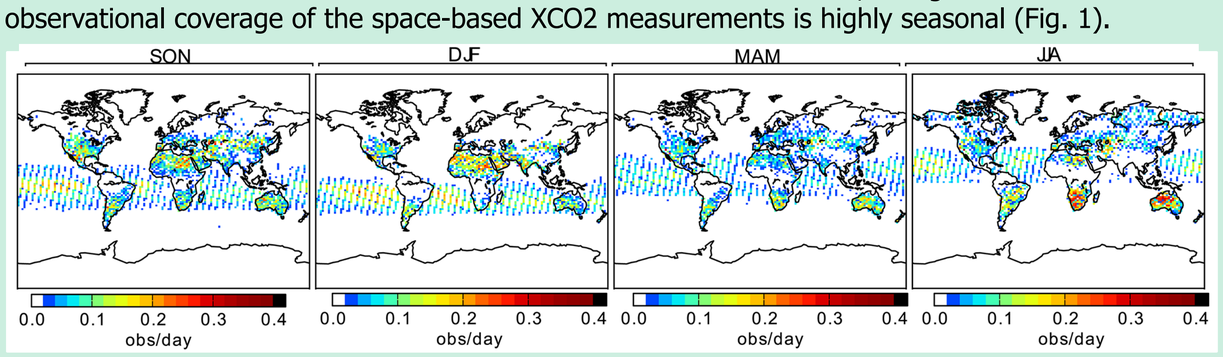
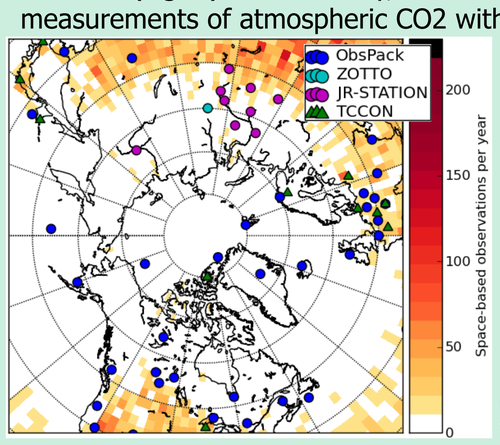


Figure 1. Number of measurements per day for GOSAT. Each subplot shows the number density of measurements for a given meteorological season

Luckily, there are a number of ground-based sites measuring atmospheric CO2 at high northern latitudes (Fig. 2). In this study, we examine the feasibility of combining ground-based and space-based measurements of atmospheric CO2 within a single flux inversion framework. Specifically, we ask:



1. Does combining ground-based and space-based atmospheric CO2 constraints within a flux inversion framework improve the agreement between posterior CO2 estimates and aircraft CO2 measurements?
2. How precisely can the seasonal cycle of net ecosystem exchange (NEE) be estimate on regional scales in northern regions from atmospheric CO2 measurements?

Figure 2. Locations of ObsPack (blue circles), ZOTTO (cyan circle), JR-STATION (magenta circles), and TCCON (green triangles) sites. The number of observations from space-based observing systems (GOSAT+OCO2) per year are also shown.

Data and Methods

We perform a series of flux inversions with GHGF-Flux. All flux inversions are performed using 4-dimensional variational (4-DVar) assimilation to optimize 14-day NEE and ocean fluxes over 2010-2015. For all inversions, we prescribe ODIAC fossil fuel emissions, CASA-GFED4-FUEL biofuel emissions, GFED4 biomass burning emissions, and ECCO-Darwin prior ocean fluxes. The flux inversions differ in the prior 14-day NEE fluxes and data-sets assimilated.

Assimilated data:

- ObsPack GLOBALVIEW v4.1 (CGADIP, 2018). This package incorporates data from many observing sites around the world and is specifically prepared for use in data assimilation studies.
- Japan–Russia Siberian Tall Tower Inland Observation Network (JR–STATION). This is a network of nine towers, these measurements are provided as hourly means.
- Greenhouse Gases Observing Satellite (GOSAT). We use version 7.3 of the NASA Atmospheric CO2 Observations from Space (ACOS) GOSAT measurements in this analysis. We assimilate all high gain (H-Gain) nadir measurements that pass the quality flag requirement.

Evaluation of the flux inversions

It is challenging to evaluate the accuracy of posterior CO2 fluxes obtained by flux inversions. Here, we evaluate the simulated posterior atmospheric CO2 fields against independent measurements of atmospheric CO2 measurements from aircraft campaigns. In general, closer agreement between posterior CO2 and aircraft measurements suggests more accurate fluxes.

Figure 3 compares aircraft measurements over Japan to simulated CO2 for the prior fluxes, surface-data-only inversion, GOSAT-only inversion, and GOSAT+surface-data inversion. We find that (1) the surface-data inversion has the smallest mean bias (2) the GOSAT inversion best recovers the seasonal cycle and (3) the GOSAT+surface inversion well captures the seasonal cycle with a reduced mean bias relative to the GOSAT flux inversion.

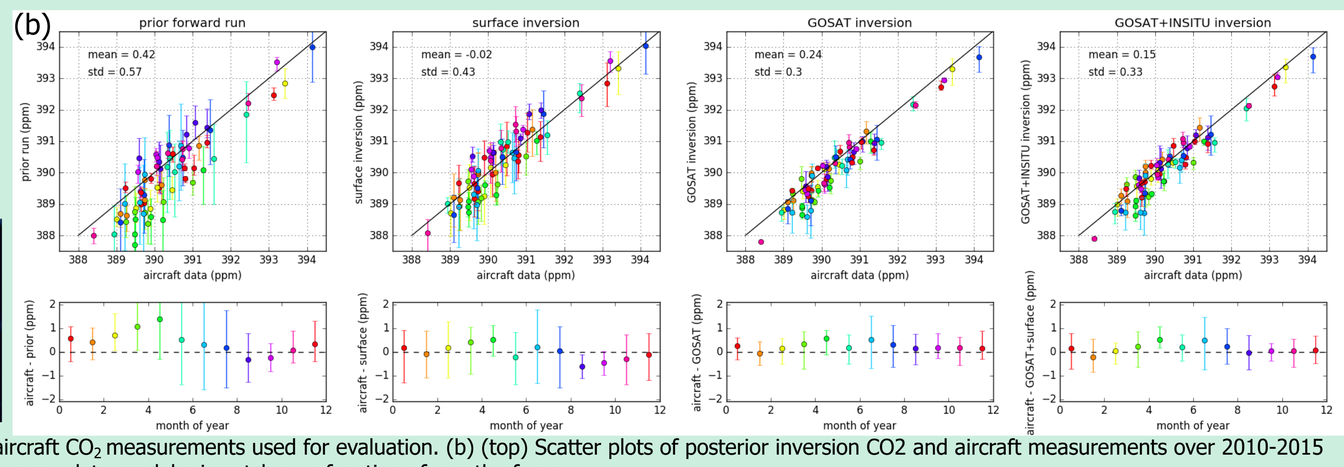


Figure 3. (a) Location of aircraft CO_2 measurements used for evaluation. (b) (top) Scatter plots of posterior inversion CO2 and aircraft measurements over 2010-2015 and (bottom) the monthly mean data-model mismatch as a function of month of year

To further examine the differences between the flux inversions, we can examine the zonal differences between the posterior fluxes and GOSAT measurements as a function of latitudes and time (Fig. 4). We find that all inversions improve agreement with GOSAT relative to the prior.

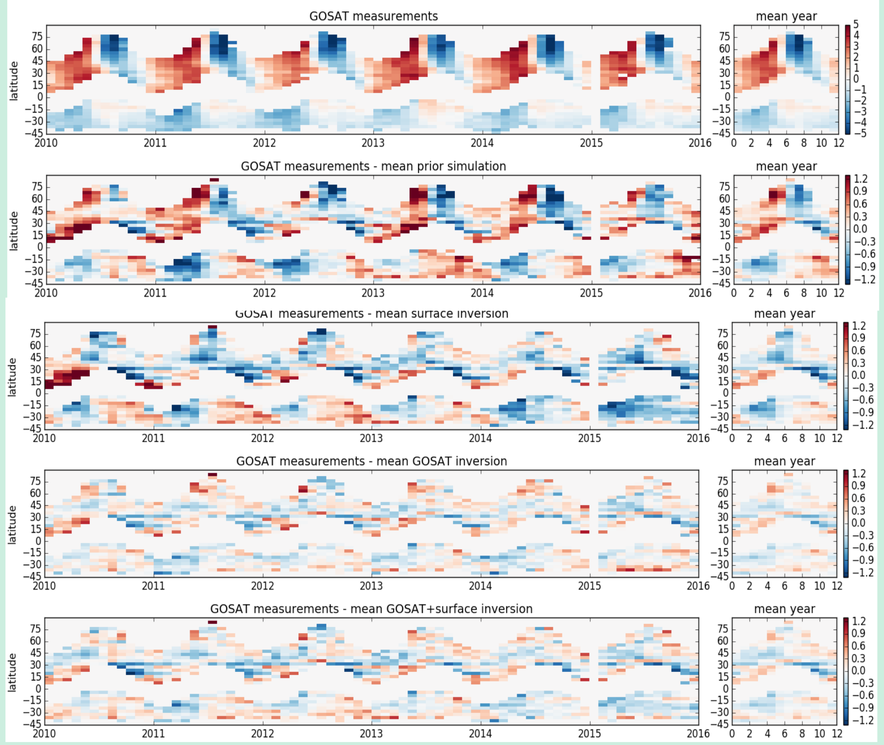


Figure 4. zonal mean mismatch between GOSAT measurements and flux inversion posterior CO2 fields as a function of latitude and time. Zonal means with less that 50 GOSAT measurements are removed.

Posterior Seasonal Cycle

We examine the seasonal cycle obtained by the flux inversions over three regions (Fig. 4). We performed three inversion using different prior fluxes and uncertainties, giving a range of posterior fluxes (giving an estimate of precision).

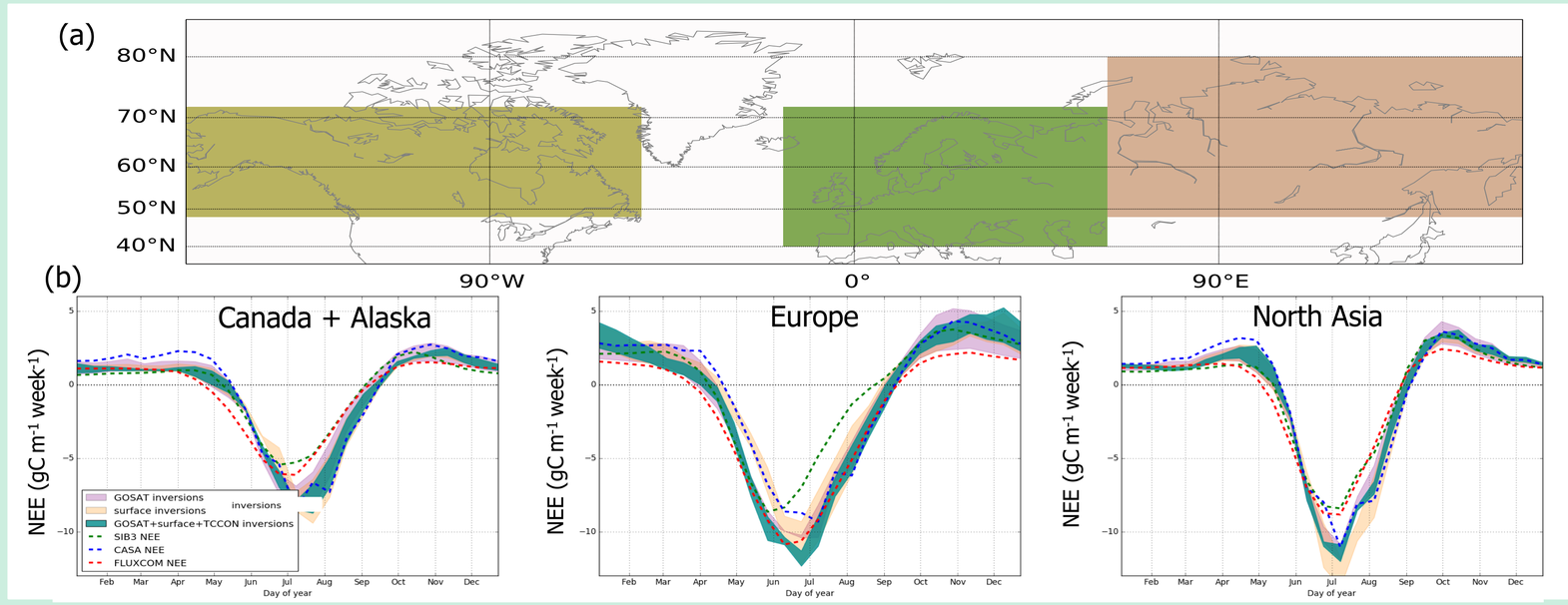


Figure 5. (a) Map showing there regions, (yellow) Canada+Alaska, (green) Europe, and (salmon) North Asia. (b) Posterior seasonal cycles of 14-day NEE fluxes for (black) the GOSAT-only inversions (magenta), surface-data-only inversions (yellow), and GOSAT+surface data inversions. The dashed lines show the seasonal cycles of the prior NEE fluxes for (green) SiB3, (blue) CASA, (red) SMAP L4C, and (orange) FLUXCOM.

Key Results

- The seasonal cycle of posterior NEE is recovered with high precision and generally falls within the model spread.
- The GOSAT+surface inversion is similar to the GOSAT-only inversion during the summer
- The GOSAT+surface inversion is similar to the surface-data-only inversion during the winter

Conclusions

- Assimilating multiple atmospheric CO2 datasets within a single flux inversion gives strong agreement between posterior atmospheric CO2 and aircraft CO2 measurements.
- The posterior NEE seasonal cycle recovered from atmospheric CO2 flux inversions is recovered with high precision, and is not very sensitive to prior NEE.
- The seasonal cycle of posterior NEE generally falls within the model spread, but does show some systematic differences, such as, a more rapid transition to drawdown during the spring.

National Aeronautics and Space Administration
Jet Propulsion Laboratory
California Institute of Technology
Pasadena, California

Acknowledgements

Brendan Byrne's research was supported by an appointment to the NASA Postdoctoral Program at the Jet Propulsion Laboratory, administered by Universities Space Research Association under contract with NASA. Resources supporting this work were provided by the NASA High-End Computing (HEC) Program through the NASA Advanced Supercomputing (NAS) Division at Ames Research Center. We are also thankful for support from NASA OCO2/OCO3 science team program.

www.nasa.gov

Copyright 2019. All rights reserved.

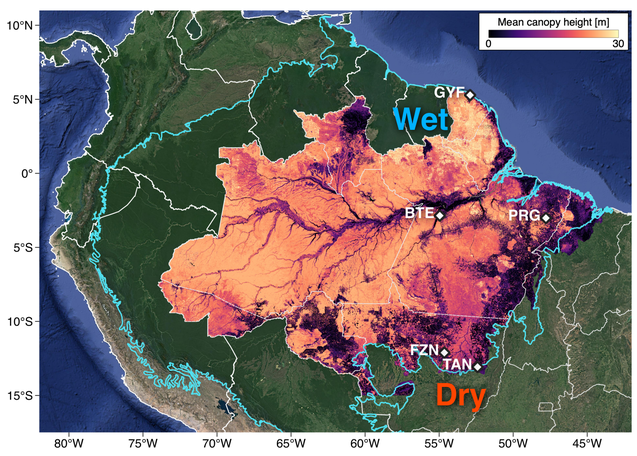
Poster No. EA-16

National Aeronautics and Space Administration

Amazon forest degradation impacts on energy, water, and carbon cycles

Marcos Longo (329G)
Sassan Saatchi (329G), Michael Keller (329G), Kevin Bowman (329G), António Ferraz (329G), Victoria Meyer (329G), Liang Xu (329G)

Introduction



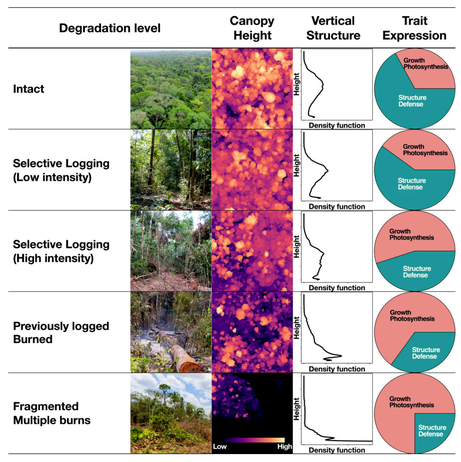


Figure 1. (a) Airborne-lidar derived canopy height across the Amazon in Brazil and French Guiana, showing regional heterogeneity (highest in S and E, where most of deforestation and degradation occurs. (b) Typical changes in forest structure and function in tropical forests[1].

Scientific questions:

- How do changes in forest structure caused by degradation impact the energy, water, and carbon cycles across the Amazon?
- Does degradation make Amazon forests more susceptible to fires?

Approach

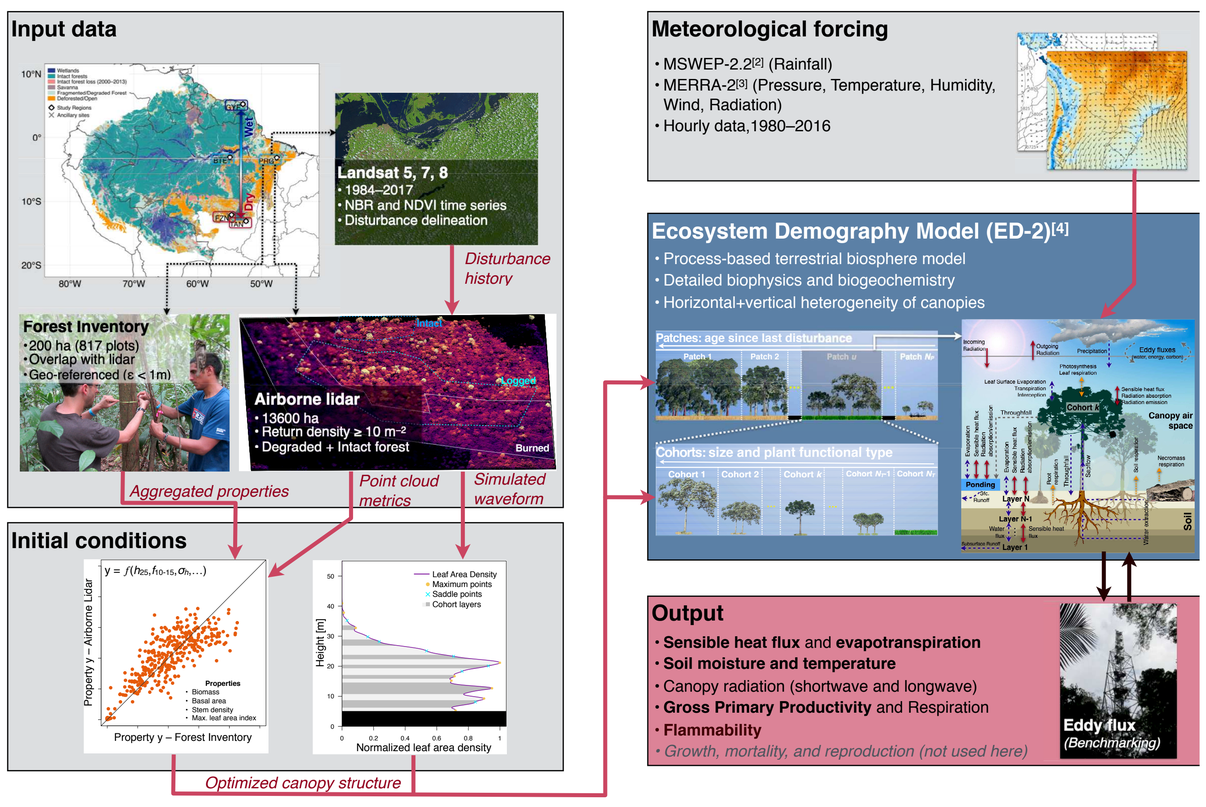


Figure 2. Overview of the integrated lidar and ED-2 model framework, used to understand the impact of tropical forest degradation on biophysical and biogeochemical cycles in the Amazon.

Initialization and model assessment

Initialization assessment (Fig. 3):

- 1000 bootstrap sampling replicates (leave region out).
- Reasonable structural change due to degradation across regions.
- Negative bias in understory of dense canopies.

Model evaluation (Fig. 3):

- Good agreement with tower's ET across rainfall gradient
- Largest biases at the driest sites and season transitions.

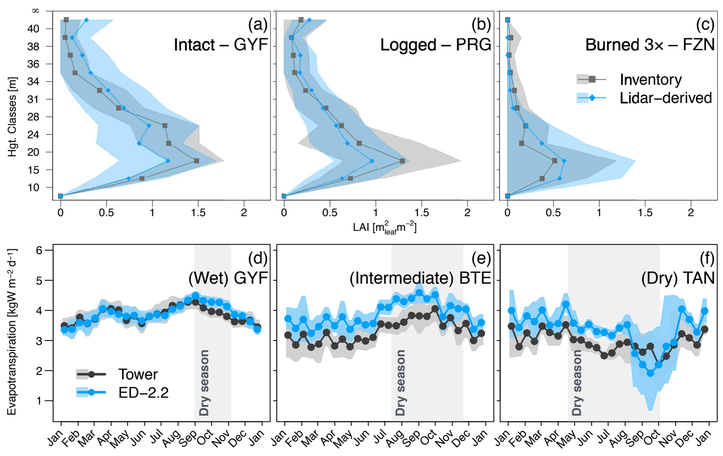


Figure 3. (a–c) Assessment of lidar initialization using cross-validation. (d–f) Evaluation of simulated evapotranspiration across the Amazon, using towers as references.

Average impacts of forest degradation

Water flux (Fig. 4).

- Intact, light degradation: Dry-season increase
- Severe degradation: dry-season reduction.

Ground Temp. (Fig. 4):

- Dry-season warming in degraded forests.
- Warming above 4°C in drier sites.

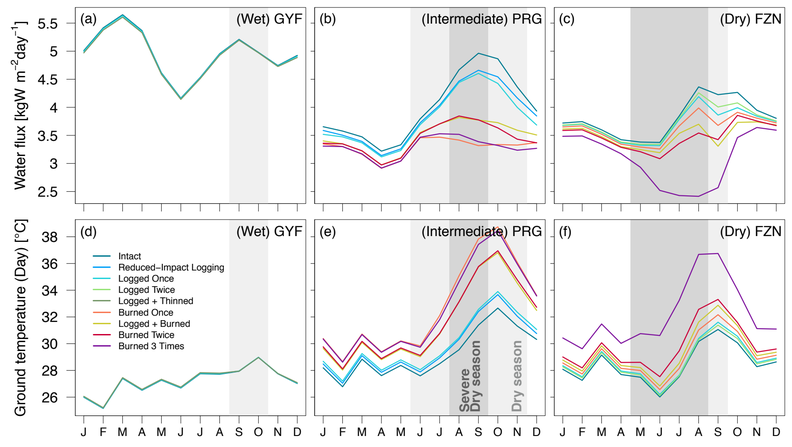


Figure 4. Long-term (1980–2016) monthly averages of (a-c) evapotranspiration and (d-f) daytime ground temperature across the Amazon region and across degradation gradients.

Interannual variability & flammability risk

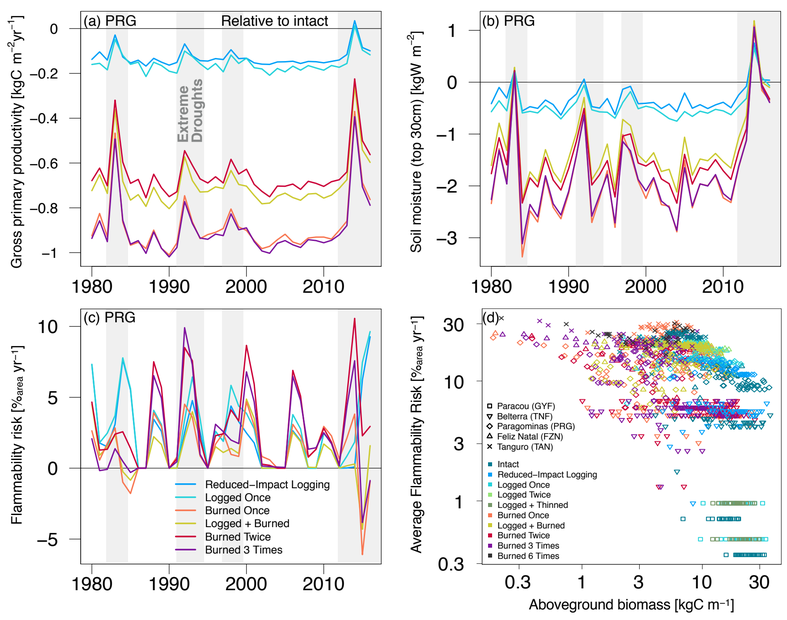


Figure 5. Relative differences in (a) GPP, (b) soil moisture, and (c) flammability in degraded forests (PRG). (d) Average flammability as a functions of biomass (proxy for forest structure).

Degradation impacts – Interannual variability:

- Typical years: GPP↓, SWC_{30cm}↓.
- Extreme droughts: degradation effects less significant.

Fire risk (Fig. 5d):

- Wet (GYF): low fire risk
- Intermediate (BTE, PRG): increased fire risk due to severe degradation.
- Dry (FZN, TAN): recurrent flammability even at low degradation.

Conclusions and future directions

Degradation effects on typical years:

- Wet season: few differences
- Dry season: T_{ground}↑, H↑, ET↓, GPP↓

Degradation impacts on flammability:

- Severe droughts: all forests are flammable;
- Moderate droughts: flammability in severely degraded forests only.

Future directions: integrate ECOSTRESS and lidar data at regionally to quantify the role of forest degradation on water and energy cycles

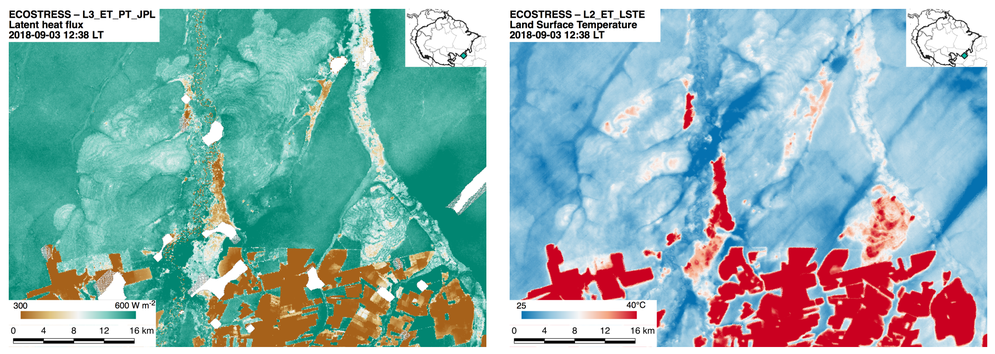


Figure 6. Impact of deforestation and degradation near midday on dry-season ET and LST in Southern Amazonia, from ECOSTRESS. Ring patterns are burned areas.

References

1. Longo M, Keller M 2019. *New Phytol.* **10.1111/nph.15636**.
2. Beck HE, *et al.* 2019. *Bull. Am. Meteorol. Soc.* **10.1175/BAMS-D-17-0138.1**.
3. Gelaro R, *et al.* 2017. *J. Climate* **10.1175/JCLI-D-16-0758.1**.
4. Longo M, et al. 2019. *Geosci. Mod. Devel. Discuss.*, doi: 10.5194/gmd-2019-45

National Aeronautics and Space Administration
Jet Propulsion Laboratory
California Institute of Technology
Pasadena, California

www.nasa.gov

Copyright 2019. All rights reserved.

Acknowledgements. This research was supported by the NASA Postdoctoral Program, administered by Universities Space Research Association under contract with NASA. Lidar and forest inventory data from Brazil were acquired by the Sustainable Landscapes project supported by the Brazilian Agricultural Research Corporation (Embrapa), USFS, USAID, and the U.S. Department of State. We thank Damien Bonal, Paulo Brando, Benoît Burban, Géraldine Derroire, Maiza dos-Santos, Scott Saleska, and Grégoire Vincent for sharing tower and additonal lidar and inventory data sets, and Joshua Fisher, Paul Moorcroft, Fabian Schneider, and Xiangtao Xu for discussions.

Poster EA–17

National Aeronautics and Space Administration

Trends and Anomalies in Global Terrestrial Gross Primary Productivity from 1982-2016

Author: Nima Madani (329G)
Nicholas C. Parazoo (329G)

Introduction

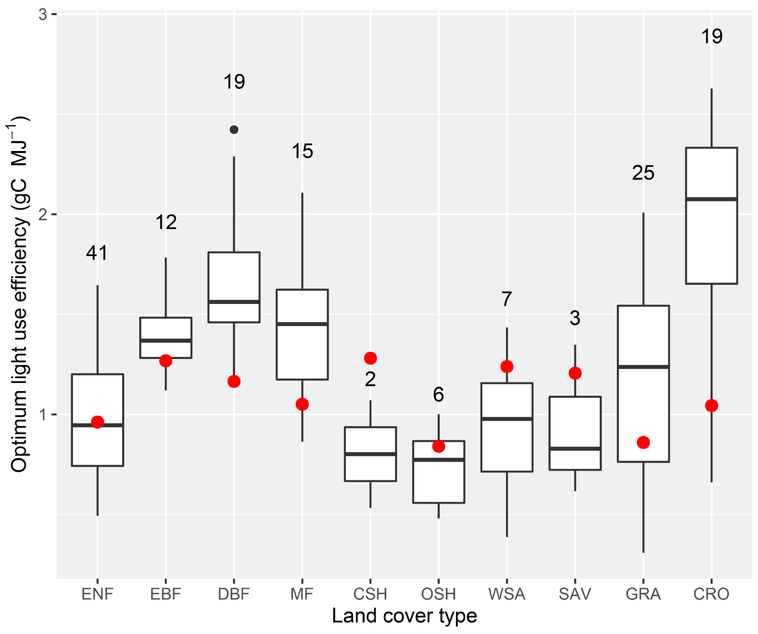
Global terrestrial ecosystem Gross Primary Productivity (GPP) constitutes the largest land-atmosphere annual carbon flux and the primary mechanism of photosynthetic fixation of atmospheric CO_2 into plant biomass. Despite the importance of GPP:

- There is a large uncertainty in current model based GPP assessments that contributes to its spatial and temporal variability, and climate sensitivity.
- The effect of climate and its role on long term trend in ecosystem productivity is not well assessed yet.

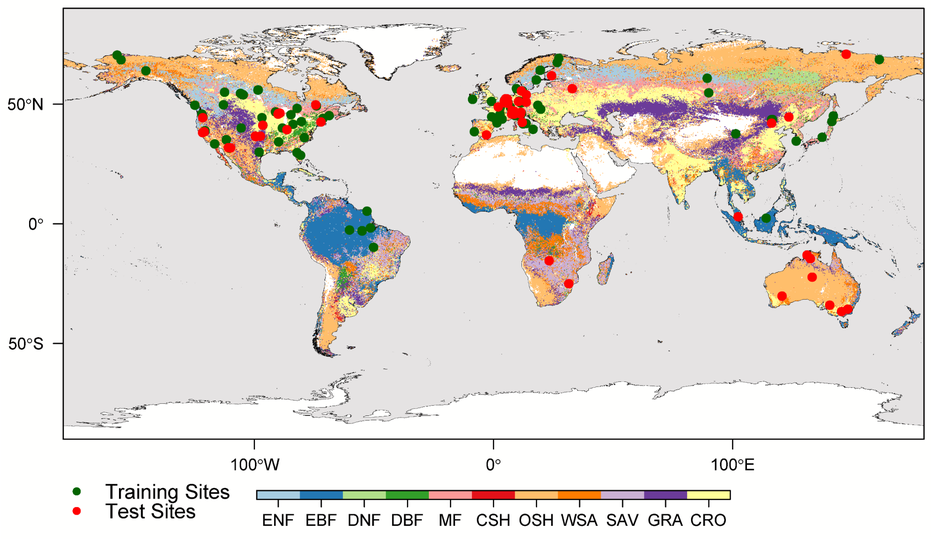
We used GIMMS-3g long term FPAR record along with reanalysis data from MERRA-2, to model GPP from 1982 to 2016 using an improved Light Use Efficiency (LUE) model.

Methodology

- Static LUE_{max} predefined for each biome types in LUE models has been known as the main source of uncertainty in these models.
- Based on these models, plants in a biome background matrix operate at their maximum capacity in up-taking atmospheric CO_2 and converting that into biomass.
- In order to improve the biome homogeneity assumption of ecosystem processes in the LUE models, we used global carbon flux towers from the FLUXNET network to estimate the optimum LUE (LUE_{opt}) at each tower site.
- Using a selection of environmental explanatory variables such as Max and Min FPAR, average annual SIF from GOME-2, and long term average annual temperature, we extrapolated LUE_{opt} observations into global scales using a machine learning method. Max and Min annual FPAR from 1982-2016 was used to create dynamic LUE_{opt} information.



Boxplot showing the variability in flux tower derived LUE_{opt} for different land cover classes. The number above each boxplot shows the total number of tower sites used to represent each land cover class, and the red dots denote the maximum light use efficiency used in the current version of the MODIS MOD17 product.

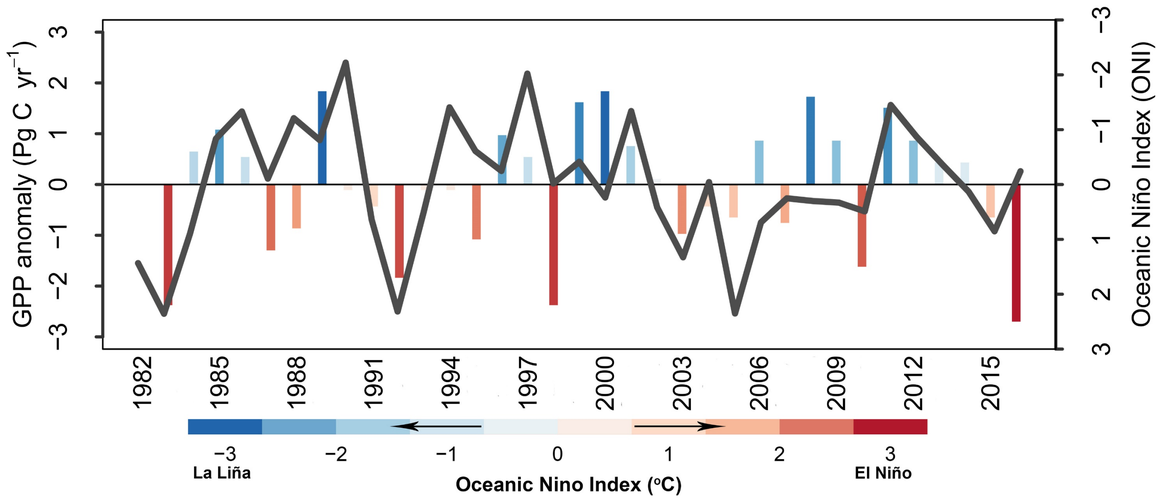


Location of global flux tower sites used for estimation of LUEopt. Tower sites are overlaid on a global land cover map (MODIS MCD12C1-Type2). The FLUXNET tower sites include 95 training sites and 54 validation sites.

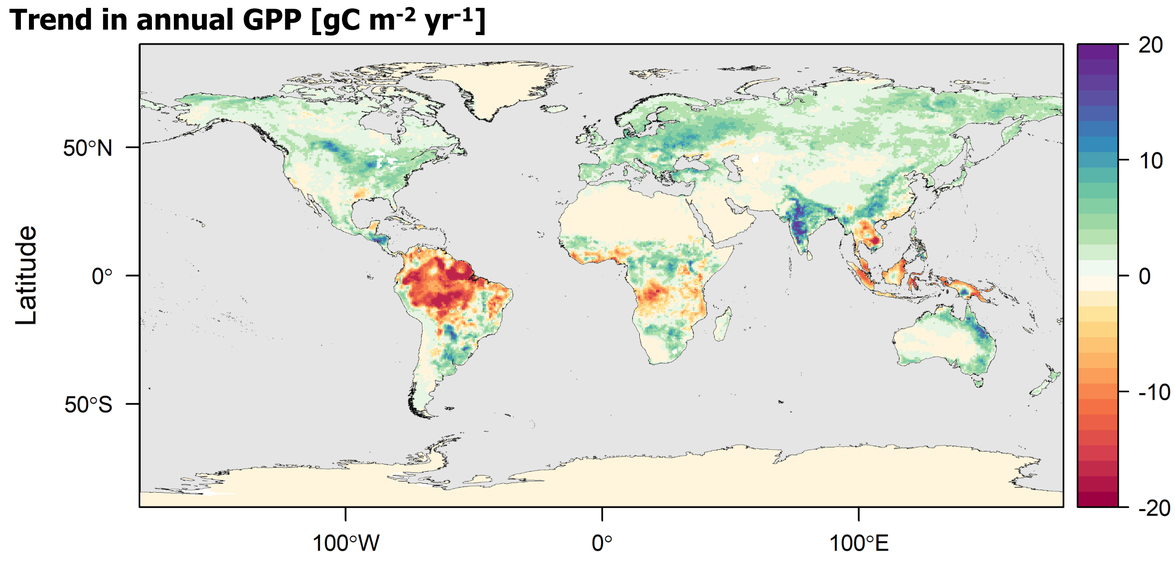
National Aeronautics and Space Administration
Jet Propulsion Laboratory
California Institute of Technology
Pasadena, California

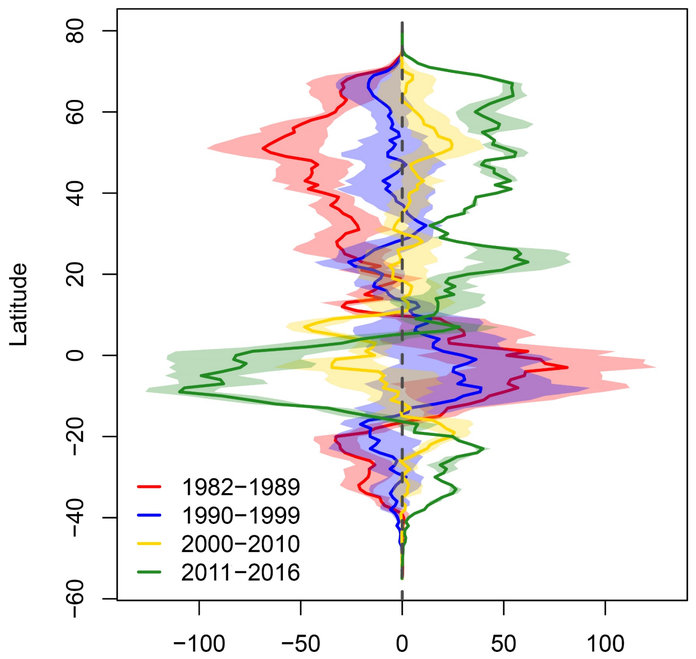
Results

Anomaly in global GPP from 1982-2016.



Trend in annual GPP [gC m^{-2} yr^{-1}]





- Thirty five-year annual linear trend in GPP shows that in 80% of the vegetated land area GPP shows increasing trends up to 20 gC m-2 yr-1 ($P < 0.05$).
- The GPP of northern latitude ecosystems (+45ºN) after the year 2000 on average has increased by 50 gC m-2, which is consistent with observation of increase in shrub dominance in tundra.
- In the northern latitudes after the mid-1990s (+45ºN) GPP started to increase by 0.5-1.5 Pg compared to 35-year average for the region.
- The northern ecosystems GPP increase is highly related to increase in air temperature and changes in FPAR.
- The annual GPP in the Amazon has started to decline after the year 2004.
- The increase in VPD of Amazonian tropical forests corresponds to a decreasing trend in annual GPP.

Summary

- We provided the largest improvements in the LUE model since it development in late 1990s.
- Based on the new GPP model. the increasing trend in GPP has been offset by declining carbon uptake in tropical forests.
- The reduction rate of GPP in tropical forest, that account for about a quarter of global biomass and are responsible for one third of the global carbon flux, is alarming.

www.nasa.gov

Poster No. EA-18

Copyright 2019. All rights reserved.

National Aeronautics and Space Administration

Assimilation of GRACE data into CARDAMOM

Author: Victoria Meyer (329G)
Anthony Bloom (329G), JT Reager (329F), Mingjie Shi (329G), Marcos Longo (329G), John Worden (3290)

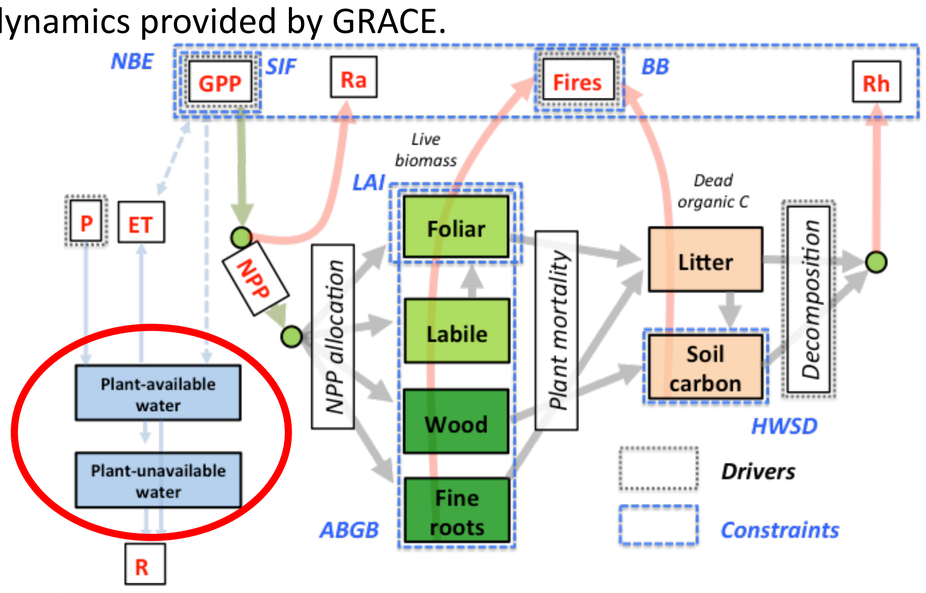
Introduction

A number of land surface models already try to represent the temporal evolution of Carbon (C) and/or water (H_2O) state variables, but none of them explicitly uses observations of **equivalent water thickness (EWT)** to constrain state variables and process controls on **belowground water and its impact on the overlying vegetation**.

- We investigate the added value of temporal constraints on C and H_2O cycles using GRACE (Gravity Recovery And Climate Experiment) water storage data.
- We use the CARbon DAta-MOdel fraMework (CARDAMOM) to represent the evolution of C and H_2O state variables and associated processes (Bloom et al., 2016).
- We test our model in key pixels and in the Amazon basin

Methods: from one to two water buckets

CARDAMOM was modified to account for plant unavailable water (PUW), which, together with plant available water (PAW), can be related to the total water dynamics provided by GRACE.



Carbon (C) Fluxes

H2O Fluxes
P = Precipitation
R = Runoff
ET = Evapotranspiration

Links between GPP, ET and water storage:

1) Calculate GPP: $GPP = GPP_{max} \times H2O_{stress}$

2) Calculate ET, based on: $GPP \times VPD/ET = constant$ (MET driver; Inherent water use efficiency)

3) Update PAW and PUW:

$$PAW_{t+1} = PAW_t + (P_t - R_t - ET_t)\,\Delta t$$
$$PUW_{t+1} = PUW_t + (cR_t - R'_t)\,\Delta t$$

(Runoff coming from PAW bucket)

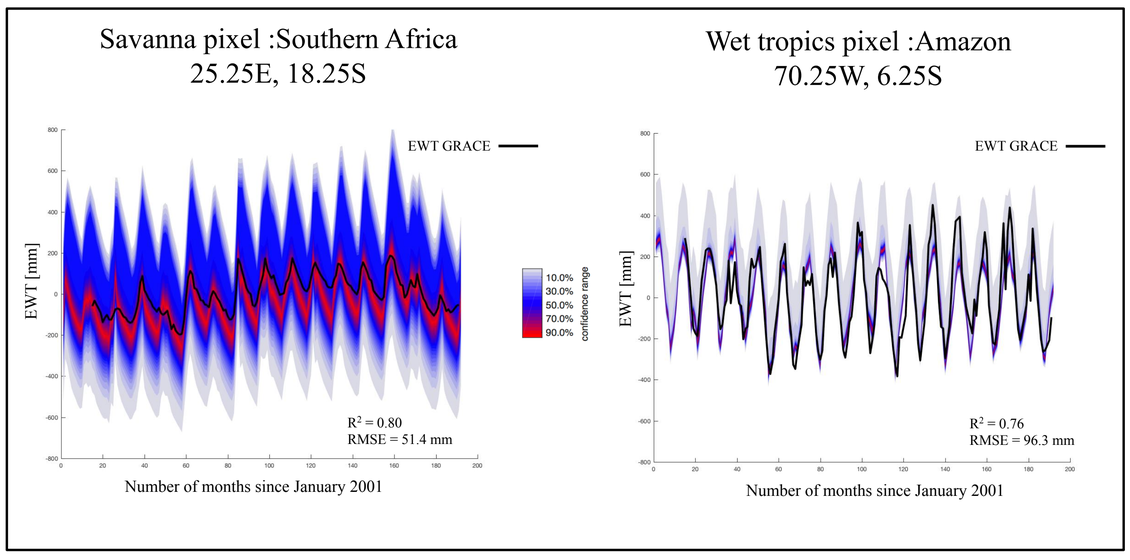
$$with\ R_t = aPAW_t^2 \quad and\ R_t' = bPUW_t^2$$

With 6 parameters being optimized:

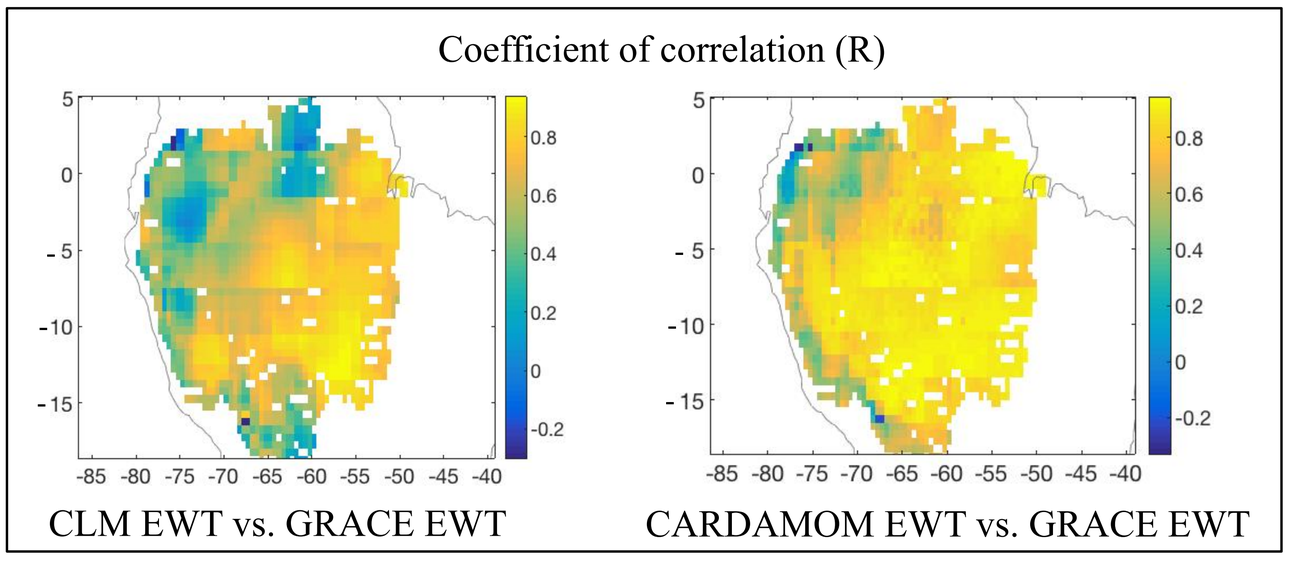
- Initial condition for PAW and PUW
- Runoff coeff for PAW and PUW
- Fraction of runoff that goes to PUW
- Water use efficiency

GPP = Gross Primary Production **Ra** = Autotrophic Respiration **Rh** = Heterotrophic Respiration **NPP** = Net Primary Production (GPP-Ra)

Results: CARDAMOM is able to reproduce GRACE data



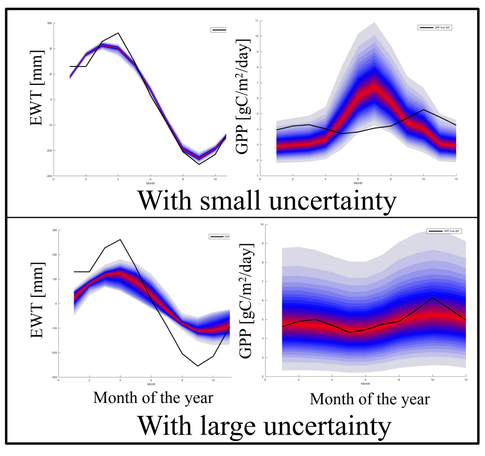
Pixel level examples



Maps of the Amazon basin

Summary and next steps

- CARDAMOM can reproduce seasonal and inter annual variations of GRACE data in amazon river basin
- There is a tradeoff between EWT and GPP, highlighting that some mechanisms are not well represented by the model
- Gridded Runoff will be ingested in a river routing model and compared to river gauges for validation (Yamazaki et al., 2011)



References

Bloom, A. Anthony, et al. "The decadal state of the terrestrial carbon cycle: Global retrievals of terrestrial carbon allocation, pools, and residence times." *Proceedings of the National Academy of Sciences* 113.5 (2016): 1285-1290.
Yamazaki, D., S. Kanae, H. Kim, and T. Oki (2011), A physically based description of floodplain inundation dynamics in a global river routing model, Water Resour. Res., 47, W04501, doi:10.1029/2010WR009726.

National Aeronautics and Space Administration
Jet Propulsion Laboratory
California Institute of Technology
Pasadena, California

www.nasa.gov

Poster No. EA-19

Copyright 2019. All rights reserved.

National Aeronautics and Space Administration

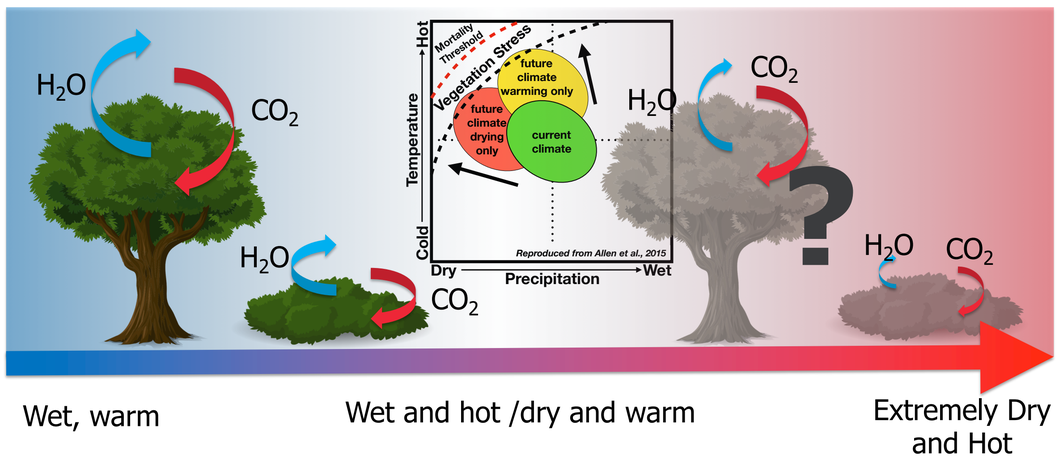
Evaluating the strength of the carbon-water cycle coupling and vegetation functional responses to environmental stress with OCO-2 and SMAP

Author: A.J. Purdy 329-G
Joshua B. Fisher 329-G

We find ecosystem responses to warmer and drier environmental conditions as observed by SIF and transpiration from a MODIS-driven ET algorithm show distinct responses across different eco-climatic regions.

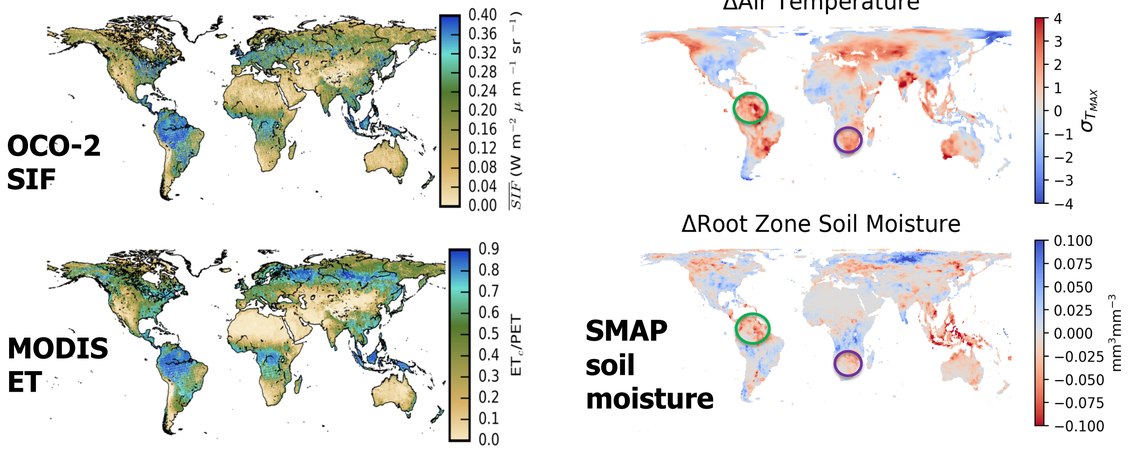
Background

Plants link the carbon and water cycles through their control on photosynthesis and transpiration. Under a changing climate how plants respond to changes in water availability, temperature, and cloud cover remains an open science question. This open question largely impacts the uncertainty of climate projections.



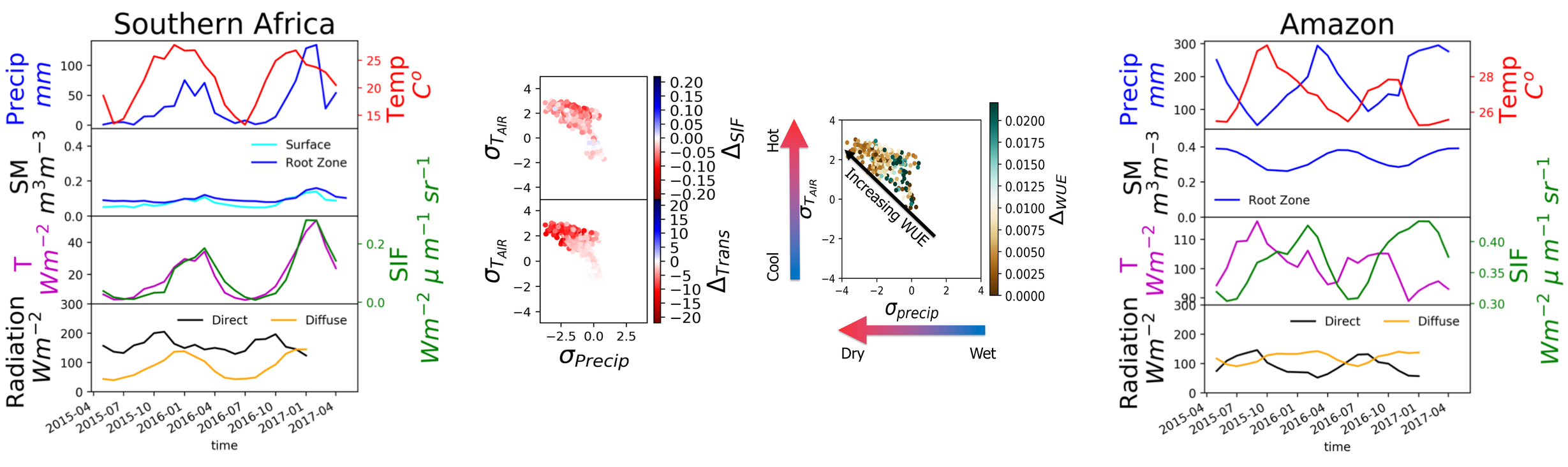
Methods

OCO-2 solar induced fluorescence, SMAP soil moisture, and a MODIS-driven evapotranspiration model provide coincident observations to study changes in carbon and water cycles from space. We diagnose how regions that experienced hotter and drier conditions responded to regulate carbon uptake and water loss.



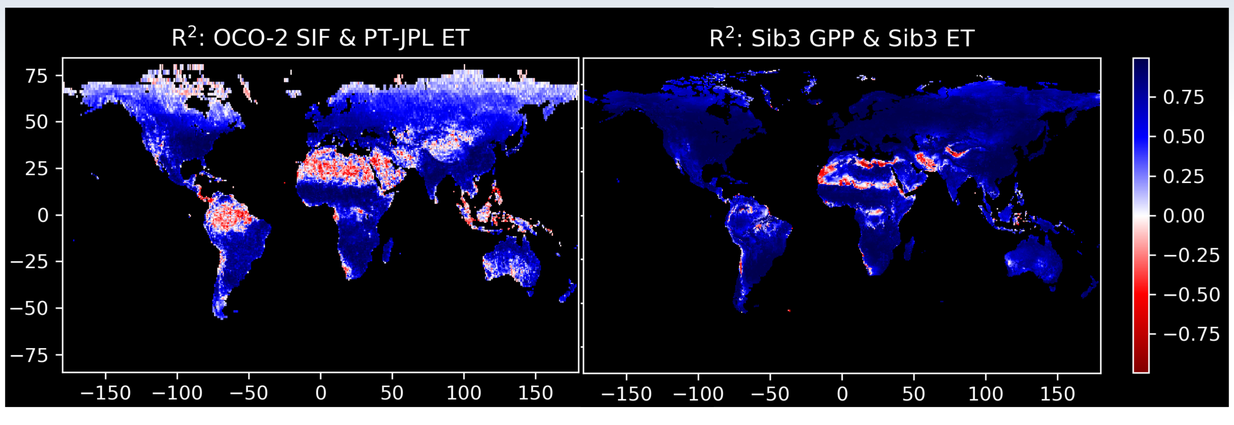
Results

For water and temperature limited regions, the carbon and water ecosystem responses are tightly coupled (Left). Space-for-time analysis reveals ecosystems increase water-use-efficiency under extreme perturbations (Center). In wet tropical regions, we find evidence that the amount of diffuse and direct radiation may help explain divergence in these cycles (Right).



Discussion

This work directly addresses key science goals of SMAP and OCO-2 to understand the processes that link the terrestrial water, energy, and carbon cycles in order to build better models to predict carbon sinks in the future. Here, satellite observations reveal many Earth system models over-estimate strength of the carbon and water cycle linkage in the tropics relative to observations. Further, analyses on the fraction of diffuse radiation and the impact of short-term perturbations in controlling environmental variables offers a path towards refining model structure or parameterizations to address these limitations.



National Aeronautics and Space Administration
Jet Propulsion Laboratory
California Institute of Technology
Pasadena, California

www.nasa.gov

Poster No. EA-20

Copyright 2019. All rights reserved.

Sensitivity of longwave radar backscatter to soil freezing process in Arctic tundra

Author: Yonghong Yi[1] (329G)
Richard Chen[2], Mahta Moghaddam[2], John Kimball[3], Charles Miller[1]

[1]Jet Propulsion Laboratory, California Institute of Technology [2]Dept. Electrical Engineering, University of Southern California [3]NTSG, University of Montana

1. Background

The contribution of cold-season soil respiration to the Arctic-boreal carbon cycle and its potential feedback to global climate remain poorly quantified, partly due to a poor understanding of soil moisture variation and its effects on the seasonal freezing and thawing (F/T) of the active layer in permafrost landscapes.

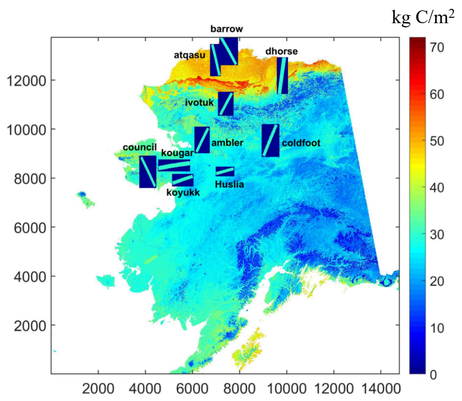


Fig. 1 AirMOSS flight lines from Alaska ABoVE campaign.

- Longwave radar can potentially provide useful information on subsurface soil properties regulating the active layer F/T process.
- We investigate the sensitivity of P-band (430 MHz) radar data to active layer soil freezing using a data-modeling framework.

2. Methods

We simulated P-band radar backscatter using a coupled modelling framework (Fig. 2), which includes a permafrost hydrology process model (Yi et al. 2019) and radar scattering model (Chen et al. 2019).

- A key challenge is to accurately represent thermal, hydraulic and dielectric profiles in highly organic tundra soils.
- A new organic soil parameterization (Fig. 3) was developed (Chen et al. in Prep.) to harmonize key parameters common to both models.

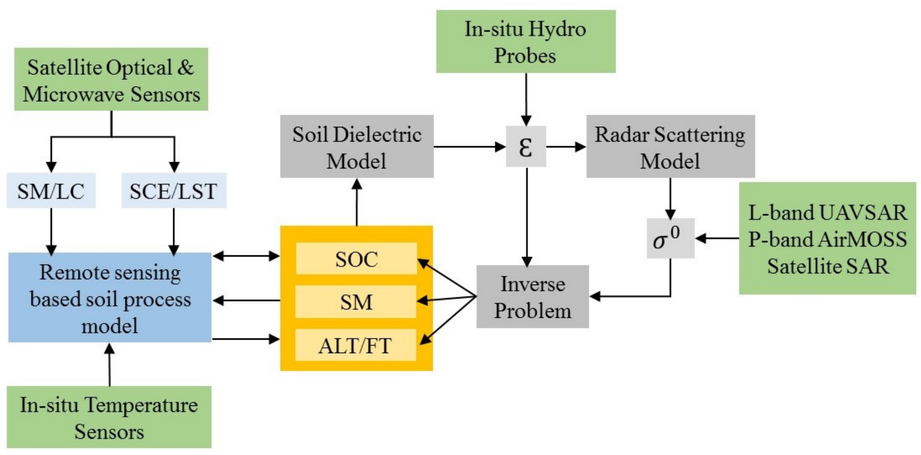


Fig. 2 The coupled soil-radar modeling framework in which the soil process model generates an initial soil F/T and dielectric profile for the radar scattering model; in-situ dielectric or radar backscatter data are used to optimize key common soil parameters.

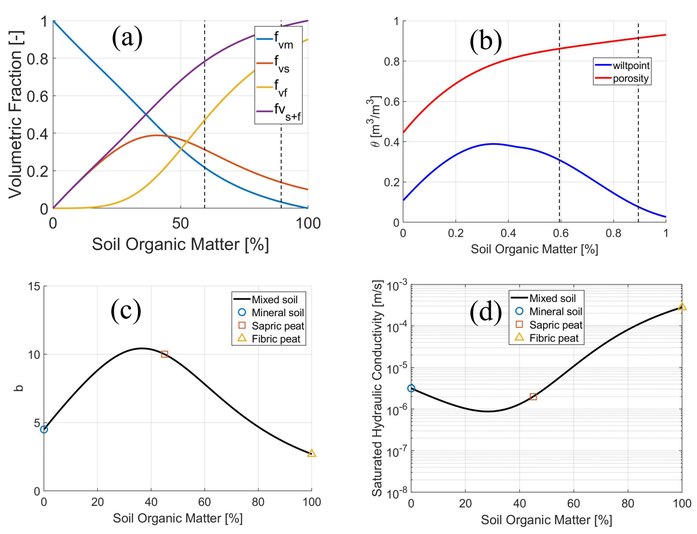


Fig. 3 Simulated change in key tundra soil parameters to varying soil organic matter (SOM) levels (a-d).

3. Sensitivity of soil dielectric constant to soil organic carbon (SOC) profile

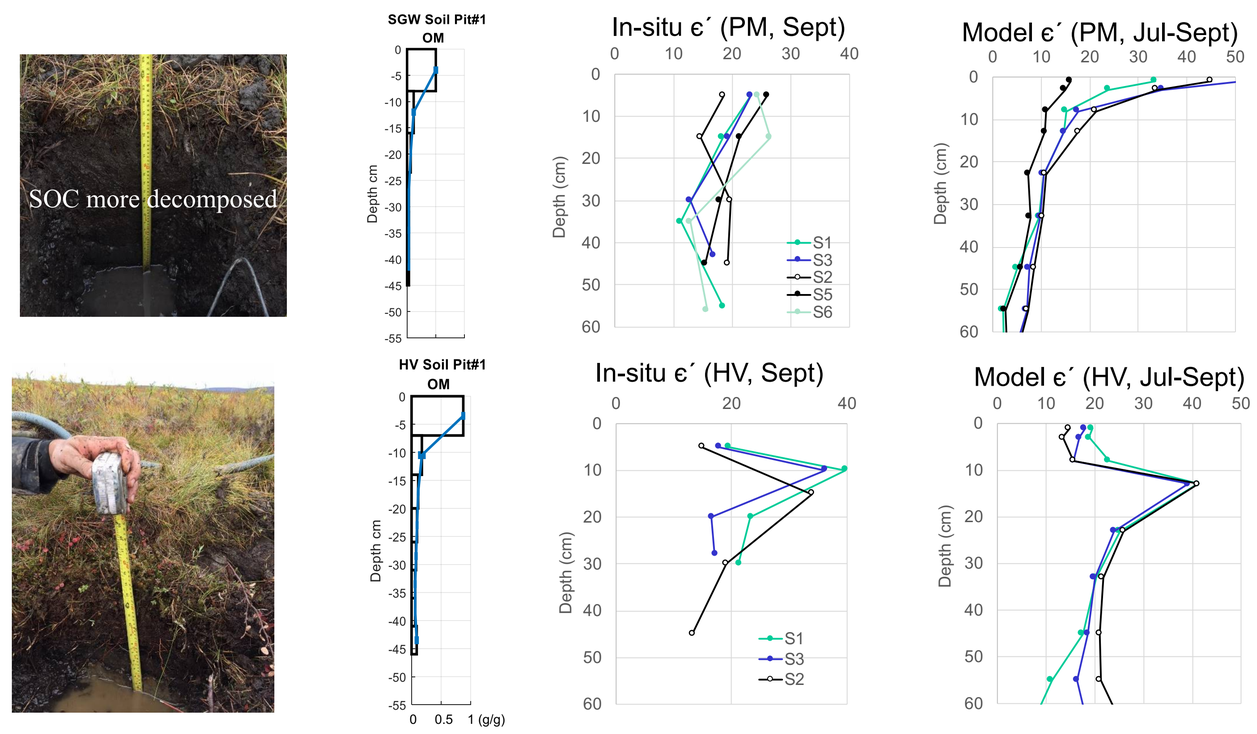


Fig. 4 Model vs in-situ soil dielectric constant profile at Prudhoe Meadow (PM, a-c, more decomposed SOC), and Happy Valley (HV, d-f, less decomposed SOC) sites located in dhorse transect (Fig. 1).

4. P-band radar backscatter sensitivity to active layer freezing

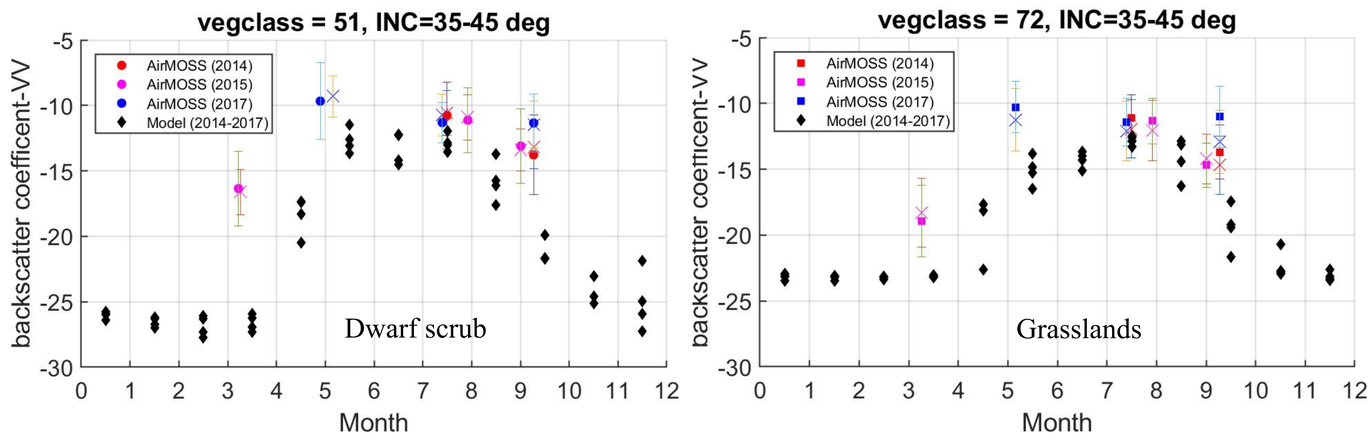


Fig. 5 Seasonality of model simulated radar backscatter vs AirMOSS data for two dominant Alaskan North Slope tundra types (Dwarf scrub vs grassland). Model simulations were conducted at PM (grassland) and HV (Dwarf scrub) sites from 2014 to 2017 (INC = 40º). AirMOSS data were averaged from all pixels with INC ranging from 35º to 45º. Dwarf scrub dominates at Ivotuk and dhorse lines; grassland dominates in atqasuk and dhorse lines.

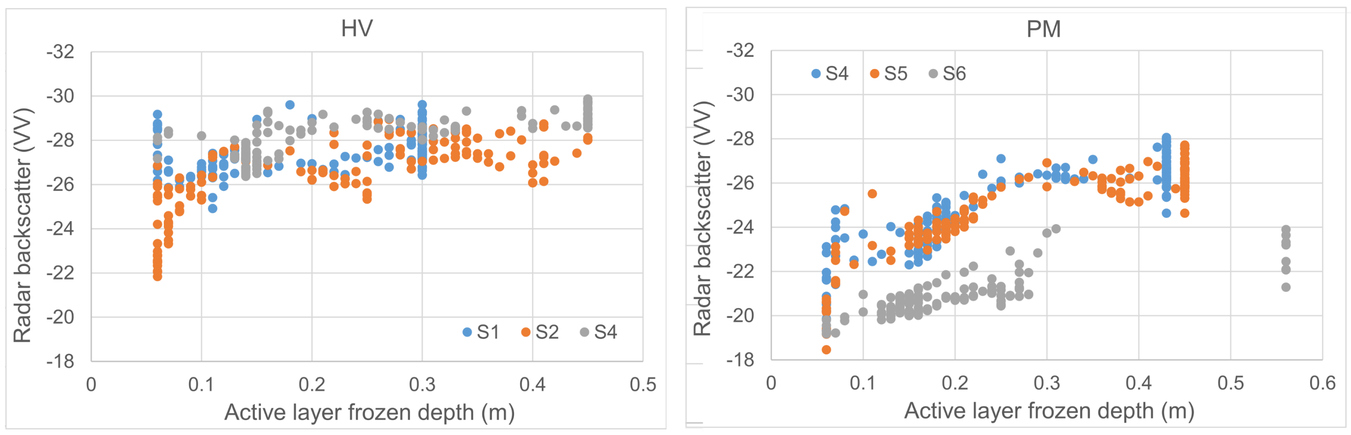


Fig. 6 Model simulated radar backscatter sensitivity to soil frozen depth during early cold season at PM and HV sites. Both the model simulations and detection of soil frozen depth were based on in-situ soil dielectric data.

Conclusions:

- P-band radar is sensitive to changes in soil active layer liquid water content, and can be an effective indicator of active layer frozen depth during early winter.
- Accounting for both total soil carbon content and condition is needed to accurately simulate seasonal wetting and drying of active layer.

National Aeronautics and Space Administration

Jet Propulsion Laboratory
California Institute of Technology
Pasadena, California

www.nasa.gov

Copyright 2019. All rights reserved.

Reference:

1. Yi, Y., Kimball, J.S., Chen, R.H., Moghaddam, M., and Miller, C.E.: Sensitivity of active layer freezing process to snow cover in Arctic Alaska, *The Cryosphere,* 2019.
2. Chen, R.H., A. Tabatabaeenejad, and M. Moghaddam. Retrieval of Permafrost Active Layer Properties Using Time-Series P-Band Radar Observations, *IEEE Trans. Geosci. Remote Sens.,* 2019.

Poster No. EA-21

InSAR and GNSS Time-series for Observing Slow-Slip Events along the Mexican Subduction Zone

Author: Jeremy Maurer (334H)
D. Bekaert (334H), J.A. González-Ortega (CICESE)

Introduction

Slow-slip events (SSEs) release stress build-up just like earthquakes. Unlike earthquakes, SSEs do not cause notable shaking, and last from weeks to months rather than seconds. Although not dangerous themselves, SSEs do change the stress field and can potentially trigger a devastating earthquake. The inter-relation between slow-slip events and earthquakes is not well understood and an active research topic within the solid earth community.

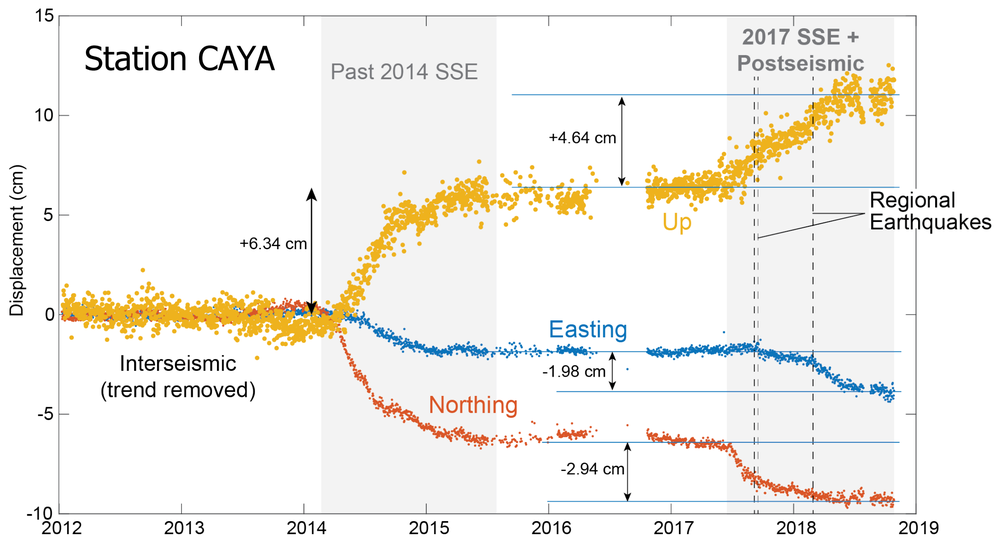
Background: SSEs occur every 3-4 years near Guerrero, Mexico, with the most recent starting in 2017, during which the 2017 Puebla and 2018 Oaxaca earthquakes occurred. Key questions involve: Did the SSE trigger the earthquakes, or vice versa? How will these events impact the next large earthquake on the Mexico subduction zone?

Problem: GNSS data is sparse in the region, and can be complemented with dense InSAR observations. However, InSAR is challenged by atmospheric noise 5x larger than the SSE signal.

Objective: Our objective is to complement available GNSS data with Sentinel-1 InSAR time series with tropospheric noise removed to model slip on the subduction zone during the SSE

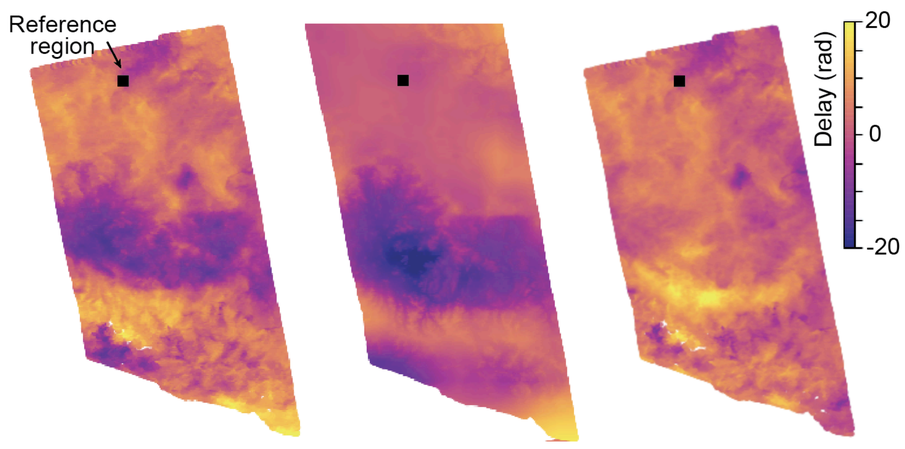
Methods

GNSS: We processed data from 19 stations, estimated and removed the inter-SSE steady velocity, and computed SSE offsets from the residuals.



GNSS time-series from station CAYA, showing offsets from the 2014 and 2017 SSEs, and the time of regional earthquakes (dashed lines).

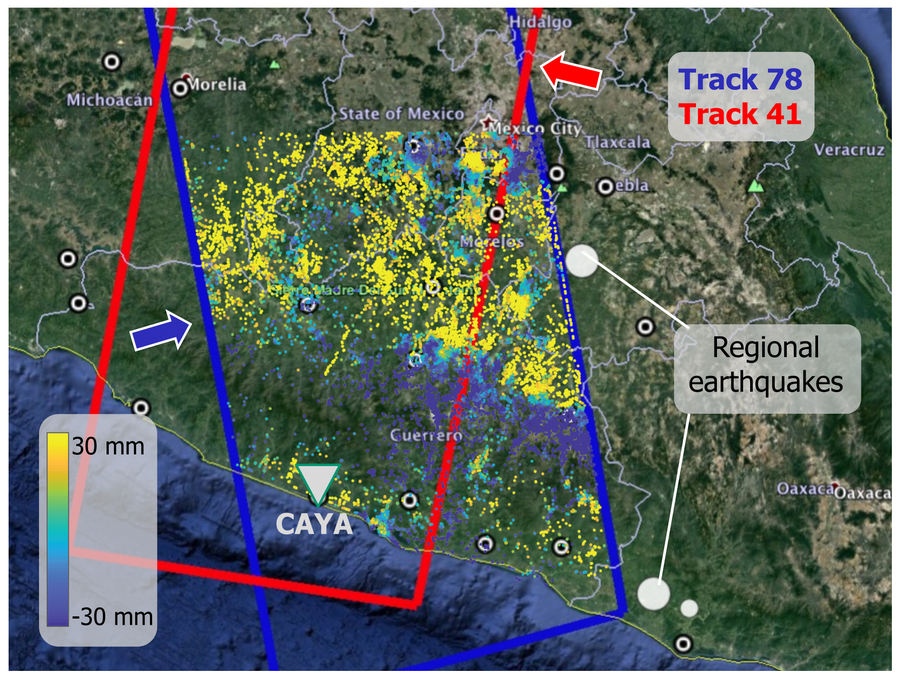
Sentinel-1: We used JPL's ISCE software to process the data up to interferogram level, and reduced tropospheric noise using a newly developed ray-tracing algorithm leveraging data from the European Centre for Medium-Range Weather Forecasts.



Original interferogram: (left), Troposphere estimate (center), Corrected interferogram (right). 6.28 radians = 28 mm in line-of-sight displacement

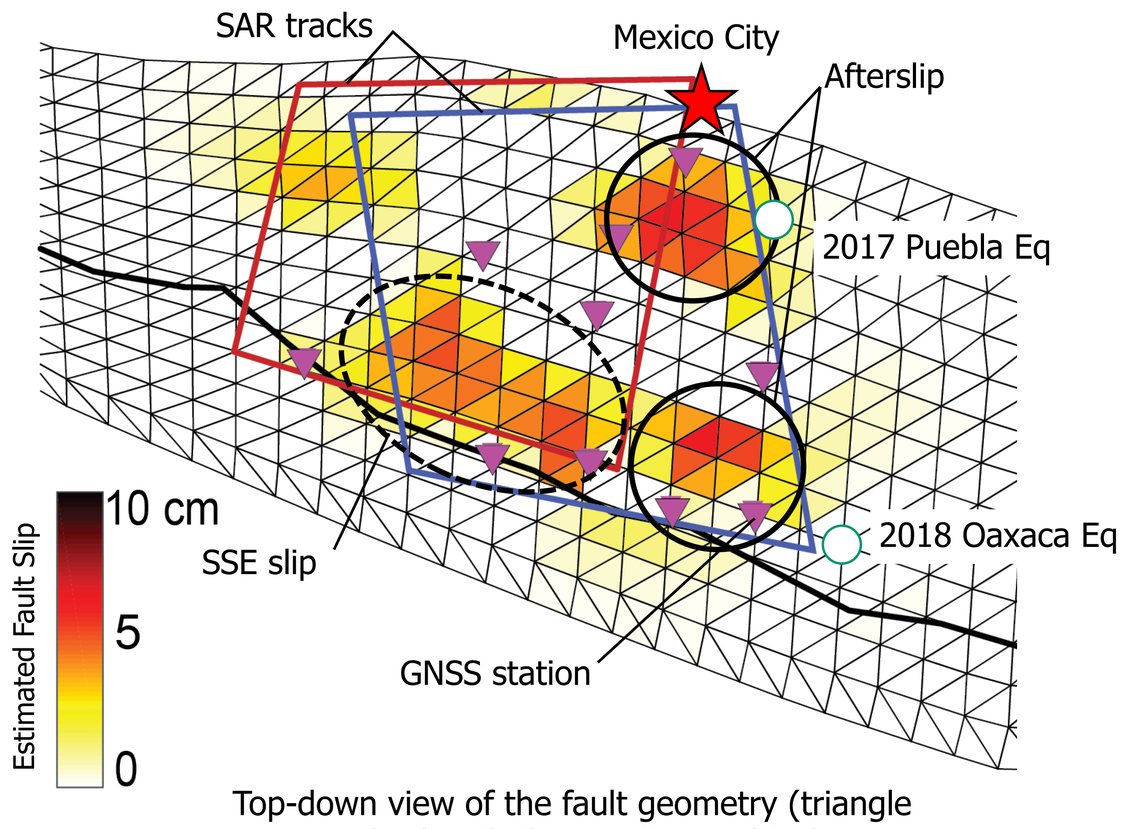
Results

Observed displacements: We used GIAnT to perform a time-series analysis for each track and estimated cumulative offsets for the 2017 SSE, shown below for track 78.



Overview of the Guerrero, Mexico study region, with the Sentinel-1 tracks shown (arrows are look directions) and cumulative SSE offsets from track 78.

Fault slip: We find that the 2017 Puebla and 2018 Oaxaca earthquakes triggered additional aseismic slip (afterslip) on the fault. We estimate total slip from the SSE and afterslip and find a total moment release corresponding to an M_W 7.1-7.2 earthquake. Although GNSS data has lower noise, we find that the additional data density from InSAR greatly improves the model resolution, especially outside the area with GNSS data.



Top-down view of the fault geometry (triangle patches) with the coastline in black.

Conclusions

- The 2017 SSE in Guerrero, Mexico was superimposed by aseismic afterslip from the 2017 Puebla and the 2018 Oaxaca earthquakes
- The combined slip on the fault from the SSE and afterslip was equivalent to a Mw 7.1-7.2 earthquake
- Incorporating tropospheric noise correction methods improves the detection threshold for slow slip events from InSAR, and complements observations from other geodetic datasets.

Poster No. EA-22

National Aeronautics and Space Administration
Jet Propulsion Laboratory
California Institute of Technology
Pasadena, California

www.nasa.gov

Copyright 2019. All rights reserved.

National Aeronautics and Space Administration

A Hybrid Damage Detection Approach based on Multi-temporal Coherence and Amplitude Analysis for Disaster Response

Author: Jungkyo Jung (334K) and Sang-Ho Yun (334K)

Introduction

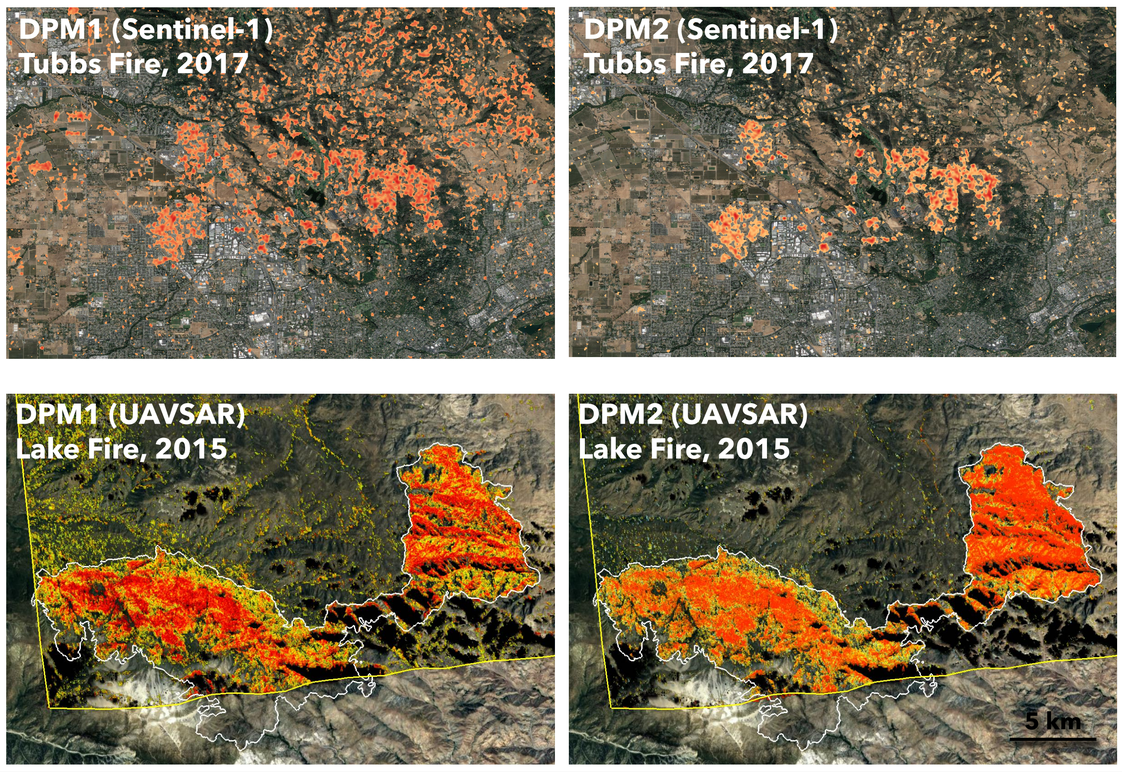
Rapid imaging of damage caused by the natural disasters is becoming an increasingly essential part of disaster management by response efforts. The Advanced Rapid Imaging and Analysis (ARIA), a joint project between JPL and Caltech, has been developing algorithms and a system to rapidly produce Damage Proxy Maps (DPMs) from Synthetic Aperture Radar (SAR) observations. The algorithms and system were successfully tested for a variety of natural disaster events including the Feb 2011 Christchurch Earthquake, 2013 Super typhoon Haiyan, 2015 Gorkha Earthquake[1]., 2017 Hurricane Maria, and 2018 Camp & Woolsey Fires in California.

So far, DPM version 1, which is based on interferometric SAR coherence, has been produced and delivered for response. DPM2, which is based on multi-temporal coherence analysis, was further introduced to enhance the accuracy performance [2) 3)].

Objective

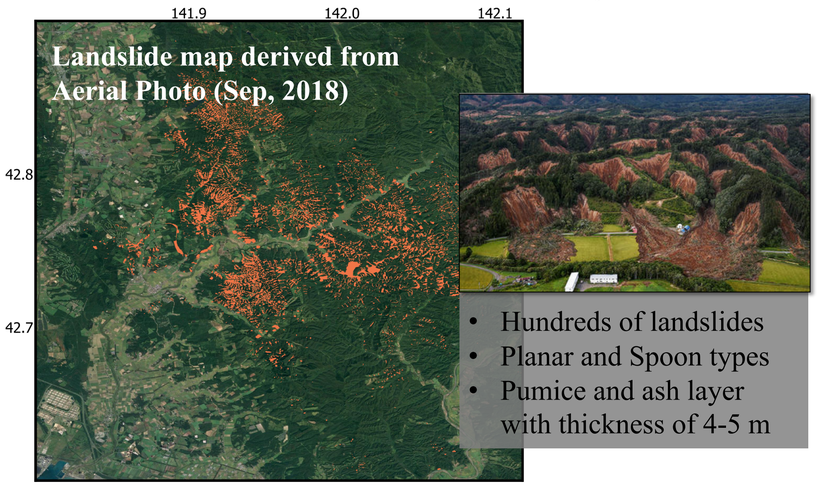
DPM1 and DPM2, coherence-based methods, become less reliable over the pixels with low coherence. This research aims to develop a generalized damage detection algorithm applicable for forest area (low coherence area) using both amplitude and coherence of multi-temporal SAR imagery.

DPM1 vs. DPM2

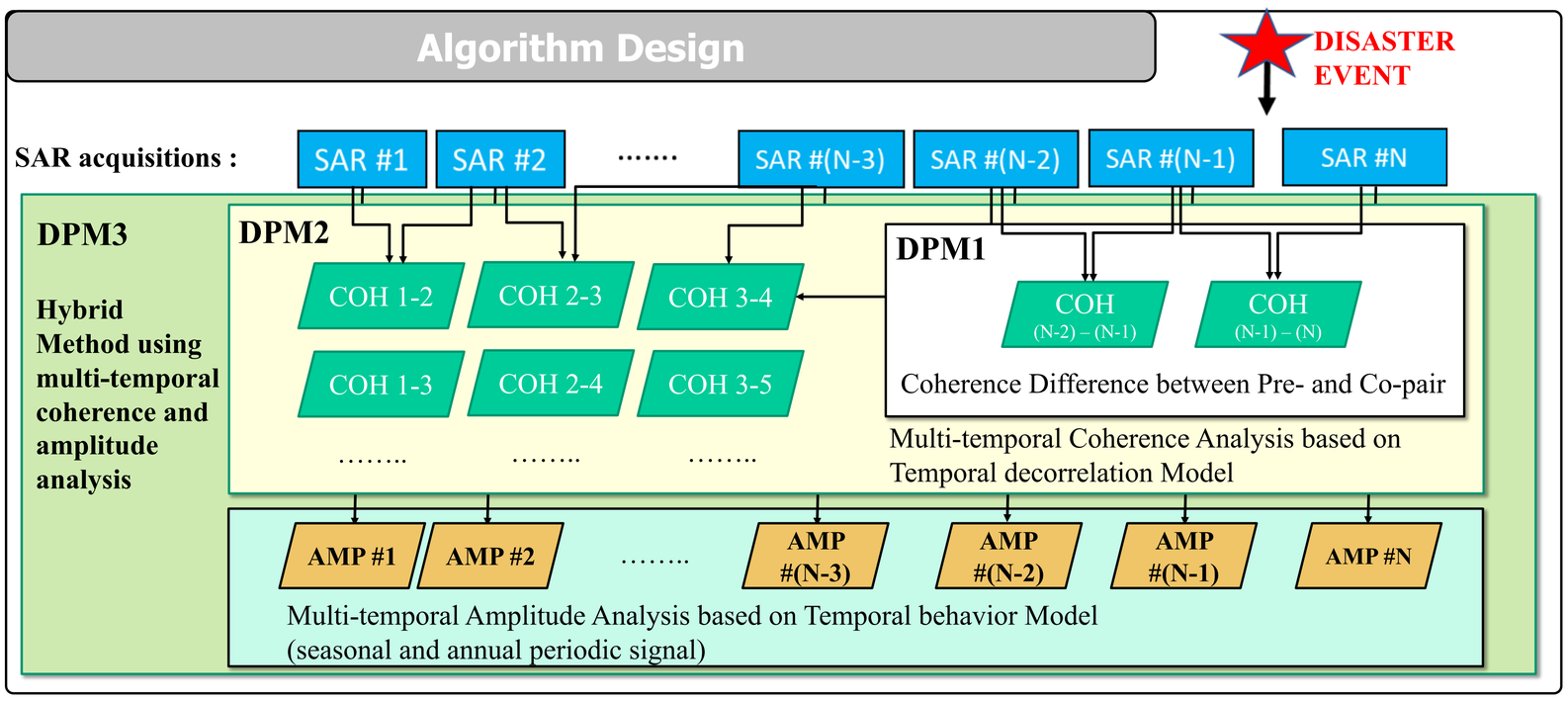


Experimental Study Area

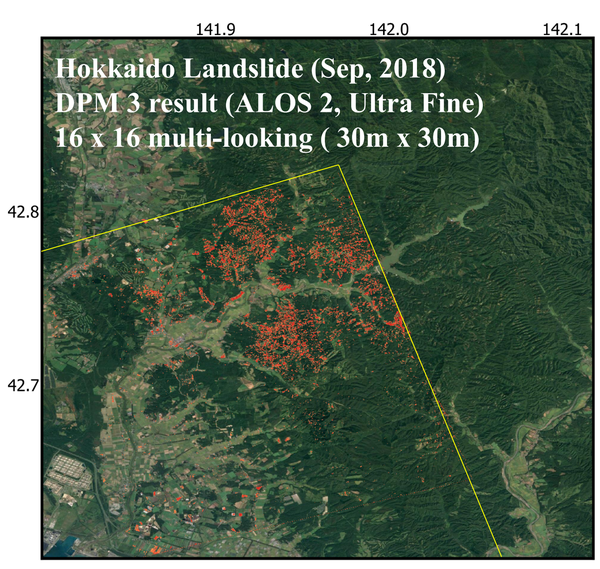
Event Date : September 06, 2018
Landslide trigger : 1) M6.7 Earthquake
2) Heavy precipitation due to Typhoon Jebi



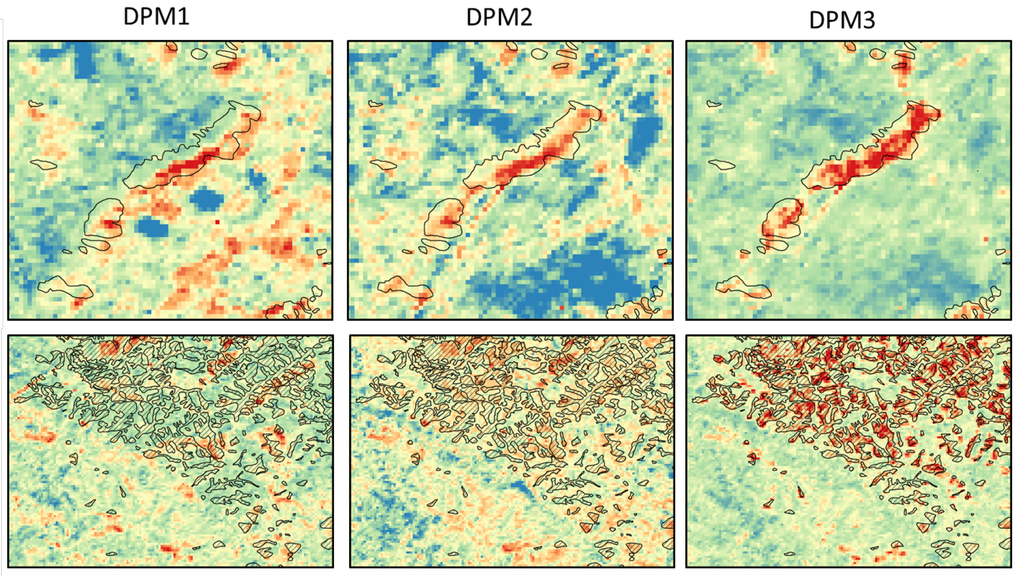
Algorithm Design

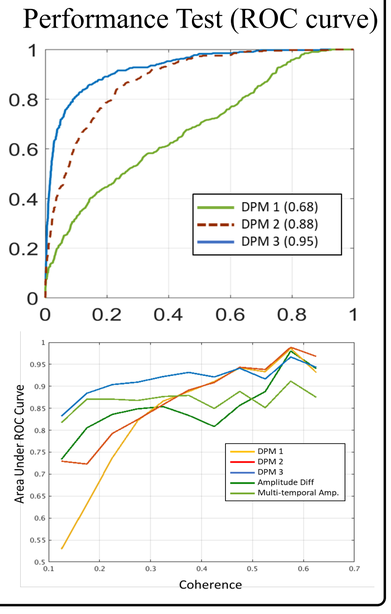


Experimental result for Hokkaido Landslide (2018)









Achievements and Future Study

- DPM3 shows the highest accuracy among the algorithms by detecting the damages even over pixels with low coherence (temporal decorrelation of forest).
- DPM1 is cheap and fast (1-2 days), and DPM2 and 3 are computationally expensive (~2weeks).
- ARIA system's cloud computing can dramatically reduce the computation time.
- Rapid access to historical SAR data is required for timely production of DPM2/3
- Using additional polarizations (i.e. HV/VV) can further improve the performance.

National Aeronautics and Space Administration
Jet Propulsion Laboratory
California Institute of Technology
Pasadena, California

www.nasa.gov

Copyright 2019. All rights reserved.

Reference

1) Yun, S. H., Hudnut, K., Owen, S., Webb, F., Simons, M., Sacco, P., ... & Milillo, P. (2015). Rapid Damage Mapping for the 2015 M w 7.8 Gorkha Earthquake Using Synthetic Aperture Radar Data from COSMO–SkyMed and ALOS-2 Satellites. *Seismological Research Letters*, *86*(6), 1549-1556.
2) Jung, J., Kim, D. J., Lavalle, M., & Yun, S. H. (2016). Coherent change detection using InSAR temporal decorrelation model: A case study for volcanic ash detection. *IEEE Transactions on Geoscience and Remote Sensing*, *54*(10), 5765-5775.
3) Jung, J., Yun, S. H., Kim, D. J., & Lavalle, M. (2017). Damage-Mapping Algorithm Based on Coherence Model Using Multitemporal Polarimetric–Interferometric SAR Data. *IEEE Transactions on Geoscience and Remote Sensing*, *56*(3), 1520-1532.

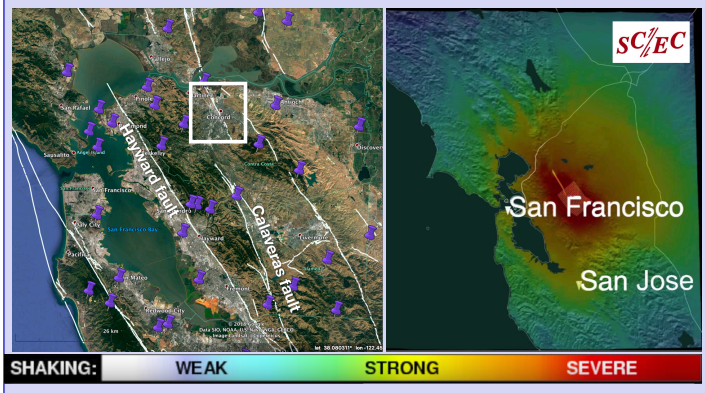
Poster No. EA-23

National Aeronautics and Space Administration

Sentinel-1 time series of transient creep on the Concord Fault, Eastern Bay Area

Ekaterina Tymofyeyeva (334K)
Piyush Agram, Heresh Fattahi (334K)

Motivation:



- Understanding motions on the Concord fault (white square) is important, because an earthquake on this fault would have serious consequences for the Eastern Bay Area (see above).
- The purple "pins" in the map indicate the locations of continuously recording GPS stations. The coverage is reasonably dense, but there aren't enough on the Concord fault to resolve localized fault motions.

Time Series:

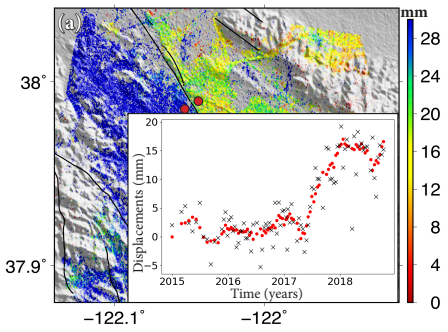


Figure: Time series of displacements on the Concord fault, at two points marked by red and red circles in panel (a). The red points in panel (b) are cumulative displacements in millimeters, corrected for the atmospheric contribution using the CANDIS method (Tymofyeyeva and Fialko, 2015). The black crosses are uncorrected time series, shown for comparison.

Conclusions:

•We apply adaptive multilooking and sequential EVD methods to the study of shallow fault creep on the Concord Fault in the Eastern San Francisco Bay Area, where continuous GPS stations and other geodetic instruments are not available close to the fault.

•We use data from the European Sentinel-1 mission to observe a transient shallow creep event on the Concord fault.

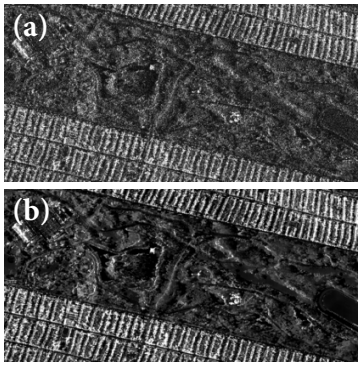
•We are able to determine that the event began in the summer months of 2017, with variable slip along the fault, and a peak cumulative slip amplitude of approximately 15 mm in the direction parallel to the fault trace.

National Aeronautics and Space Administration
Jet Propulsion Laboratory
California Institute of Technology
Pasadena, California

www.nasa.gov

Copyright 2019. All rights reserved.

Methods:



- Created coregistered SLCs with **ISCE processing software.**
- Used **adaptive multi-looking** for noise reduction and coherence estimation (similar to Ferretti et al., 2011).
- Processed data in batches using the **Sequential EVD** (inspired by Ansari et al., 2017)
- Applied **CANDIS atmospheric correction** (Tymofyeyeva and Fialko, 2015)
- Decomposed data from two lines of sight into **vertical and fault-parallel components** (e.g., Tymofyeyeva and Fialko 2018)

Figure: Example of an amplitude image over San Francisco, filtered using adaptive multilooking. Panel (a) shows the original image, and panel (b) shows the filtered image. Sharp features and structures are preserved, while speckle noise in smoother areas is reduced.

Our approach: Sequential time series:

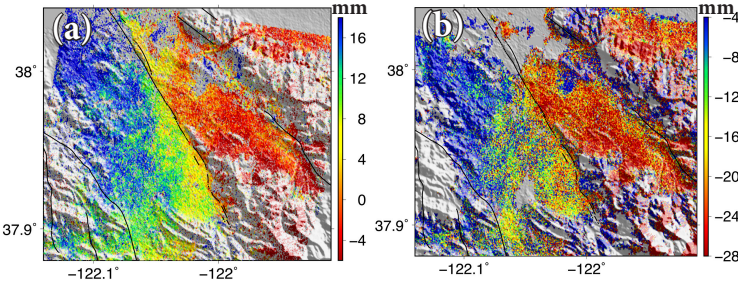
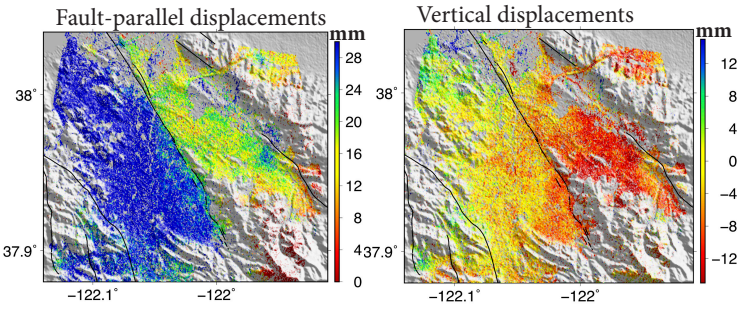


Figure: Cumulative time series from 2014-2019 for descending track 42 over the Concord fault, Eastern Bay Area. Comparison between our time series processing approach (a) and cumulative time series computed by adding up displacements from sequential interferograms (b). All displacements are in millimeters.

Displacements:

Fault-parallel displacements Vertical displacements



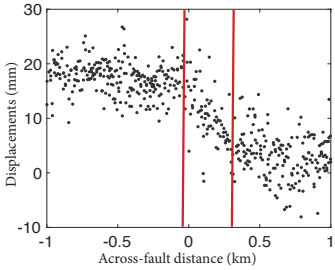


Figure (above): Fault-parallel and vertical displacements derived using Sentinel-1 Tracks 42 and 35 during the time period between 2014-2019, on the Concord fault.

Figure (left): Displacements inside a 800m-wide, 2km-long profile across the Concord fault. The deformation across the fault is not a sharp "step", but rather a gradient across a distance of about 400m, suggesting either that the fault is locked from the surface to a depth approximately equal to the width of the distributed zone (which is likely unphysical), or that the distributed shear zone is a consequence of multiple dislocations, a change in material properties, or a bend in the fault relative to the overall strike, as discussed earlier in this section.

Poster No. EA-24

National Aeronautics and Space Administration

Considerations for the Design of Statistical Analyses of Dependent Data in Distributed Data Systems

Author: Maggie Johnson (398L)
Amy Braverman (398L)

Introduction

Large scale data analyses for Earth science typically involve the use of massive data stored on different servers that do not necessarily share the same file system. This motivates moving towards distributed data and compute systems where the majority of computation is performed at the data site. In this setting, analysts may be faced with a-priori decisions in designing a distributed analysis that could result in a trade-off between various costs (computation/transmission time and even of constructing the system, e.g. cloud computing) and inferential uncertainties (bias, variance, etc.) in the estimates produced by the analysis.

Proposed Design Framework

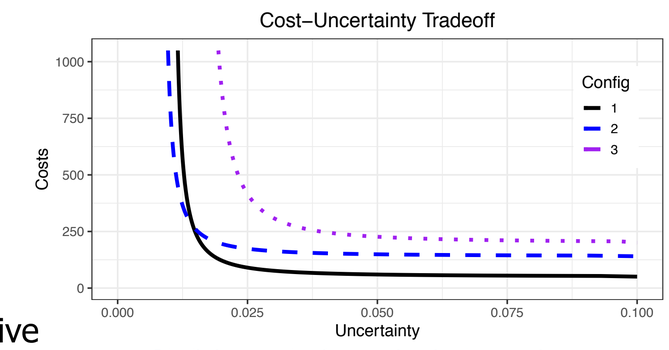
For a given analysis objective, minimize

Total Cost = implementation (time) + λ_1 uncertainty + λ_2 system design (money) + …

over a set of possible designs (statistical, system) subject to budget and uncertainty constraints.

To do this we need:

1. A computationally feasible methodology implementable in a distributed framework.
2. To quantify ALL relevant costs of performing the analysis.
3. Solve a highly constrained, typically nonlinear, multi-objective optimization problem.

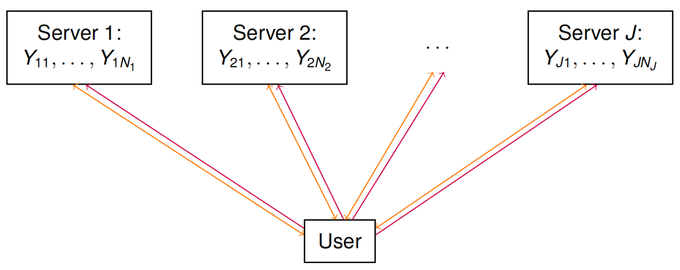


Idealistic example of uncertainty-implementation cost pareto fronts under three system "configurations."

Illustrative Problem: Spatial Covariance Parameter Estimation

Assume we have spatial data $Y_{1,1}, \dots, Y_{J,N_J}$ stored separately on $j = 1, \dots, J$ servers.

- $N = N_1 + \cdots + N_J$ where N_j is large.
- Model spatial dependence through a Gaussian process with p unknown parameters $\boldsymbol{\theta}$, such that $\boldsymbol{Y} \sim MVN(\boldsymbol{X\beta}, \boldsymbol{\Sigma}(\boldsymbol{\theta}))$ where $\boldsymbol{\Sigma}(\boldsymbol{\theta})$ is a $N\ x\ N$ matrix.
- Objective is ML estimation of $\boldsymbol{\theta}$, BUT evaluating the log-likelihood/gradient exactly requires bringing all data together and performing $O(N^3)$ operations at every iteration of a numerical optimization algorithm.

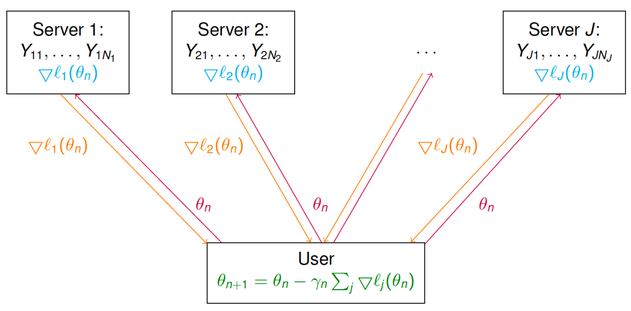


A simplified data system structure.

Step 1: A Distributed Methodology

Approximate the likelihood by assuming data in different servers are **independent.**

- Log-likelihood is a sum of log-likelihoods computed at each server, given a value of $\boldsymbol{\theta}$.
- Numerical optimization can be achieved using distributed gradient descent without moving data.
- $O(N_j^3)$ operations at each server and $O(p)$ at user.



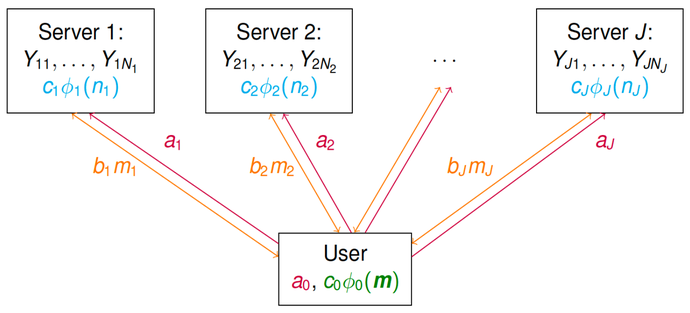
n^{th} iteration of distributed gradient descent.

Step 2: Defining and Quantifying the Cost Tradeoff

Design Questions

Distributed algorithm may still be outside a computational budget if N_j are large.

- How much data, $n_j < N_j$, should be used from each server?
- What is the tradeoff between implementation cost and uncertainty in estimates of $\boldsymbol{\theta}$, depending on system design?



Illustrative system-cost components for the simple data system.

$\boldsymbol{\mathcal{A}} = \{J, N_1, \dots, a_0, \dots, b_1, \dots, c_0, \dots\}$

- define the system
- latency, bandwidth, etc.

$\boldsymbol{\mathcal{B}} = \{n_1, \dots, n_J, m_1, \dots, m_J, \dots\}$

- determined by design of methodology

$\boldsymbol{\mathcal{C}} = \{\varphi_0(\boldsymbol{m}) \propto p,\ \varphi_j(n_j) \propto n_j^3, \dots\}$

- computational complexity

Statistical Costs (Uncertainty)

Define an "anticipated" variance as a function of $\boldsymbol{n} = \{n_1, \dots, n_J\}$.

- Estimate $Var(\boldsymbol{\theta})$ using the information sandwich estimator, $IS(\boldsymbol{\theta})$.
- Integrate out dependence on individual spatial locations, S_n, and unknown $\boldsymbol{\theta}$ using Monte Carlo integration.

$$C_{stat}(\boldsymbol{\mathcal{B}}) = \iint IS(\boldsymbol{\theta}|Sn)\ p(Sn)\ p(\boldsymbol{\theta}) dS_n d\boldsymbol{\theta}$$

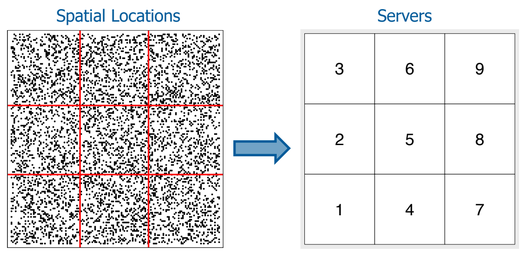
Implementation Costs (Time)

Define $C_{impl}(\boldsymbol{\mathcal{A}}, \boldsymbol{\mathcal{B}}, \boldsymbol{\mathcal{C}}) = g(C_{comm}(\boldsymbol{\mathcal{A}}, \boldsymbol{\mathcal{B}}, \boldsymbol{\mathcal{C}}),\ C_{comp}(\boldsymbol{\mathcal{A}}, \boldsymbol{\mathcal{B}}, \boldsymbol{\mathcal{C}}))$, where

- At each server
  $C_{comm}(\boldsymbol{\mathcal{A}}, \boldsymbol{\mathcal{B}}, \boldsymbol{\mathcal{C}}) = a_j I(n_j > 0) + b\ m_j$ and $C_{comp}(\boldsymbol{\mathcal{A}}, \boldsymbol{\mathcal{B}}, \boldsymbol{\mathcal{C}}) = c_j \varphi_j(n_j) \propto c_j n_j^3$
- At the user

$$C_{comp}(\boldsymbol{\mathcal{A}}, \boldsymbol{\mathcal{B}}, \boldsymbol{\mathcal{C}}) = c_0 \varphi_0(\boldsymbol{m}) \propto c_0 Jp$$

Step 3: Obtain Pareto-Optimal Set of Design Solutions

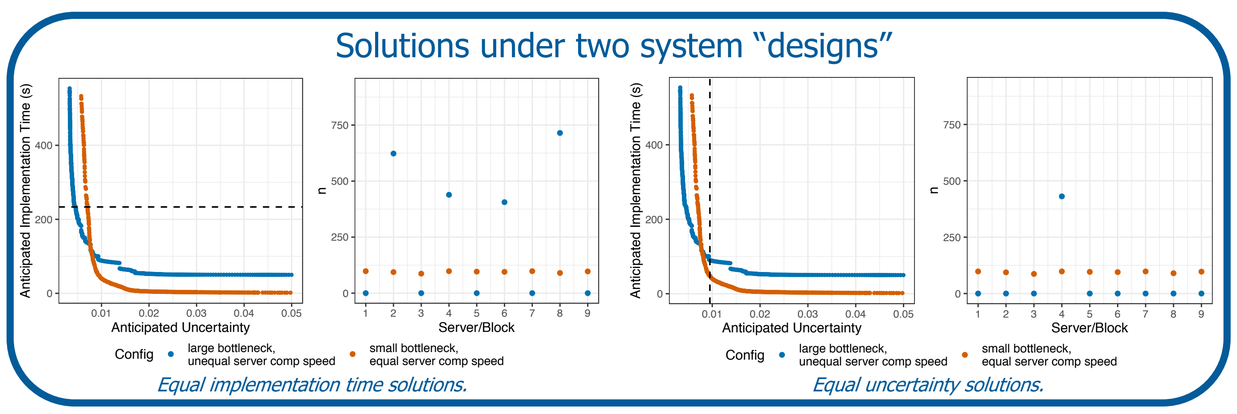


Simulated spatial locations distributed to 9 "servers".

Approximate pareto set of solutions of

$$\min_{n_1,\dots,n_J} C_{stat}(\boldsymbol{\mathcal{B}}) + \lambda C_{impl}(\boldsymbol{\mathcal{A}}, \boldsymbol{\mathcal{B}}, \boldsymbol{\mathcal{C}})$$

using the NSGA-II algorithm implemented in the R package mco.



Discussion

Determining an appropriate function for quantifying statistical cost (e.g. uncertainty) is dependent on the analysis objective and is not straightforward.

- Statistics like variance are typically not easily optimizable functions in small number of parameters.

Realistic values of system parameters (e.g. $\boldsymbol{a}$, $\boldsymbol{b}$, $\boldsymbol{c}$, etc.) are not easily obtained and are most likely dynamic.

- Moving towards quantifying these cost parameters in cloud systems.

Current work is focused on extending this framework for the problem of spatial data fusion of multiple remote sensing data products.

National Aeronautics and Space Administration
Jet Propulsion Laboratory
California Institute of Technology
Pasadena, California

www.nasa.gov

Copyright 2019. All rights reserved.